Statistical Analysis of Travelling Ionospheric Disturbances During Geomagnetic Storms

A Thesis Submitted in Fulfilment
of the Requirements for the Degree of
Master of Science in Physics

RHODES UNIVERSITY
Where leaders learn

Author: Mr. Matsobane Alex Mothibi
Institution: Rhodes University
Department: Physics & Electronics
Date: February, 2025

Abstract

This thesis presents observations of medium to large-scale traveling ionospheric disturbances (TIDs) originating from high latitudes, and propagating towards the equator and TIDs originating from the equator with a poleward propagation in the African-European sector during geomagnetically disturbed conditions between 2006 and 2022. 196 TID activities propagating over the African-European sector were observed, of these TID activities, 161 and 33 were observed during geomagnetic storms, and simultaneous occurrence of geomagnetic storms and solar flares, respectively. Total electron content perturbations derived from Global Navigation Satellite Systems (GNSS) observations within a latitude range of 40°S–60°N and longitude ranges of 20°-40°E representing the African-European sector were analysed based on the storm criteria of Dst $\leq$ -30 nT. The GNSS total electron content (TEC) data were used to obtain the two dimensional (2d) TEC perturbations. The northern hemispheric part of the African sector has limited data coverage which is visualized by a gap around 20°, where there were no data coverage can be observed in the 2d TEC maps. An important result is that large-scale TIDs (LSTIDs) and medium-scale TIDs (MSTIDs) were found to occur predominantly during the main and recovery phases of geomagnetic storms respectively, at least over the African-European sector. During the main phase of storms equatorward LSTID activity was relatively consistent across both hemispheres, with years of solar maximum, between 2013 and 2015, showing higher frequencies of events. Equatorward MSTID activity appeared less frequent overall, particularly in the southern hemisphere (SH), suggesting that equatorward LSTID activity are more prominent during the main phase of geomagnetic storms. Poleward TID activity were more predominant in the recovery phase than the main phase of geomagnetic storms.

Acknowledgement

Much appreciation and thanks to my supervisor, Prof. John Bosco Habarulema, for support during my study and for his motivation. His insights, comments and knowledge helped me in my research and the writing of this thesis. That being said I want to expand my thanks and gratitude towards the South African National Space Agency (SANSA) for awarding me a bursary to obtain my MSc degree. Many thanks to God, my friends and family who gave me their support, encouragement and love which kept me motivated during my studies.

Dedications

This thesis is dedicated to my niece and younger sister, Mrs Tshepiso Korong Mothibi and Mrs Tshegofatsho Kgabo Mothibi.

Contents

Chapter 1: Background

1.1 General Background

The atmosphere of the Earth acts as an electrical system, primarily due to solar radiation, and as a result, the ionosphere is formed. The ionosphere is a region of the Earth's upper atmosphere, predominantly maintained by solar radiation, where there is a high concentration of ions and free electrons. It is located at altitudes ranging from 50 to 1000 km (Dieminger et al., 1996; Goodman, 2005). It serves as a propagation medium for high frequency (HF) radio waves in communication. HF waves are transmitted from the ground to the ionosphere, where electrons refract and reflect them to ground-based receiver. HF waves' refractive and reflective properties enable long-distance communication. Ionospheric refraction causes delays in trans-ionospheric radio transmissions, including those transmitted by GPS satellites and celestial bodies. If the ionospheric electron density remains constant throughout time, refraction corrections can be easily applied to these signals and GPS positioning and timing can be achieved (Rawer, 1993). However, electron density is not uniform throughout space and time, with horizontal gradients and temporal variations (Rawer, 1993).

These unanticipated disturbances can manifest as stationary or moving structures (Rawer, 1993). The latter are known as traveling ionospheric disturbances (TIDs) (Hargreaves, 1979; Rawer, 1993). TIDs are considered ionospheric manifestations of atmospheric gravity waves (AGWs) (Hines, 1974). AGWs are the upward and downward movement of displaced air parcels in the atmosphere as it responds to buoyancy force (Nappo, 2002). A thorough examination of TID incidence in a specific region is crucial for understanding their behavior. Ionospheric probing instruments include Earth-orbiting satellites (Bhonsle et al., 1965; Bhonsle, 1966; Habarulema et al., 2015), ionosondes (Heisler and Whitehead, 1960; Afraimovich et al., 2008), incoherent scatter radar, SuperDARN (Thome, 1964; Karpachev et al., 2010), etc.

In this project, radio signals from Earth orbiting satellites were used to create maps of total electron content (TEC) over African-European sector during the period from 2006 to 2022 for geomagnetically disturbed conditions. TEC is defined as the integral of total electron density from a GPS receiver to an Earth-orbiting transmitting satellite along an imaginary cylinder with a cross-sectional area of 1 m^2 (Hofmann-Wellenhof et al., 2001). Dst $\leq$ -30 nT was used as criteria for geomagnetic disturbance conditions. The observations of TIDs are based on Global Navigation Satellite Systems (GNSS) data for the African-European sector.

1.2 Aims and Objectives

The aim of the study was to perform a statistical analysis of observations of TIDs during geomagnetic storms from 2006-2022. The aim and objectives were driven by the following:

- Do TIDs show Diurnal variation during geomagnetic storms?
- Is there seasonal dependency of TIDs during geomagnetic storms?
- Annual variation of TIDs was investigated.

1.3 Structure of the Thesis

The structure of this thesis is as follows:

- Chapter 1 provides a brief introduction to the research and explains the objectives of the research.
- Chapter 2 discusses a background theory of the ionosphere, that is its creation, morphology, and its behavior.
- In Chapter 3, the background theory on AGWs and TIDs are discussed.
- Chapter 4 provides an introduction to GPS, and illustration and formulation on how TEC data were obtained from GPS. The techniques used to determine the characteristics of TIDs from TEC maps are discussed.
- In Chapter 5, statistical results obtained by applying methods described in Chapter 4 are presented and discussed.
- Chapter 6 gives the conclusion and future work of the thesis.

Chapter 2: The Ionosphere

This chapter provides an introduction to Earth's atmosphere and geomagnetic storms, as well as theoretical background of the ionosphere.

2.1 Earth's Atmosphere

The Mixture of ideal gases that make up the Earth's atmosphere include molecular nitrogen (N_2, 78.11%), oxygen (O_2, 20.95%), argon (Ar, 0.93%), neon (Ne, 18.18 x 10^{-4}%), and helium (He, 5.24 x 10^{-4}%). Zolesi et al. (2014) list water (H_2O, 0-7%), carbon dioxide (CO_2, 0.01-0.1%), and ozone (0_3, 0-00001%) as other minor ingredients. Temperature, density, and pressure all play a role in dividing the Earth's atmosphere into distinct layers (Rishbeth, 1969; Davies and Harré, 1990; Moldwin, 2008; Zolesi et al., 2014). The thermosphere, exosphere, mesosphere, troposphere, and stratosphere are these layers. By taking up the Sun's dangerous radiation, these layers shield our world. According to temperature, Figure 2.1 depicts the layers of the Earth's atmosphere.

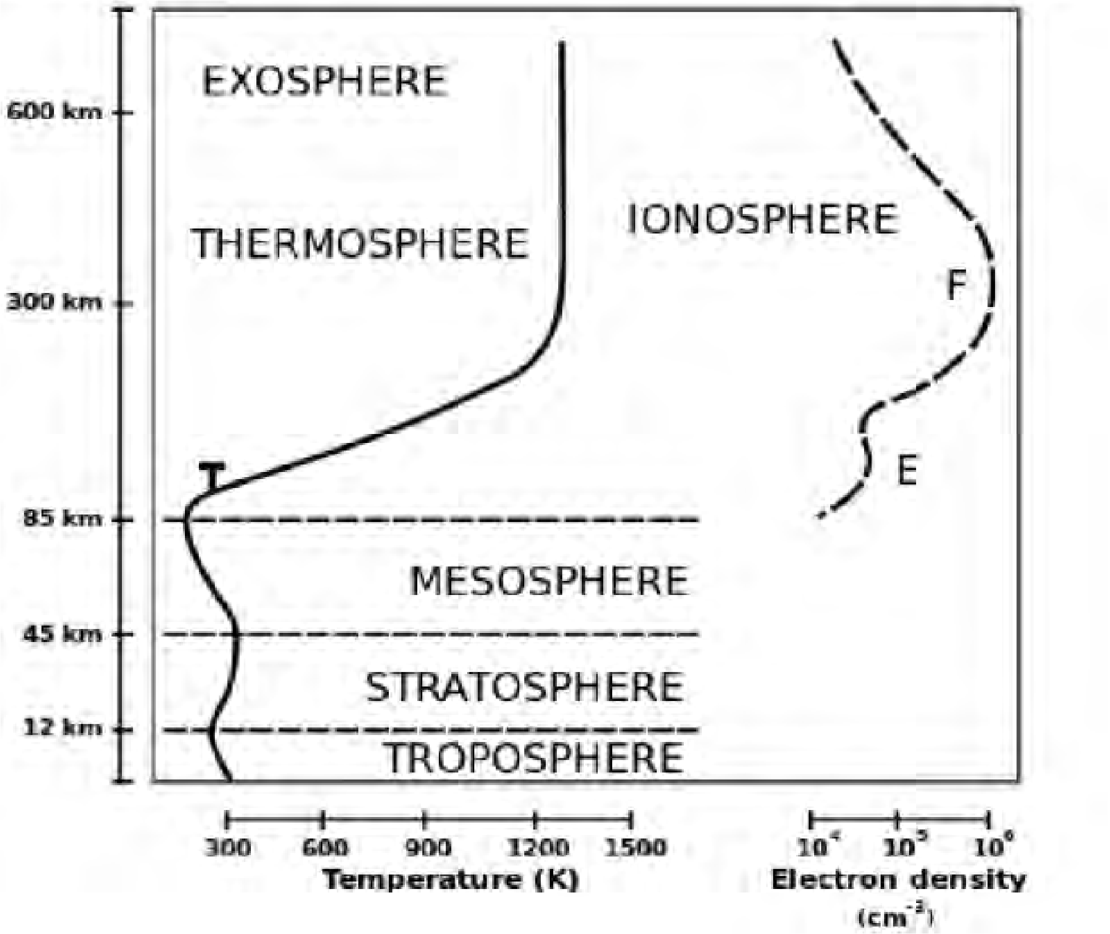

Figure 2.1.: Layers of the Earth's atmosphere: troposphere, stratosphere, mesosphere, thermosphere and exosphere (Hargreaves, 1992).

According to Brekke (2013), N_2 and O_2 are the major neutral components at ionospheric altitudes, with O dominant above ~250 km and N_2 dominating below ~250 km. He and H atoms are common in the topside ionosphere, with H atoms dominating above ~1000 km (Kelley, 2003; Brekke, 2013). Gravitational force is the dominant force acting on neutral particles. To achieve static equilibrium, the gravitational force must be balanced by a net pressure force acting on a parcel of air. Brekke (2013) describes the change in pressure p over altitude z as:

$$\frac{dp}{dz} = -N_n m_n a_g, \qquad 2.1$$

where N_n is the density of the molecules, m_n is their mass, and a_g is the gravitational acceleration. Assuming the atmosphere is an ideal gas, the pressure $p = N_n k_B T$ as a function of altitude z can be obtained from Equation (2.1).

$$p = p_0 e^{-\frac{(z-z_0)}{H}}, \qquad 2.2$$

where $H = k_B T / m_n a_g$ is the scale height, and p_0 is the pressure at z_0, the reference height. According to Brekke (2013), atmospheric neutral species often reach a scale height of around 8.5 km. According to equation (2.2), atmospheric pressure decreases exponentially with altitude. Assuming an isothermal atmosphere, the molecular density N_n at a given height (z) is

$$N_n = N_{n,0} e^{-\frac{(z-z_0)}{H}}, \qquad 2.3$$

$N_{n,0}$ is the neutral density at reference height z_0. Moreover, the density of molecules in the atmosphere decreases exponentially with altitude.

From the Earth's surface, the troposphere reaches up to 12 km, the stratosphere 12 to 50 km, the mesosphere 50 to 80 km, the thermosphere 80 to 700 km, and the Exosphere extends around 10,000 km from 700 km to space (McNamara, 1991; Rishbeth, 1969; Moldwin, 2008). The Earth's ionosphere is an ionized zone between 50 and 1000 km in altitude that is made up of electrons and ions (Rishbeth, 1969; McNamara, 1991; Hargreaves, 1992; Zolesi and Cander, 2014). Because of its characteristics that aid in the reflection of HF radio signals, it is a naturally occurring resource that is used for HF radio applications (Davies, 1990, Hunsucker and Hargreaves, 2002). Extreme ultraviolet (EUV) radiation from the Sun creates the ionosphere when photons interact with neutral atoms to release free electrons. A range of methods and tools, such as radar systems, satellites, and ground-based observatories, are used to study and monitor the ionosphere.

2.2 Formation of the Ionosphere

When these gases are photoionized by highly powerful solar radiation, the ionosphere is created (Ratcliffe, 1960; McNamara, 1991). The intensity of solar radiation reduces when it penetrates the atmosphere from high to low altitudes due to absorption by neutral atoms and molecules. As a result, the lower atmosphere produces less plasma. The density of air atoms and molecules, on the other hand, increases as height drops. Because of the conflicting tendencies in radiation intensity and atmospheric density, the highest electron generation occurs at a high altitude (McNamara, 1991). Some electrons are lost through processes known as attachment and recombination. Electrons are lost by attachment in the lower ionosphere as they directly mix with neutral molecules or atoms to generate negatively charged particles (McNamara, 1991). As solar photons penetrate further into the atmosphere, they produce more ions. When photoionization takes place, the photon flux is weakened until it reaches a depth where the amount of photoionization decreases.
It creates an ionization layer that peaks close to the altitude of maximum production. The photoionization production rate can thus be stated as:

$$q_i = \sigma_i N_j(z) \phi_\infty e^{-\tau}, \qquad 2.4$$

where σ_i is the ionization cross section, N_j is the number density of the ionizable component at altitude z, ϕ_∞ is the solar flux beyond the atmosphere, and optical depth τ is given by

$$\tau = \sigma_a \sec sec\ \chi\ Ndz, \tag{2.5}$$

where σ_a is the absorption cross section and χ is the solar zenith angle. The optical depth τ of the ionosphere measures the attenuation of solar radiation due to absorption by free electrons. Radio communication, satellite navigation, and radar systems all rely heavily on the ionosphere's optical depth. During solar events such as solar flares or geomagnetic storms, greater ionization can cause higher optical depths, resulting in signal degradation or loss, particularly at lower frequencies (Dieminger et al., 1996b).

When electrons mix with oppositely charged molecules or atoms, they generate a neutral gas (Dieminger et al., 1996b). When an electron (denoted by e^-) combines with a positive ion (X^+), a neutral atom (X) is formed, as shown by

$$X^+ +\ e^-\ \rightarrow X +\ \gamma, \tag{2.6}$$

Where γ is a photon. The process is termed as radiative recombination because a photon is produced (Prölss, 2004).

Dissociative recombination is another type of recombination that is most prevalent in the ionosphere. It occurs in two steps; in the first, charge exchange occurs when (X^+) species collide with neutral molecular (A_2) species:

$$X^+ +\ A_2\ \rightarrow AX^+ + A, \tag{2.7}$$

This is known as the α-type reaction, and it happens at the rate L = [$\beta\mathrm{X}^+$], where β is the attachment coefficient and [X^+] is the concentration of X^+ (Ratcliffe, 1960; Hargreaves, 1979). The second stage of dissociative recombination happens when the charged molecule created by the β-type reaction is dissociated by an electron (e^-):

$$AX^+ + e^-\ \rightarrow A + X, \tag{2.8}$$

The rate of this sort of reaction (α-type) is $L\ =\ \alpha N_e^2$, where α is the dissociation coefficient and $\mathrm{N_e}$ is the electron density(Ratcliffe and Holzer, 1973; Hargreaves, 1979; McNamara, 1991; Dieminger et al., 1996b). According to Hargreaves, (1979), β is greater than α in the lower ionosphere, therefore AX^+ is created at a faster rate, leaving the α-type reaction to govern electron loss rate. In contrast, α is larger in the upper ionosphere, implying that electrons rapidly dissolve charged molecules, leaving the β-type reaction to govern neutralization.

2.3 Regions of the Ionosphere

Even though there is intense radiation at altitudes above the F-region peak (~ 200 - 350 km in middle latitudes), ionization is not significant since the atmosphere is thin due to less neutral particles (Hargreaves, 1979; Kamide and Chain, 2007). However, the gas for ionization is rare at lower altitudes, the EUV is weak due to energy loss from absorption at higher altitudes; thus, ionization is low once more. The EUV is powerful enough and there are enough species to ionise at specific altitudes, resulting in maximal ionization. The ionosphere is divided into regions: Bottomside Ionosphere and Topside Ionosphere. The bottomside ionosphere has four regions during the day, called the D, E, F_1 and F_2 regions, since at different altitudes, different atoms dominate and absorb EUV energy at different wavelengths (McNamara, 1991).

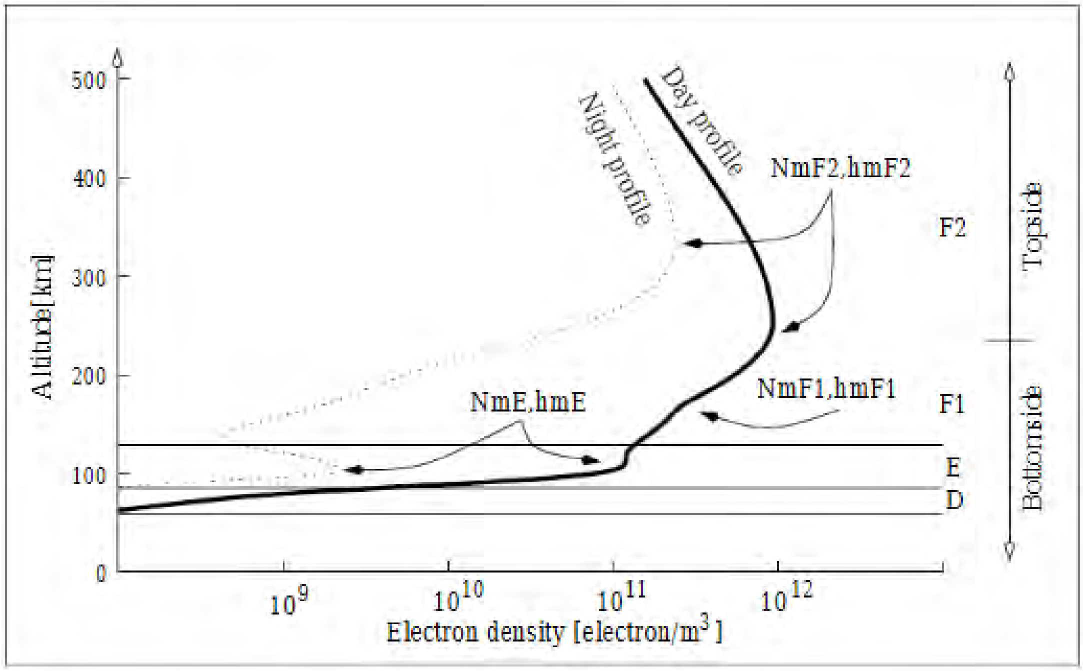

Figure 2.2: The daytime and nighttime vertical profiles of the electron density (Thompson et al., 2017).

2.3.1 D Region

The D region extends from 50 to 90 km above the Earth's surface. It has an electron density of the order of 10^2 - 10^3 cm^{-3} and a neutral atmosphere density of the order of $10^{14}cm^{-3}$. Metal ions such as Ca^+, Fe^+, Na^+ and hydrated ions such as $H_3O^{+,}$ H_5O^+, $H^+ (H_2O)_n$ and others can be found in the D region. In this region, solar X-rays or Lyman alpha ionize NO, and electron attaches to O and O_2 to generate negative ions. Electrons generate negative ions during recombination, which are eliminated by photo-detachment during the day, associative detachment ($O + O^- \rightarrow O_2 + e^-$), and mutual neutralization for A is a neutral atom, $O^- + A^+ \rightarrow O + A$) (Leadon et al., 1981; McNamara, 1991). Furthermore, during solar minimum (which is linked to a decrease in sunspot numbers), when there are more galactic cosmic ray particles entering the Earth's atmosphere, galactic cosmic rays play a crucial role in ionizing this region. This is because galactic cosmic ray particles are able to enter the solar system due to the weakening of the ambient solar wind and its magnetic field (Hargreaves, 1992; Moldwin, 2008). Compared to other ionospheric areas, the D-region has less ionization. Significant x-ray emissions occur during the geomagnetic storms, leading to a sharp rise in ionization (sudden ionospheric disturbances) in this area (Moldwin, 2008). Though a residual ionization level is created at night by galactic cosmic rays, this zone is only present during the day. Because of the recombination process, which creates neutral atoms by combining positively charged ions and negatively charged electrons, it nearly vanishes at night. During the day, photoionization is at its peak, which results in a higher electron density. Here, the atomic molecule density is substantially higher than the electron density (Davies and Harré, 1990; Moldwin, 2008; Zolesi et al., 2014). Solar x-rays are too tiny to constitute a significant contributor to ionization in the D area under typical circumstances (McRae and Thomson, 2004). However, the Sun's X-ray radiation increases dramatically during solar flares. When x-rays with wavelengths considerably below 1 nm are transmitted to the D region's height, the ionization rate and electron density are greatly increased (Mitra, 1974; McRae and Thomson, 2004). Because it absorbs radio waves, which impairs long-distance HF communication, the study and understanding of the D-region is essential to HF radio communication (McNamara, 1991; Moldwin, 2008).

2.3.2 E Region

The E region extends from 90 to 150 km above the Earth's surface. It has an electron density of the order of 10^3 - 10^5 cm^{-3}. The absorption of energy from EUV radiation and solar X-rays ionizes O, O_2, and N_2 in this region. O^+, N^+, and NO^+ are the dominant ions. In this region, dissociative recombination ($O^+ + e^- \rightarrow O + O$) and ($NO^+ + e^- \rightarrow N + O$) occur (Leadon et al., 1981; Kelley and Heelis, 1989; McNamara, 1991; Savage and Sembach, 1996). Another source of ionization in this region is particle precipitation, particularly at night when photoionization is absent (Hunsucker and Hargreaves, 2002; Moldwin, 2008). Furthermore, there exist transient causes of ionization at E-region altitudes, like complex dynamics, which stem from the interaction between auroral electric fields, neutral atmospheric motion, and meteorites penetrating the upper atmosphere. The latter generate an ionized trail by burning up and influencing the surrounding neutral gas with sufficient energy (Rishbeth, 1969; Hunsucker and Hargreaves, 2002; Moldwin, 2008; Zolesi et al., 2014). Known as sporadic E, these sources create a short-lived, narrow zone of extremely concentrated ionization at E-region heights (Rishbeth, 1969; Moldwin, 2008). According to (Hargreaves, 1992; Hunsucker and Hargreaves,,2002) the intermittent Sporadic E has a greater critical frequency than the typical E-region. Sporadic E typically lasts from a few minutes to many hours, depends on the latitude, and occurs at random. The high-frequency radio waves used for long-distance communication are reflected by this extremely intense ionization (Rishbeth, 1969; Moldwin, 2008).

2.3.3 F Region

According to Moldwin (2008), the F layer starts at 120 km and reaches its maximum density at about 300 km. The F layer is mostly formed through EUV ionization of atomic oxygen. During the day, the F layer is divided into two layers: F_1 and F_2. The F_2 layer has the maximum electron density (Davies and Harré, 1990; Hunsucker and Hargreaves, 2002). The F_1 region is within an altitude of about 150 to 200 km above the Earth's surface. It has an electron density of 10^5 - 10^6 cm^{-3}. The major species, O and N_2, are ionised by Lyman, and N_2 ionization disappears after sunset. Most of the ionization is molecular in nature and is eliminated by dissociative recombination (Leadon et al., 1981; Kelley and Heelis, 1989; McNamara, 1991; Savage and Sembach, 1996). The F_2 region is located at about 200 km above the Earth's surface, above the F_1 region. It possesses an electron density of the order of 10^5—10^6 cm^{-3} and neutral atmosphere density of the order of 10^8 cm^{-3}. Because the effective recombination rate falls with increasing ionospheric height, this region contains more ions than others. By using an attachment-like recombination law for charge transfer, molecular recombination is similar to that of the F_1 layer (Leadon et al., 1981; Kelley and Heelis, 1989; McNamara, 1991; Savage and Sembach, 1996).

2.3.4 Topside ionosphere

The O^+ ions make up the majority of the topside ionosphere, which is located at altitudes above the maximum height of the F_2 layer, hmF_2 to around 1000 km (Kamide and Chian, 2007). Height-related decreases in electron density are exponential (Kamide and Chian, 2007). Therefore, this area is unable to reflect any radio waves that are broadcast from the earth. Therefore, it is not possible to observe the topside with ground-based ionosondes. Since 1962, sounders on satellites have provided data regarding topside conditions (Hargreaves, 1992; Dieminger et al., 1996a). TEC of the topside has recently been studied by low Earth orbit satellites, such as SWARM (Pedatella and Forbes, 2011; Buchert et al., 2015) and Constellation Observing System for Meteorology, Ionosphere, and Climate (COSMIC) (Anthes, 2011) amongst other methods.

There is no clear definition for the topside ionosphere's upper boundary. Like other studies (such as Yoshimura et al. (2005) and Marinov et al. (2004)), it is acknowledged to be at the Upper Transition Height (UTH), which is the altitude at which the O^+ and H^+ ion densities are equal. According to this description, the main ion species that contribute significantly to the topside ionosphere are O^+ and H^+ ions. It is presumed that the minor ion is He^+. Heelis et al. (1990) reported theoretical evidence that there may occasionally be a winter nighttime He^+ bulge in this region when the He^+ density increases above the H^+ density. Although the neutral densities of He^+ and H^+ ions are strongly related, the physical mechanisms governing their densities are different. Neutral molecules and atoms have far lower concentrations in the topside ionosphere than they do in the lower ionosphere. Consequently, the majority of the output and loss of Ionization takes place in the lower ionosphere, particularly in the vicinity of the F-region (Webb and Essex, 2000). Thus, there is a close relationship between the dynamics of the lower ionosphere and the electron density distribution in the higher ionosphere. The topside ionosphere's low neutral atom density allows for diffusion to occur quickly enough for the plasma to diffuse away from the F-region ionosphere over a considerable vertical distance in a few hours, covering an atmospheric scale height (roughly 50 km) (Rishbeth, 1975). Therefore, plasma transport processes, field-aligned plasma flows, and chemical processes all affect the dynamics of the topside ionosphere with respect to the distribution and relative amounts of the O^+ and H^+ densities (Venkatraman and Heelis, 1999). Ionization for the topside ionosphere can be both sourced and drained by the F-region.

2.4 Measuring the ionosphere

Early studies of the ionosphere focused on the bottomside, measuring electron density with ground-based ionosondes. Ionosondes have contributed significantly to our understanding of the ionosphere, particularly its bottomside. Since the 1920s, researchers have studied the geographic and temporal aspects of ionospheric electron density (Havens et al., 1954). An ionosonde is a pulsed radar system that sweeps frequencies from 1 to 30 MHz vertically into the ionosphere (Hunsucker and Hargreaves, 2003). Signals are reflected off ionospheric layers. The electron density as a function of altitude above the ionosonde can be determined by monitoring the time it takes for signals to reflect from the ionosphere.Ground-based ionosondes cannot explore the topside ionosphere due to HF radio wave reflections, only able to detect the bottomside (Bilitza, 1994). Radio signals with frequencies higher than the critical frequency of the F_2 layer do not reflect within the F_2-region, resulting in no information. Satellite-mounted ionosondes, also known as topside sounders, revolutionized ionosphere research in the 1960s (Bilitza, 1994).

“Topside sounders measure the topside ionosphere similarly to ground-based ionosondes, which monitor the bottomside. Rockets and Incoherent Scatter Radars (ISR) can be used to study the region above the F_2-layer peak. Rocket-mounted instruments measure ionospheric characteristics, including ion species concentrations and electron/ion temperatures (Bilitza, 1994). However, these metrics are limited and only applicable to the rocket's trajectory. Rocket observations of the ionosphere use "direct" methods, which need only local assumptions and approximations. As a result, only localized measurements are collected, leading to limited conclusions (Bilitza, 1994). ISR are another tool for analyzing electron density distribution in the topside ionosphere. The technique uses a powerful pulsed radar to propagate energy into the ionosphere. Some echos are caused by wave scattering from individual electrons in the ionosphere (Bilitza, 1994). The power of the returning signal is directly proportional to electron density. Ionosondes are pretty good for the study of the E, F_1, and F_2 regions, which span from about 90 to 500 km in altitude. They do not work so well for the D region, 60-90 km, because radio waves are more likely to be absorbed than reflected there (Bilitza, 1994). Here, rockets come into play, for they can sample the D region directly and provide data of immense value that other instruments cannot easily obtain (Bilitza, 1994). ISR are instruments capable of measuring everything from the D region right up to higher layers, offering detailed vertical profiles across the whole ionosphere. GNSS satellites measure the TEC and allow for the creation of an overview on a global scale of the ionospheric conditions, while LEO satellites add localized data, thus providing more detailed information in specific altitude ranges (Bilitza, 1994). The two are instruments with their special characteristics and, therefore, complement each other in providing an in-depth understanding of the ionosphere (Bilitza, 1994).

A topside sounder, like bottomside ionosondes, records ionogram (a picture of reflections and resonances of swept frequencies against apparent range) traces while the satellite travels its orbit (Bilitza, 1994). Using an inversion process, the electron density at a certain time and location within the height range between the satellite height and the peak of the F_2-layer may be calculated from the ionograms. Topside ionograms are easier to invert than bottomside ionograms, which must account for the valley region between the E- and F-layers. Topside ionograms are inverted using the electron density at the beginning location, which is typically obtained from on-board in-situ probe measurements" (Bilitza, 1994).

Satelite Name	Operated By	Launch Date	Data available Until	Orbit Altitude
Alouette-1	USA/Canada	Aug 1962	Sep 1972	1000
Alouette-2	USA/Canada	Nov 1965	Jan 1975	500-3000
ISIS-1	USA/Canada	Jan 1969	Dec 1981	2000-3500
ISIS-2	USA/Canada	Apr 1971	Jan 1983	1400
ISS-b	Japan	Feb 1978	Apr 1983	1100
IK-b	Russia	Feb 1979	Aug 1981	500-1000
Cosmos-1809	Russia	Dec 1986		960

Table 2.1 displays a list of topside sounder missions, their launch dates, and accessible data (Bilitza, 1994).

2.5 Variation of the ionosphere

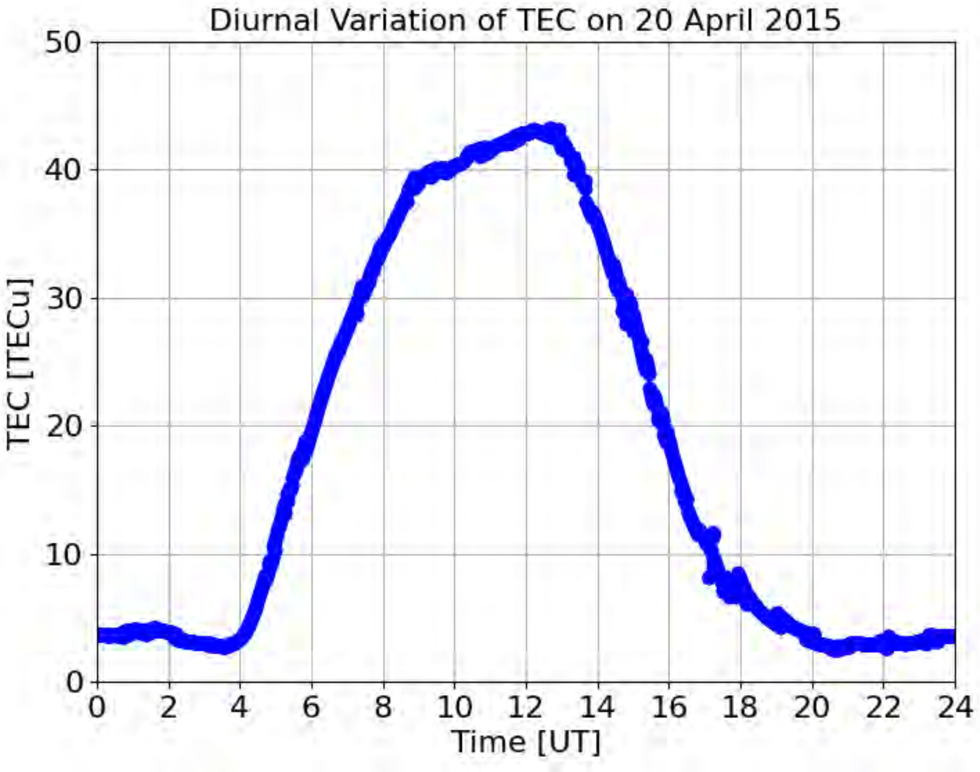

Figure 2.3: A graph illustrating the diurnal variation of average TEC on 20 April 2015 over Aliwal North station (30.68° S, 26.72°E), South Africa.

2.5.1 Diurnal Variations

The ionosphere's electron density fluctuates throughout the day and night. Because the D region is known to absorb HF waves, ionosondes cannot study its diurnal oscillations in the same way that the E and F regions can. However, this does not imply the absence of the D region. According to McNamara (1991), the D region exists throughout the day because of the availability of solar X-rays, which ionize portions of the constituents. The D region disappears at night due to recombination and electron attachment dominates (McNamara, 1991; Dieminger et al., 1996b).

Figure 2.2 indicates that the D region disappears at night due to a lack of solar energy. According to McNamara (1991), the E region does not fully disappear at night, but instead shrinks significantly, making it less reflective of HF waves. The F_1 layer vanishes completely after nightfall since it is indistinguishable from the F_2 layer. Furthermore, the F_2 layer remains throughout the night, as illustrated in Figure 2.2. This is attributed to thermospheric neutral winds pushing the F region plasma upward to low-recombination altitudes (Ondoh and Marubashi, 2001).

The ionosphere's electron density fluctuates throughout the day and night. According to Hofmann-Wellenhof et al. (1992), TEC is determined by electron density, which in turn is determined by solar radiation, the primary source of photoionization. The TEC is calculated by integrating electron density versus altitude (Hofmann-Wellenhof et al., 1992; Zolesi and Cander, 2014). TEC fluctuation is heavily impacted by changes in the intensity of daily solar radiation. TEC achieves its peak values at around local midday, when the solar zenith angle is about zero. The zenith angle is defined as the angle formed by the Sun's rays and the vertical direction. When the solar zenith is zero, the Sun is overhead and photoionization is at its peak. At night, electron loss during recombination causes TEC to decrease. Figure 2.3 shows the diurnal variation of average TEC on April 20, 2015, over Aliwal North station (30.68°S, 26.72°E). TEC was at its lowest between 20:00 UT (22:00 LT) and 24:00 UT (02:00 LT) at night and at its highest between 12:00 UT (14:00 LT) and 14:00 UT (16:00 LT) in the afternoon. The average was determined by taking all the TEC values at a particular epoch, then computing the average TEC value.

2.5.2 Seasonal Variations

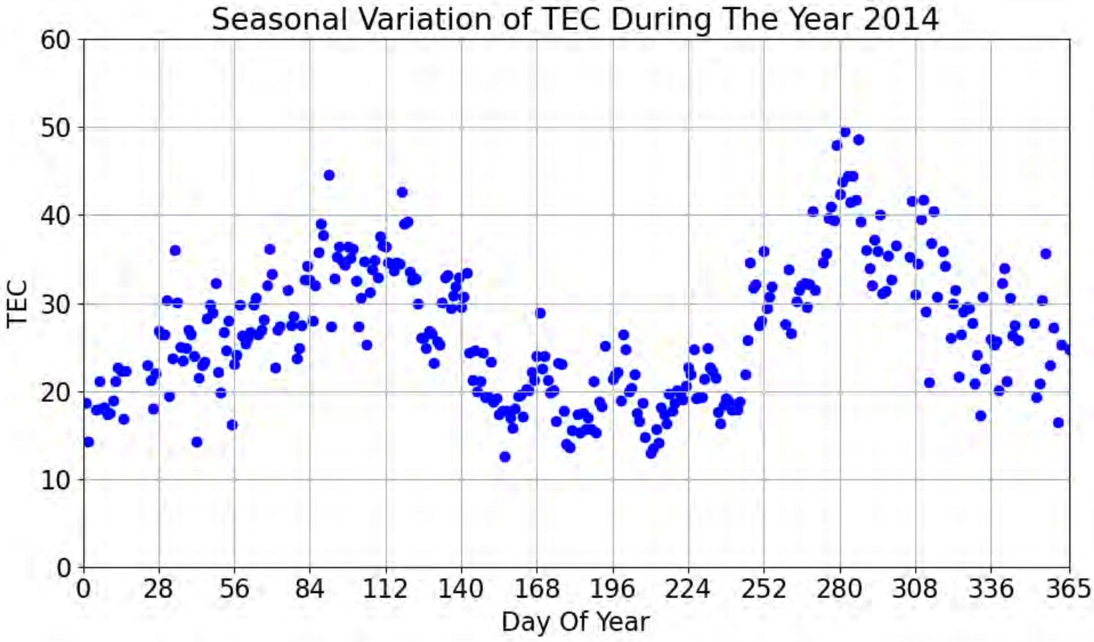

Figure 2.4: Seasonal variation of TEC during the year 2014 over Aliwal North station (30.68°S, 26.72°E), South Africa. at 12:00 UT.

The solar zenith angle, which fluctuates throughout the year, contributes to major seasonal variation in the ionosphere. The ionosphere forms in the neutral atmosphere and changes with the Sun zenith angle. Winter middays have a higher solar zenith angle than summer middays (McNamara, 1991). Summer has higher ionization rates in the ionosphere compared to winter. Seasonal change in electron density in the ionosphere has been observed (McNamara, 1991; Zolesi et al., 2014). TEC levels are highest during the equinox months (March to May and September to November) and summer, and lowest in winter (Rishbeth, 1969; Davies and Harré, 1990; McNamara, 1991; Mukherjee et al., 2010; Patel et al., 2017).

There is an annual anomaly whereby the average ionospheric electron density is higher on the winter solstice compared to summer solstice (Azpilicueta, Brunini and Radicella; 2012). According to Ondoh and Marubashi (2001), the seasonal anomaly is the result of an imbalance in [O_2] and [N_2]. According to Hargreaves (1979), electron generation in the F_2 layer is primarily driven by atomic oxygen, while recombination is driven by O_2 and N_2. During summer, global air circulation reduces atomic oxygen density. The ratios of [O]/[O_2] and [O]/[N_2] decline during summer, indicating decreased electron generation (Hargreaves, 1979). As a result, the electron density in the F_2 layer is higher during the winter than in the summer. Furthermore, there are significant broad peaks in the critical frequency of F_2 layer at equinoxes. These peaks are known as the semi-annual anomaly. According to Zou et al. (2000), this is related to thermospheric circulation. Rishbeth (1969) found that the seasonal trend of [O]/[N_2] is symmetric around winter, resulting in the observed semi-annual anomaly. Figure 2.4 illustrates the variation of TEC over Aliwal North, South Africa, at 12:00 UT (14:00 LT) in 2014. The graph demonstrates that TEC values were significantly higher during the equinox months and summer than in winter. According to Chapman's ionization theory, the solar zenith angle controls the ionospheric electron density. For seasonal variation, electron density should be higher in summer and lower in winter (Davies, 1990; McNamara, 1991; Schunk and Nagy, 2009; Kelley, 2009; Mukherjee et al., 2010).

2.5.3 Solar Cycle Variations

The Sun's impact on the creation of electrons in the ionospheric layer varies with changes in solar emission activity across time (Hargreaves, 1979). A solar cycle lasts around eleven years. The quantity of sunspots on the surface of the Sun is a measure of its activity, with the number of sunspots reaching its peak during periods of high solar activity and its lowest during periods of low solar activity. Solar x-rays and EUV radiation change over the solar cycle. X-ray and EUV radiation levels are higher during the solar maximum compared to the solar minimum period. The ionosphere produces more electrons during solar maximum (McNamara, 1991; Hargreaves, 1992; Zolesi and Cander, 2014). The interaction of solar flare radiation with ionosphere constituents causes immediate increase in electron density in the ionosphere. Flare-enhanced photoionization at various altitudes in the ionosphere abruptly increases the TEC, causes short radio wave fadeout and sudden frequency deviation, and alters field-aligned plasma motion (Mendillo et al. 2018; Liu et al. 2022). Figure 2.5 shows how VTEC varies between high and low solar activity over Aliwal North station (30.68°S, 26.72°E) during the March and September equinoxes, as well as the June and December solstices. High solar activity leads to higher photoionization rates, resulting in higher TEC values. Solar flares, which create high levels of ionization in the ionosphere, are more frequent during periods of high solar activity (Davies, 1990; Saha, 2008; Zolesi and Cander, 2014).

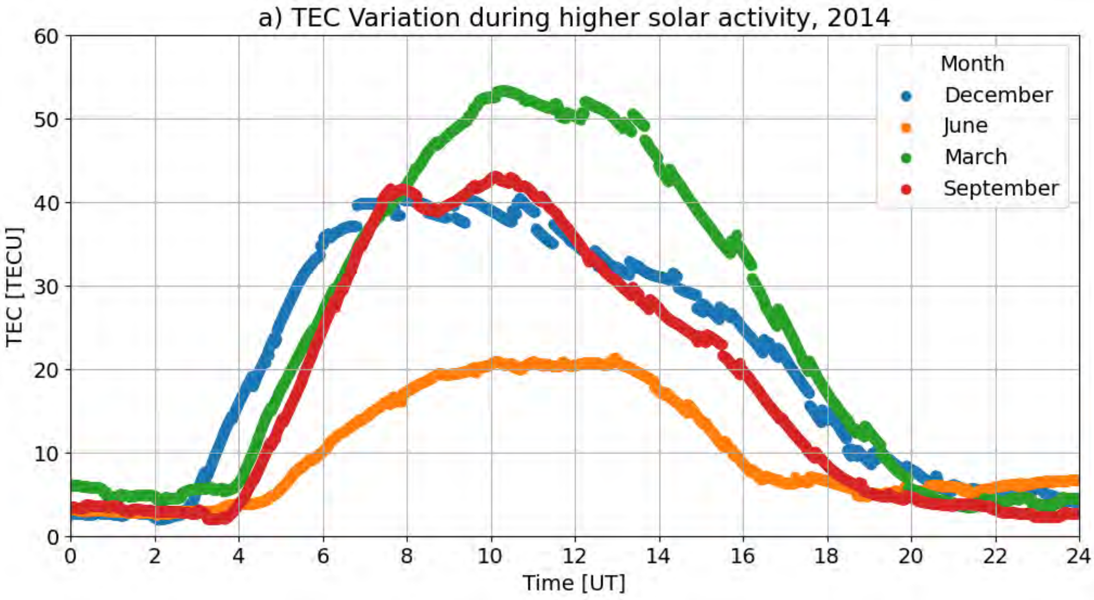

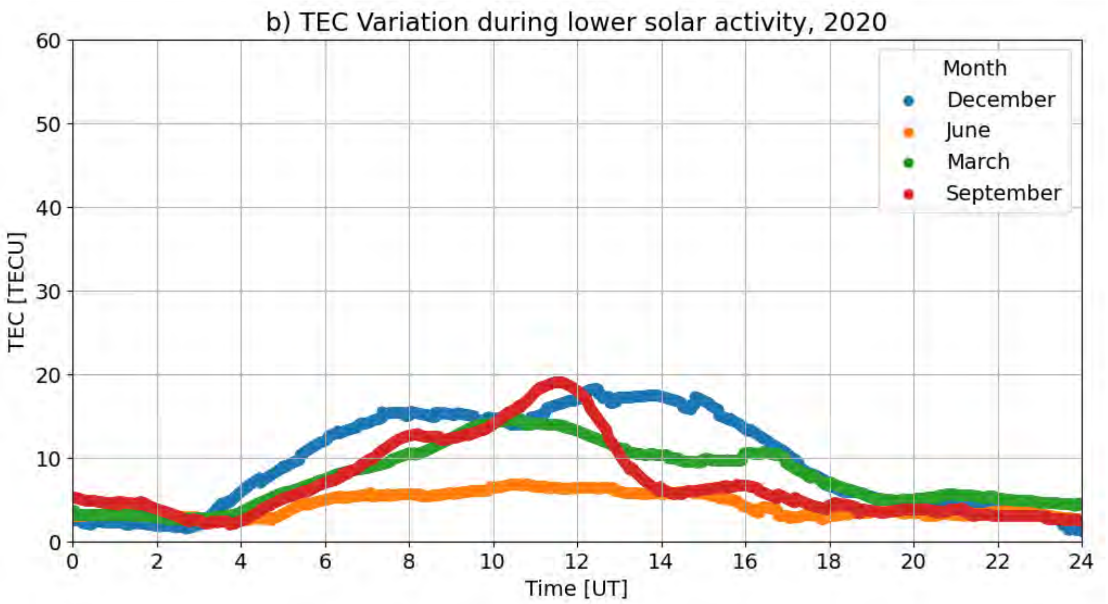

Figure 2.5: (a) Average TEC variation for the 20 March 2014 and 23 September 2014 equinoxes, and for solstice days 21 June 2014 and 22 December 2014 over Aliwal North station (30.68°S, 26.72°E), South Africa. (b) illustrates the TEC variation during the equinoxes of 20 March 2020 and 22 September 2020, and during solstice days on 20 June 2020 and 21 December 2020

Solar activity in the ionosphere causes variations in neutral density, neutral wind, ion and electron densities, temperature, and electric fields (Mukherjee et al., 2010; Liu et al., 2011).

2.5.4 Latitudinal Variation

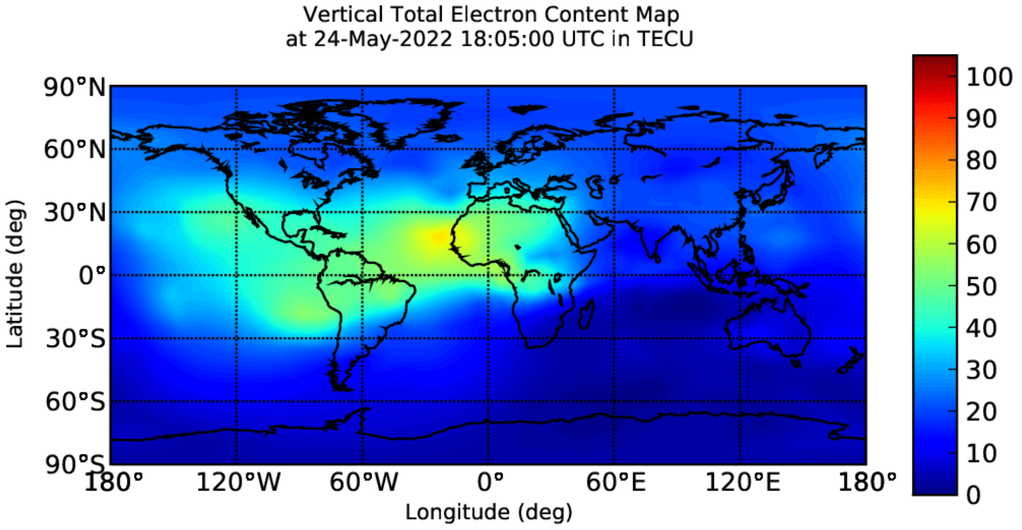

Figure 2.6: Global ionospheric TEC map (GIM) generated at Jet Propulsion Laboratory (JPL) using GNSS data for 18:05 UTC on 24 May 2022 (Pi et al.,

2021).

The intensity of radiation and daily production of free electrons reduces as latitude increases, since solar radiation enters the atmosphere more obliquely. The ionosphere can be divided into three sections (low-latitude, mid-latitude, and high-latitude) with distinct features. Figure 2.6 shows the global ionospheric TEC map at 18:05 UTC on 24 May 2022. The TEC gradually decreases with increasing latitude.

2.5.4.1 Low Latitude Ionosphere

In the low-latitude region, the ionosphere is deformed with a depletion in electron density across the geomagnetic equator and substantial enhancements occurring around ±20° north or south of the magnetic equator. This phenomenon is induced by the "fountain effect": an electrodynamic lifting of the plasma that drifts upwards until the pressure and gravity forces are high enough, at which point the plasma is driven back through the magnetic field lines to higher latitudes. This effect is caused by the geomagnetic field running horizontally over the geomagnetic equator, resulting in strong electromagnetic forces that lead to abnormally high electrical conductivity over the equator and a strong electric current (an "electrojet") flowing in the E and F regions. Thus, the equatorial ionosphere is higher in height than the mid-latitudes, with electron density dropping to a minimum near the magnetic equator and reaching a maximum at 15°-20° latitude on both sides of the geomagnetic equator (Kelley, 2009; Zolesi and Cander, 2014). This occurrence is referred to as the equatorial ionization anomaly (EIA). The EIA begins at around 10:00 LT in the morning, lasts until sunset, and covers over half of the world in 24 hours (Balan, Liu, and Le, 2018). Geophysical factors affect the location and ratio of crest-to-trough (Kelley et al., 2004; Kelley 2009). Local EIA regions can become unstable at night, particularly in the evening when only the high-altitude F region ionosphere remains (Eastes et al., 2019). The EIA is caused by a daytime eastward electric field around the equator. The position and intensity of the EIA's two crests alter due to fluctuations in electric fields and neutral winds (Kelley et al., 2004; Kelley, 2009). Figure 2.7 illustrate the concept and mechanism of EIA.

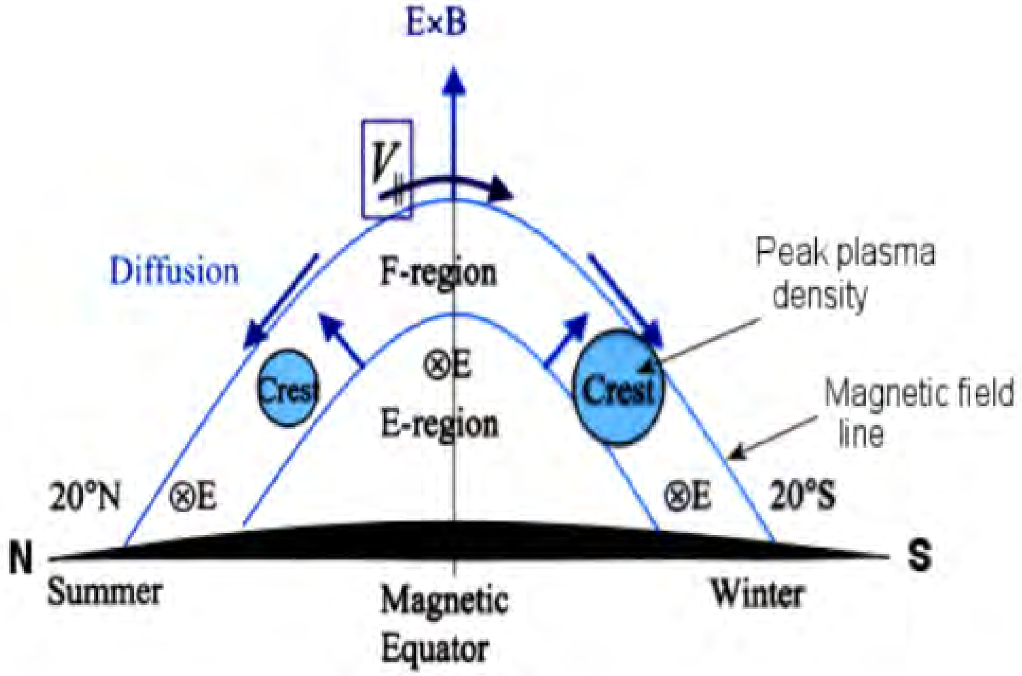

Figure 2.7: Schematic of the EIA, upward plasma drift and following the downward diffusion along the field lines are shown by the arrows, producing the fountain effect. (Anderson, 2004).

2.5.4.2 Mid Latitude Ionosphere

The mid-latitudinal ionospheric geomagnetic latitude spans from 30° to 60° on both sides of the geomagnetic equator. The mid-latitudinal ionosphere is less complicated than other latitudes under normal solar-terrestrial settings, with a minor spatial gradient that changes slowly (Zolesi and Cander, 2014). At mid-latitudes, magnetic field lines containing high-density plasma are substantially shorter, gravity works parallel to the magnetic field, and wind effects are at least as strong as electric fields (Hunsucker and Hargreaves, 2007; Kelley, 2009; Zolesi and Cander, 2014). The shielding effect of the Alfvén layer prevents the magnetospheric electric field from having a major impact on the mid-latitude quiescent ionosphere (Huba et al., 2005; Kelley, 2009). The mid-latitude ionosphere is quiescent plasma under geomagnetically quiet conditions, but the plasma density varies due to both plasma and neutral processes (Titheridge, 1995; Tsugawa et al., 2004). The irregularity of the ionosphere during geomagnetic storms at mid-latitudes is powerful enough to induce changes in signal power, known as ionospheric scintillation. Irregularities in radio waves can induce amplitude and phase scintillation, impacting satellite communications and GPS navigation systems (Basu et al., 2001, 2002; Mishin et al., 2003). During the solar maximum, mid-latitude scintillation peaks, ionization density in the F-region rises, and anomalies emerge against this background (Basu et al., 2002; Heelis, 2004; Kelley, 2009). Scintillation occurs less frequently in the mid-latitude ionosphere compared to low- and high-latitude ionospheres (Basu et al., 1988, 2002; Kuai et al., 2022). Ionospheric scintillation transpires often in low latitudes between sunset and evening hours (Abdu et al., 1985; Muella et al., 2010; Liu et al., 2015), as well as in high latitudes (Kersley et al., 1988; Secan et al., 1997; Jiao et al., 2013). During geomagnetic storms, the auroral zone expands towards the equator and diminishes at mid-latitudes (Zolesi and Cander, 2014). Photoionization is the primary source of ionization in the mid-latitude ionosphere, resulting in significant diurnal, seasonal, and solar cycle changes (Rishbeth and Garriott, 1969; Saha, 2008; Heelis, 2004; Kelley, 2009; Schunk and Nagy, 2009; Zolesi and Cander, 2014).

2.5.4.3 High Latitude Ionosphere

The high latitude ionosphere has geomagnetic latitudes ranging from 60° to 90° on either side of the equator (Schunk and Nagy, 2009; Zolesi and Cander, 2014). High-latitude regions experience the most variability due to their connectivity to the outer magnetosphere and interplanetary medium through field lines. The geophysical environment and internal processes have a significant impact on the system. The magnetosphere's electric field causes large-scale mobility in the high-latitude ionosphere, impacting electron density morphology. According to (Rishbeth and Garriott, 1969; Schunk and Nagy, 2009; Zolesi and Cander, 2014), ion-neutral frictional heating causes an increase in ion temperature as plasma moves through neutral particles. As ion temperature increases, the chemical kinetics of the ions, topside plasma scale heights, and ion composition varies. Furthermore, particle deposition in the auroral oval boosts ionization rates and electron temperatures. This has an impact on ion and electron density as well as temperature. Ionospheric changes influence the thermosphere's structure, circulation, and composition (Kelley, 2009; Schunk and Nagy, 2009; Zolesi and Cander, 2014).

The Sun's low elevation leads to weak ion formation from EUV and X-rays, while high-energy charged particles mostly contribute to ion generation at high latitudes (Saha, 2008; Schunk and Nagy, 2009). At geomagnetic latitudes over 75°, the polar ionosphere dissipates solar wind energy, which can significantly impact the upper atmospheric energy balance. Energy is dispersed through heat, wind, and waves (Schunk and Nagy, 2009; Kelley, 2009). The high-latitudes are known for the main ionospheric trough (MIT), which affects electron density in the F-region during the night. Taylor Jr. et al. (1975) and Zolesi and Cander (2014) describe an ionized latitudinal patch in the afternoon sector at around 70° magnetic latitude as the natural barrier between the mid-latitudes and the auroral ionosphere. The MIT is also known as the mid-latitude ionospheric trough (Moffett and Quegan, 1983; Lubyk et al., 2022). The MIT is a crucial component of the subauroral ionosphere, occurring frequently during winter nights. According to Karpachev and Afonin

(1998) and Karpachev et al. (2016), 90-95% of MIT observations occurred during periods of high solar activity. Higher illumination of the high-latitude ionosphere reduces the likelihood of a midday MIT (Karpachev et al., 2022). The MIT's location is determined by local time, longitude, and magnetic activity (Ahmed et al., 1979; Karpachev and Afonin, 1998).

2.6 Geomagnetic Storms

According to Hargreaves (1992), a geomagnetic storm is characterized as a significant deviation from typical ionospheric or geomagnetic behaviour and typically lasts for one to several days. Significant variations in the geomagnetic field are characterized as geomagnetic storms (Hargreaves, 1992; Gonzalez et al., 1994). Charged particles from solar winds that interact with the geomagnetic field can be the source of these variations. An interplanetary magnetic field (IMF) in a solar wind that is headed toward Earth interacts with the geomagnetic field when it arrives (Hargreaves, 1992; Gonzalez et al., 1994). When the Earth's magnetosphere is exposed to solar wind particles, a geomagnetic storm happens as a result of the interaction between the southerly component of the IMF and the geomagnetic field (Dieminger et al., 1996b; Tsurutani and Gonzalez, 1997; Borovsky and Denton, 2006). According to Borovsky and Denton, (2006), solar winds that are delivered to the geomagnetic field by coronal mass ejections (CMEs) or corotating interacting regions (CIRs) are typically responsible for geomagnetic storms.

2.6.1 Causes of geomagnetic storms

Geomagnetic storms are generally caused by CMEs, interplanetary shocks, and CIRs formed by slow and fast solar wind streams (Hargreaves, 1992; Tsurutani et al., 2006; Moldwin, 2008). According to Hargreaves (1979), a CME is a huge cloud of charged particles that the Sun releases, usually during solar maximum. According to Borovsky and Denton, (2006), a coronal hole, or low temperature zone, on the photosphere releases charged solar particles at high speeds into a CIR. When the fast, extremely intense CMEs stream away from the Sun, they create shock waves in front of them (Crooker et al., 1997; Moldwin, 2008). Shock waves are crucial in accelerating solar energetic particles (SEPs) (Crooker et al., 1997). A CME's transit duration from the Sun to the Earth ranges between one and five days, depending on its initial velocity, mass, and size, as well as the circumstances and coupling processes with the ambient solar wind flow in interplanetary space (Crooker et al., 1997; Moldwin, 2008; Temmer, 2016). The CMEs have greater magnetic fields than the ambient solar wind, resulting in a compacted magnetosphere. This energy may trigger a geomagnetic storm, which would intensify the Van Allen radiation belts and produce an aurora (Moldwin, 2008). CMEs can generate geomagnetic storms and ionospheric disturbances (Gopalswamy, 2006). CMEs, which occur during the solar maximum, are the primary cause of big magnetic storms with more severe societal repercussions than CIR storms (Webb, 1991; Turner et al., 2009).

Moderate geomagnetic storms are mostly caused by CIRs that intrude on the magnetosphere (Tsurutani et al., 2006). CIR-driven storms occur when the rapid solar wind from a coronal hole interacts with the slow solar wind of the interplanetary medium (Moldwin, 2008; Tsurutani et al., 2006; Turner et al., 2009; Richardson, 2018). When rapid and slow solar winds interact, the plasma compresses near the boundary, which results in enhancing the density of the slow wind zone. The fast solar wind's plasma converts kinetic energy into thermal energy, causing heating and decreasing plasma density (Akasofu, 1981; Bagh et al., 2000; Turner et al., 2009). Disturbance storm time (Dst) index assesses the intensity of the Earth's equatorial magnetic field due to particle injection into the magnetosphere (Tsurutani et al., 1997; Echer et al., 2011).

During a magnetic storm, electric currents known as ring currents surround the Earth (Hargreaves, 1979). During the main phase of a geomagnetic storm, particles are injected into the magnetosphere, causing ring current to grow. As the ring current rises, Dst decreases. According to Parkinson (1983), Davies (1990), Campbell (2001) and Tsurutani (2001), the Earth's magnetic field weakens due to the ring current encircling it. Four near-equatorial geomagnetic observatories measure hourly averages of the horizontal component of the Earth's magnetic field to calculate the Dst index (nT) (Campbell, 1997). The Dst index describes only the zonal average disturbance, not its local dependence. The Dst index is provided by

$$Dst = \frac{1}{N}\frac{\Delta H - H_q}{cos\ \beta} \qquad 2.9$$

where β is the geomagnetic latitude of the station, ΔH is the horizontal component of the magnetic field without the nightime baseline value and Hq is the horizontal components of the magnetic field disturbance on the quietest day at a specific station, and N is the total number of stations. The cos β coefficient seeks to normalize magnetic disturbances to equator values at different latitudes (Kamide and Maltsev, 2007). The Dst index is calculated using four ground-based magnetic stations: San Juan, Honolulu, Kakioka, and Hermanus.

Observatory	Geographic Longitude [°]	Latitude [°]	Dipole Latitude
Hermanus	19.22	-34.40	-33.3
Kakioka	140.18	36.23	26.0
Honolulu	201.98	21.32	21.1
San Juan	293.85	18.01	29.9

Table 2.2: The network of magnetometers that are used to derive the Dst index

These four observatories were chosen for their proximity to the magnetic equator, making them less affected by the auroral current system. Furthermore, their location far from the magnetic equator reduces their exposure to the equatorial electrojet current in the ionosphere (Wanliss and Showalter, 2006).

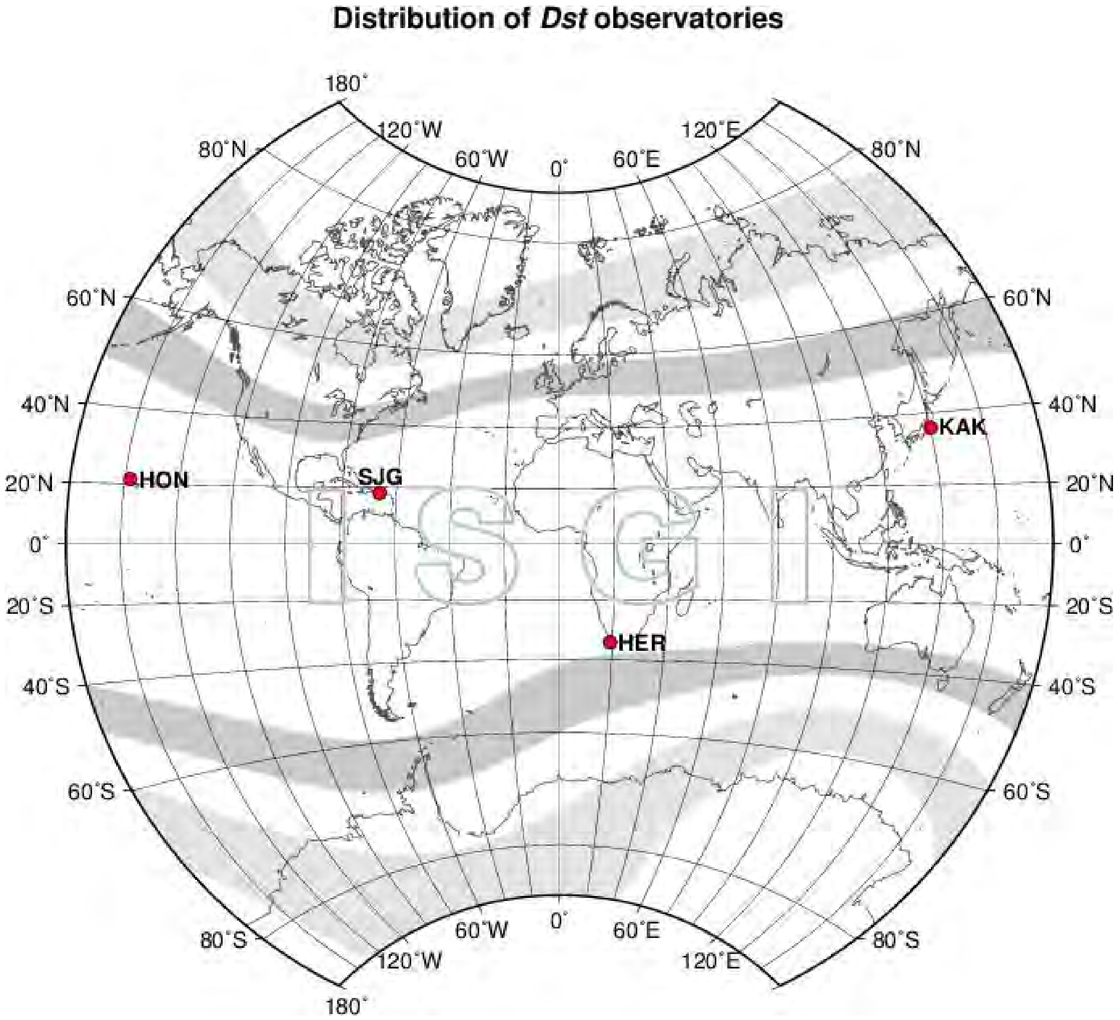

Figure 2.8: A map showing the network of magnetometers that are used to derive the Dst index (http://isgi.unistra.fr/index.php).

Geomagnetic storms are classified as weak, moderate, intense, strong, or great depending on their Dst levels (Prölss, 1995).

Table 2.3: Categories of a geomagnetic of storm according to the Dst index (Loewe and Prölss, 1997).

Dst Index (nT)	**Category**
$-30 \geq$ Dst > -50	Weak
$-50 \geq$ Dst > -100	Moderate
$-100 \geq$ Dst > -200	Intense
$-200 \geq$ Dst ≥ -350	Strong
Dst < -350 Great	Great

2.6.2 Phases of Geomagnetic Storms

A divergence of electron density from normal behaviour in reaction to magnetic storms is known as an ionospheric storm (Hargreaves, 1992). Ionospheric storms are classified as positive or negative depending on how much electron density is present in the ionosphere (McNamara, 1991). The electron density is increased during a positive storm; this is indicated by a decrease in the reflection height for extremely low frequency waves (Hargreaves, 1992) and an increase in HF wave absorption (Ratcliffe, 1960) and for extremely low frequency waves, by a smaller reflection altitude (Hargreaves, 1992). This impact mostly manifests itself during the primary phase of magnetic storms; however, in the case of major storms, it may continue into the recovery period, a phenomenon referred to as post storm effects (Hargreaves, 1992). A geomagnetic storm comprises three phases:

(1) Initial phase (IP): During this phase, the geomagnetic field or its measurement (Dst) rapidly increases due to a stream of protons and electrons brought in by the solar wind for a few minutes. These hit the Earth's magnetopause, causing Sudden Commencement (SC) or Sudden Storm Commencements (SSC). Note that geomagnetic storms have SSC. This is part of an initial or positive phase that can endure for a few hours, resulting in an increase in the geomagnetic field (Dst) (Koskinen, 2011).

(2) Main phase (MP): This phase begins when the H component of the magnetic field at the equator drops due to the westward ring current that circles the Earth. Particles of different energies/species do not reach near the Earth at the same moment because their velocities differ. This phase may last several hours. As the density of the stream decreases, so does Dst, until it achieves its minimal value. During the storm's main phase, a ring of energetic particles surrounds the Earth (Tsurutani et al., 1997; Moldwin, 2008). The main phase of a CME-driven storm might span a few hours or perhaps a day (Borovsky and Denton, 2006; Matamba and Habarulema, 2018). The CIR-driven storm has a weak to moderate intensity (-30 nT > Dst > -75 nT) during its main phase, which lasts roughly a day (Davies, 1990; Campbell, 2001; Moldwin, 2008).

(3) Recovery phase (RP): In this phase, the IMF goes north and the ring current decays, eventually increasing the Earth's magnetic field. The Dst gradually returns to the quiet time value, and this phase can extend for several hours or days. Geomagnetic storm recovery time is longer for CIR-driven storms compared to CME-driven ones. According to Tsurutani et al. (1997) and Borovsky and Denton (2006), the recovery phase of a CME storm may endure up to two days. CME-driven storms have high maximum energy intake but short duration. CIR-driven storms have a lower maximum energy intake, but last longer (Borovsky and Denton, 2006; Chen et al.,

2014). Storms induced by CIR and CME are categorized based on proton temperature, solar wind velocity, magnetic field, and proton density (Borovsky and Denton, 2006; Richardson and Cane, 2010; Richardson, 2018).

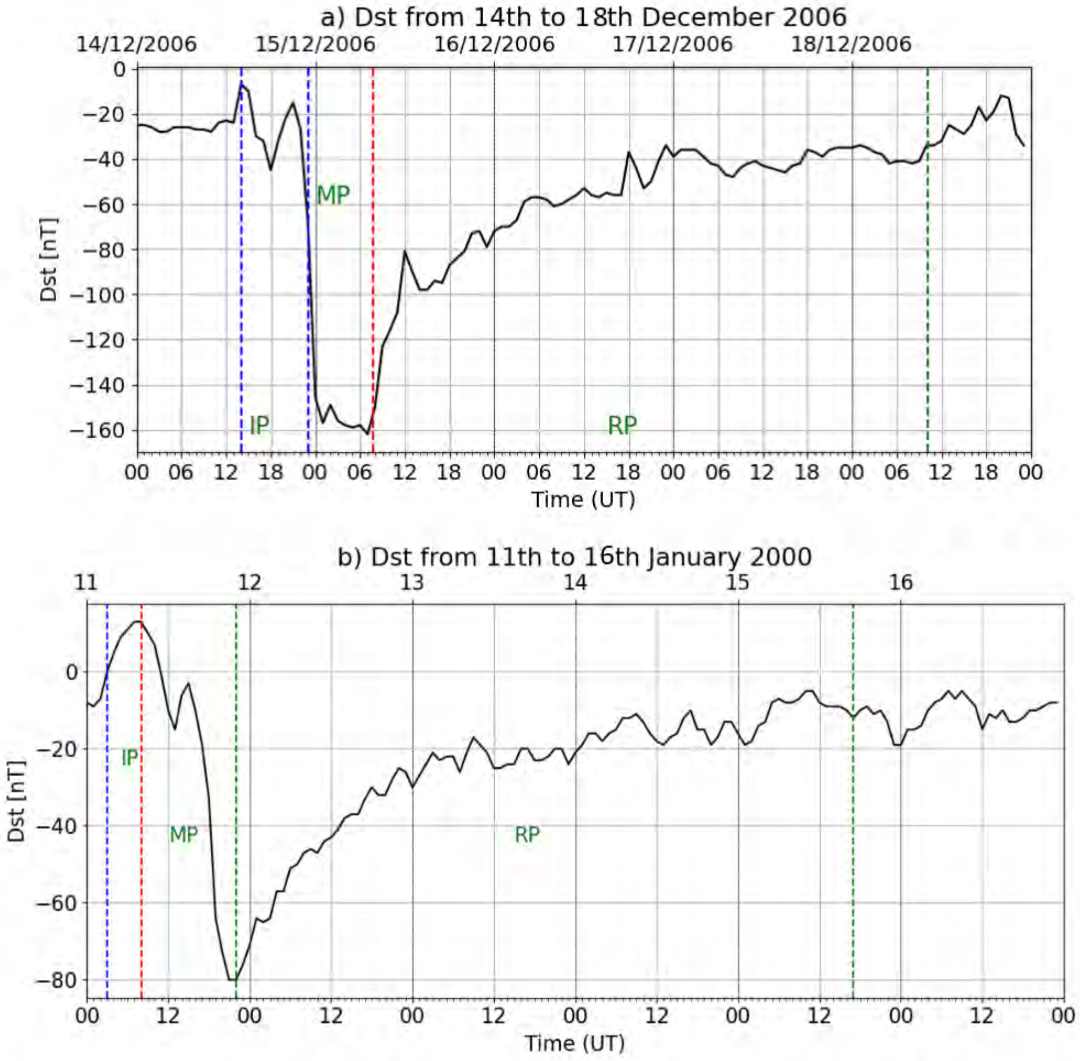

Figure 2.9: Dst index variations during a) CME-driven and b) CIR-driven geomagnetic storms.

Figure 2.9 shows the three phases of the geomagnetic storms that occurred on 14-18 December 2005 and 11-16 January 2000. The two panels show the Dst index for two independent geomagnetic storm events. Panel (a) shows the Dst index from 14th to 16th December, 2006, describing a intense geomagnetic storm. In the main phase of 15th December, the Dst index decrease steeply to a minimum of nearly -160 nT, showing an intense geomagnetic disturbance. This is followed by a gradual Recovery Phase. The initial and main phases are well defined with a rapid transition into recovery.

Panel (b) shows the Dst index from 11th to 17th January 2000. This storm was of lesser magnitude as compared to the December 2006 event. The Dst index had a minimum of about -80 nT. The Initial and Main Phases both occur on the 11th and 12th of January respectively. Compared to the storm of December 2006, this has a more gradual decrease in Dst index. There shortly follows a Recovery Phase after the Main Phase, though the Dst index is relatively low throughout, indicating a slower recovery. What is observed is that the storm in December 2006 was intense, with a faster recovery phase, the January 2000 storm was moderate, and was more gradual in its recovery phase. The December 2006 storm features a sudden storm commencement (SSC) which is not observed in the January 2000 storm.

2.6.3 Negative effect of geomagnetic storms on the ionosphere

A rapid expansion of polar ionization enhancement caused by increased energy input at high latitudes causes an upwelling of the neutral atmosphere and a decrease in the atom-to-molecule ratio as air of different composition (with fewer light atoms/molecules) is raised to high altitudes (Prölss, 1995; Blagoveshchenskii, 2013; Rukundo, 2023; Rajana et al, 2024). Rapid heating and expansion of the atmosphere at high latitudes creates a pressure gradient, which alters global thermospheric circulation and leads to stronger equatorward winds (Chamberlain, 1987; Prölss, 1995; Schneider, 2006; Nugent, 2019). Because of the shift in chemical composition, recombination rises in the ionosphere, reducing electron density. For example, oxygen depletion and inhancement of molecular nitrogen concentrations are essential in studying the ionosphere during geomagnetic storms because they diminish ionization density at F_2-region altitudes (Prölss, 1995). At the F_2-region altitude, ionization is produced through photoionization of atomic oxygen. With the assumption that the atmosphere is optically thin, the production rate (q) is exactly proportional to the atomic oxygen density ([O]) (Prölss, 1995; Mansilla, 2012).

$$q = \ J_o[O], \qquad 2.10$$

where J_0 is the ionization frequency of this element. The loss of ionization at the F_2-region altitude is produced by charge transfer reactions of the following type:

$$O^- + \ N_2 \ \xrightarrow{k_1} \ NO^+ + N \ , \qquad 2.11$$

$$O^- + \ O_2 \ \xrightarrow{k_2} \ O_2^+ + O, \qquad 2.12$$

where k_1 and k_2 are the corresponding reaction rate constants. Dissociative recombination destroys the resultant molecular ions, N O^+ and ${O_2}^+$. The loss rate can be expressed as:

$$l(N) = \beta[O], \qquad 2.13$$

where N denotes electron density; O depends on the density of the molecular gases N_2 and O_2.

$$\beta = k_1 [N_2] + k_2 [O_2] , \qquad 2.14$$

The measured composition changes are utilized to determine storm effects by computing the disturbed-to-undisturbed O and N_2 values. The ratio R(n) is the storm-time value of the gas element n divided by the relevant quiet-time value.

$$R(N_m) \cong \frac{R(O)}{R(N_2)} = R\left(\frac{O}{N_2}\right), \qquad 2.15$$

where N_m is the maximum electron density and is given by

$$N_m = \frac{q}{\beta} , \qquad 2.16$$

An increase in N_2 density and a fall in O density implies a decrease in $[O]/[N_2]$, which results in a decrease in electron density, because a recurring decrease in O density reduces the rate of ionization (Prölss, 1995; Blagoveshchenskii, 2013; Rukundo, 2023; Rajana et al., 2024).

Electric fields are responsible for electron transport and increasing the loss of ionization. The reason for this is that the reaction rates of the constants k_1 and k_2 are strongly correlated with both the ion temperature and the relative flow speeds of the interacting gases (Prölss, 1995). At higher latitudes, k_1 is proportional to the square of the effective temperature. Electrodynamic heating causes the effective temperature to rise roughly in proportion to the square of the effective electric field strength (Prölss, 1995; Blagoveshchenskii, 2013; Rukundo, 2023; Rajana et al., 2024). Chemical loss rates influence plasma density, and any chemical change (not driven by dynamics) results in the production of vibrationally excited molecular nitrogen. These species increase the plasma loss coefficient, and the increased loss rate causes large decreases in the F_2-region electron density (Fuller-Rowell et al., 1994). The rise in the loss rate results in visible gaps in the plasma density and the creation of new troughs at both sub- and transauroral latitudes (Fuller-Rowell et al., 1994; Prölss, 1995).

During geomagnetic storms, Joule heating induces a significant upwelling of the atmosphere around the auroral oval, resulting in a range of physical and chemical changes in the atmosphere (Chamberlain, 1987; Prölss, 1995; Schneider, 2006; Nugent, 2019). Particle precipitation is a significant source of ionization in the polar ionosphere, particularly during solar eclipses and winter solstices. During strong disturbance conditions, particle precipitation increases density at higher latitudes (Prölss, 1995). Joule heating and electrodynamic drift are linked to auroral electrojets (Figure 2.10). During a geomagnetic storm, Joule heating can account for 50.0% of total energy input to the ionosphere (Fuller-Rowell et al., 1994; Danilov and Laštovička, 2002; Burns et al., 2007; Mansilla, 2012). This energy input is the result of an Ohmic interaction between some currents and the electric field in the ionosphere.

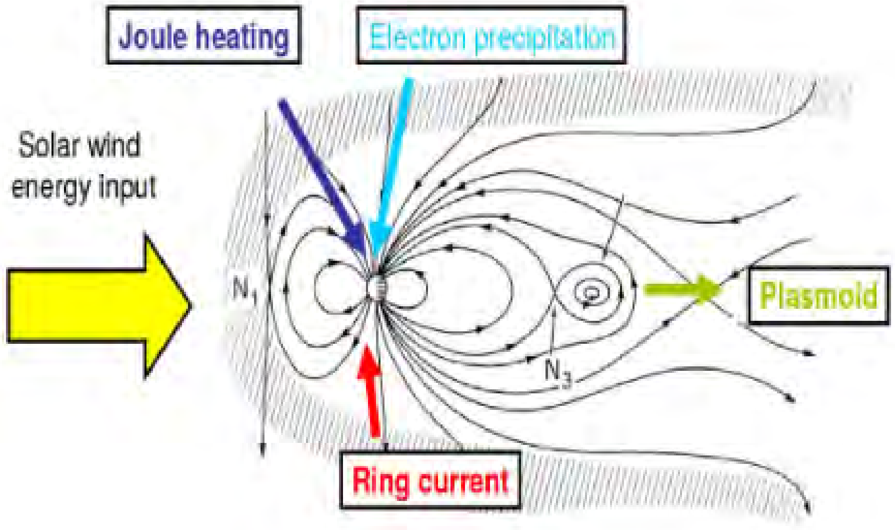

Figure 2.10: The Joule heating, the electron precipitation and the ring current in the ionosphere(Kamide and Baumjohann, 1993; Stern, 1996).

Convergence winds generate an increase in mean molecular mass in the upwelling zone, while decreasing it in the downwelling region. This rise causes negative storms at higher latitudes. Upwelling and increased molecular oxygen speed up ion recombination, resulting in lower plasma density (Fuller-Rowell et al., 1994). During a geomagnetic storm, Joule heating at high latitudes reduces the poleward wind on the dayside and strengthens the equatorward wind on the nightside, resulting in a storm circulation that transports air with more molecular species. Increasing the number of molecular species leads to more O^+ recombination and lower electron density in the F_2 area (Huang et al., 2005; Burns et al., 2007; Mansilla, 2012).

Particle precipitation induces thermal expansion and massive upward flows, exacerbating the drop in ionization density. Figure 2.10 illustrates how neutral composition variations might create disturbances in polar regions. During a geomagnetic storm, shifting the auroral oval towards the equator might result in unfavorable storm impacts due to energetic particle precipitation (Danilov and Laštovička, 2002; Lekshmi et al., 2011). The majority of the energy in the form of energetic particle precipitation (kinetic energy) is related with the cross-polar cap potential decrease, rather than the auroral oval. During the evening, the auroral oval shifts toward the equator, causing flux tubes to stay in a region where recombination occurs but not production (Fuller-Rowell et al., 1994; Danilov and Laštovička, 2002; Burns et al., 2007).
During polar cap growth, rapid ion fluxes through dayside convection enhance the rate of recombination in the F_2-region, leading to ionization depletion (Yizengaw et al., 2005).

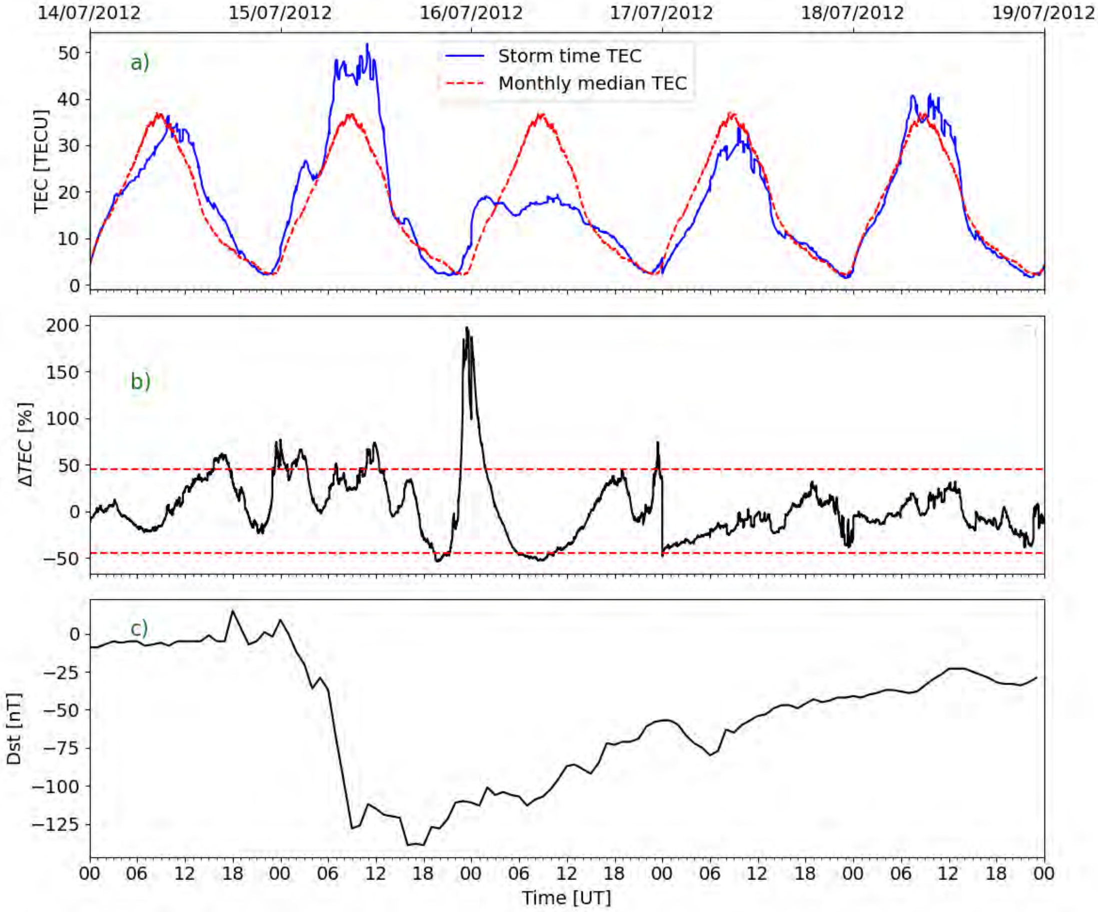

Figure 2.11: Storm effect on TEC over GRHI Gorahi (27.95°N, 82.49°E), India

During geomagnetic storms, the behavior of the ionosphere can change, causing plasma density to increase or decrease (Rishbeth 1963; McNamara 1991; Moldwin 2008). A positive or negative ionospheric storm is defined as an increase or decrease in plasma density. The ionosphere's response to geomagnetic storms is important for system researchers and model developers because it allows them to characterize the formation or inhibition of ionospheric irregularities during space weather events (Sahai et al. 2009; Horvath and Lovell 2015).

When the magnitude of TEC deviation is significant, the ionosphere's response to a geomagnetic storm is deemed considerable. Previously, ionospheric storms over the mid-latitude region were defined as those with a percentage TEC deviation of 40% or above (Matamba et al., 2015). The ionosphere over the low-latitude region is more turbulent than that over the mid-latitude region (Molchanov, 2004; Hobara et al., 2005; Amabayo et al., 2014), hence a percentage TEC deviation of ± 45% was selected (Dugassa et al., 2020).

To determine ionospheric storm effects, our study employed the monthly median TEC values for the month in which the storm occurred as background data. Thus, ionospheric storm effects were analyzed using the equation:

$$\Delta TEC = \frac{TEC - TEC_m}{TEC_m} \times 100\%, \qquad 2.17$$

where ΔTEC is the percentage TEC deviation, and TEC_m is monthly median TEC value at a particular epoch.

Figure 2.11 depicts ionospheric storm effect from July 14 to 19, 2012. a) shows TEC variation over Gorahi, GRHI station, (27.95°N, 82.49°E), India, the red plot represent the monthly median while the black plot represent Storm time TEC. b) shows the TEC deviation in percentages. The dotted red line depicts the threshold value of ΔTEC which is ±45%. c) illustrates Dst Index in nT. During the recovery of the geomagnetic storm, on July 16, 2012, a decrease in TEC compared to monthly medians occurred. The ΔTEC indicated a considerable decrease of approximately 50%. On July 16, 2012, ΔTEC was negative between 0600 and 1200 UT (Kuai, 2017). The combined effects of neutral composition disturbances and electric fields on July 16 are responsible for the significant negative storm effects (Liu et al., 2014).

2.6.4 Positive effects of geomagnetic storm on the ionosphere

According to Obayashi and Matuura (1972), neutral composition changes can also lead to positive ionospheric storms. There is no evidence to support this notion in highly disturbed situations (Burns et al., 2007; Prölss, 1995; Mendillo, 2006; Prölss, 2008). Observations strongly support the theory that positive ionospheric storms are induced by ionization transport (Prölss, 1995; Danilov, 2013; Suvorova et al., 2014; Chen et al., 2014). High latitude heat input leads to increased meridional pressure gradient and improved global wind circulation. Winds move ions up field lines into slower recombination zones, increasing electron concentration (Fuller-Rowell et al., 1994; Mendillo, 2006; Prölss, 2008). Near high latitudes, wind circulation drives molecular-species-rich air higher, increasing the density of molecular species compared to atomic species. This increases the ratio of recombination to production near the F_2 peak (Burns et al., 2007). The observed positive storm phase at middle latitudes was mostly attributed to the stronger eastward electric field. The electric field elevates the F_2-region plasma, leading to increased electron density.

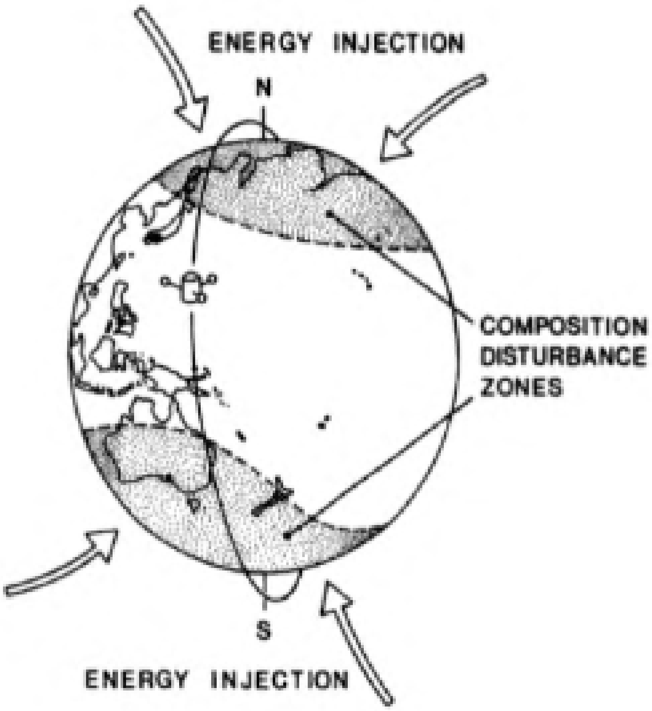

Figure 2.12: The polar energy deposition and the composition disturbance zones (Prölss, 1995).

During storms or substorms, an enhanced convective electric field transports nightside plasmaspheric plasma from higher to lower L-shells with smaller volumes, resulting in increased plasma pressure in the magnetic flux tube and downward plasma flux. These fluxes contribute to higher electron density in the F_2 area. Energy injections, as depicted in Figure 2.12, elevate the F_2-region and contribute to the rise in density in polar latitudes (Prolss, 1995; Tsagouri et al., 2000; Horvath, 2007; Horvath and Lovell, 2015). The [O]/[N2] increases with height, and the increase in this ratio indicates an increase in electron density (Yu et al., 2020). According to Mikhailov et al. (1995), traveling atmospheric disturbances (TADs) can elevate the F_2-region, resulting in favorable positive storm effects. Elevating the F_2-region of the ionosphere reduces recombination rates, resulting in increased plasma density.

Figure 2.11 depicts the positive ionospheric storm effect from July 14 to 16, 2012 over Gorahi, GRHI station, (27.95°N, 82.49°E), India. During the main of the geomagnetic storm, on July 15, 2012, an increase in TEC compared to monthly medians occurred. The ΔTEC indicated a considerable increase of around 50%. On July 14, 2012, positive storm effect was observed between 1600 UT on 14 July and 0500 UT on 16 July (Kuai, 2017). Liu et al. (2014) also examined the combined effects of the multiple electric fields on July 15 and on July 16 in the American sector. The nighttime EIA intensification (positive storm effect) on July 16 in the American sector was attributed to the nighttime eastward electric field, which may have elevated the F_2 region to higher altitudes. Kuai et al. (2015) observed a nighttime long-duration positive storm induced by an eastward electric field over Jicamarca, an American equatorial station.

2.7 Conclusions

This chapter covered the Earth's atmosphere and ionosphere with a focus on TEC and its behaviour during geomagnetic storms. The mechanisms that cause ionospheric responses during storms were also briefly reviewed. The next chapter presents the formation mechanism and characteristics of AGWs and TIDs. The chapter also briefly touches on Medium and Large Scale TIDs.

Chapter 3: Atmospheric Gravity Waves and Travelling Ionospheric Disturbances

This chapter explains how atmospheric conditions affect the propagation of gravity waves. The dispersion relations of gravity wave distinguishes atmospheric waves from acoustic waves. Atmospheric gravity waves may originate from many sources and propagate in different ways. The manifestation of travelling ionospheric disturbance (TIDs) by atmospheric gravity waves are discussed.

3.1 Atmospheric Hydrostatic Equilibrium

According to Holton et al. (2003) and Rauber and Ramamurthy (2015), atmospheric gravity waves are buoyancy oscillations in a stably stratified fluid that are restored by gravity. The restoring force moves the packet back to its neutral position, however it may overshoot due to inertia. If viscous forces are weak enough, the system will oscillate around its neutral state. Due to local displacement of the fluid, oscillations are caused and spread throughout the region as transverse waves known as atmospheric gravity waves (Hines, 1960; Beer, 1974; Hunsucker, 1982; Nappo, 2013). AGWs are oscillations that generate disturbances in the atmosphere. Hydrostatic equilibrium is the balance of upward pressure and downward gravity in a fluid. The word hydrostatic is used to describe a fixed (static) equilibrium in a fluid (hydro) between pressure pushing up and gravity pulling down.

When the assumption that the Earth's atmosphere is an isothermal ideal gas, then the equation of state is given by

$$p = \rho R T, \qquad 3.1$$

With p being the pressure, ρ is density, $R = 287\ J\ kg^{-1}\ K^{-1}$ is the universal gas constant and T is the average temperature (Nappo, 2002).

When there is no vertical motion, the atmosphere can be estimated to be in hydrostatic equilibrium. This explains that an upward pressure acting on an air parcel of density ρ, with a unit area ($dxdy = 1$) at height dz is in balance with the weight of the air parcel

$$dp = -\rho g dz, \tag{3.2}$$

$g \;=\; 9.8\ m/s^2$ is the Earth's acceleration due to gravity.

$$d(\rho RT) = -\rho g dz, \tag{3.3}$$

RT is a constant.

$$RT d\rho = \; -\rho g dz, \tag{3.4}$$

We reduce the equation 3.4 to:

$$\frac{d\rho}{\rho} = -\frac{g}{RT} dz, \tag{3.5}$$

Integrating the above equation

$$\frac{1}{\rho}\ d\rho = -\frac{g}{RT} dz, \tag{3.6}$$

From the integration, we obtain the following

$$\ln ln\ \rho \quad - \ln ln\ \rho_0 \;=\; \ln ln\ \frac{\rho}{\rho_0} \quad = -\frac{g}{RT} z, \tag{3.7}$$

which is equivalent to

$$\rho = \; \rho_0 e^{-\frac{g}{RT} z}, \tag{3.8}$$

Given that H is a scale height for the atmosphere, which is given as:

$$H = \frac{RT}{g}, \tag{3.9}$$

Thus, the density is given by:

$$\rho = \; \rho_0 e^{-\frac{z}{H}}, \tag{3.10}$$

Equation 3.10 suggests that the density of a stable atmosphere decreases with altitude.

3.2 Isothermal Buoyancy Angular Frequency

An air parcel can be displaced vertically in a stratified atmosphere which is stable, causing the generation of gravity waves due to the Buoyancy force, which acts to restore the equilibrium (Nappo, 2002; Schunk and Nagy, 2009). The air parcel oscillates at its equilibrium position at the Brunt-Väisälä frequency due to the restoring force. An air parcel displaced from its equilibrium position (s_e) with a distance δs and an angle of α from the vertical, the Buoyancy force acting on the displaced air parcel is given as follows:

$$m_p \frac{d^2(\delta s)}{dt^2} = -g \ \sin \ \alpha \ (m_p - m_a)\,, \qquad 3.11$$

where $g\ sin\ \alpha$, m_p, m_a is the gravity component along the displacement direction, mass of an air parcel in equilibrium with its environment at height $\mathrm{s_e}$ and the mass of the displaced air in the parcel respectively (Nappo, 2002). Using the ideal gas law and rewriting the mass of the air parcel using ρ and volume (V), equation 3.11 can be reduce to (Nappo, 2002):

$$\rho_p V_p \frac{d^2(\delta s)}{dt^2} = -g \ \sin \ \alpha \ \ (\rho_p V_p - \ \rho_a V_a)\,, \qquad 3.12$$

Assuming that the air pressure of the air parcel is equal to that of the environment and that the volume stays the same, the equation is now simplified to:

$$\frac{d^2(\delta s)}{dt^2} = -g \ \sin \ \alpha \ \frac{(T_p - \ T_a)}{T_p}, \qquad 3.13$$

where T_a and T_p are the environmental and parcel temperatures, respectively. The Taylor series expansion of T_a and T_p to the first degree substituted in Equation 3.13 leads to:

$$\frac{d^2(\delta s)}{dt^2} = \frac{-g \ \sin \ \alpha}{T_a} \left(\frac{\partial T_a}{\partial s} - \ \frac{\partial T_p}{\partial s} \right) \delta s, \qquad 3.14$$

By applying the adiabatic lapse rate, $\Gamma = \ \frac{\partial T_p}{\partial s} = \frac{g \ \sin \ \alpha}{C_p}$, where C_p is the specific heat capacity at constant pressure, the expression can be written as follows:

$$\frac{d^2(\delta s)}{dt^2} = \ \frac{-g \ \sin \ \alpha}{T_a} \left(\frac{\partial T_a}{\partial s} - \frac{g \ \sin \ \alpha}{C_p} \right) \delta s, \qquad 3.15$$

Equation 3.15 can be rewritten using the potential temperature $\theta = \ T_a(1000/p)^{\frac{R}{C_p}}$, which is the temperature of an air parcel that is moved adiabatically from an altitude with pressure to the ground where the pressure is 1000 mb (Nappo, 2002):

$$\frac{d^2(\delta s)}{dt^2} = \ \frac{-g}{\theta} \ \frac{\partial \theta}{\partial s} \ \sin^2 \alpha \delta s, \qquad 3.16$$

Then the motion of the parcel along the displacement direction is expressed by:

$$\delta s(t) = A e^{-i\omega_b t} + B e^{-i\omega_b t}, \qquad 3.17$$

where $\omega_b^2 = \ \frac{g\ \partial\theta}{\theta \partial s} \sin^2 \alpha$ is the Brunt-Väisälä frequency, or it can be rewritten by using the frequency for purely vertical displacement (i.e. $\omega_v^2 = \ \frac{g\partial\theta}{\theta\partial s}$)

$$\omega_b = \ \omega_v \sin sin \ \alpha \ , \qquad 3.18$$

Therefore, for $\alpha \ = \ 0°$ then $\omega_b \ = \ 0$ and the motion is horizontal with no oscillation, and if $\alpha \ = \ 90°$, which means a vertical displacement, then $\omega_b = \ \omega_v$.

3.3 Dispersion relation equation for gravity waves

Gravity waves propagate in the atmosphere by the interaction between the pressure gradient (∇p), the buoyancy force (ρg) and the inertia force (Hocke and Schlegel, 1996). Linear theory is used to explain and formulate the dispersion relation equation for gravity waves. When deriving the dispersion relation the Coriolis force and centripetal acceleration are ignored because gravity wave periods which are between 10 min and 3 hrs are much less than planetary rotation periods, 24 hrs (Schunk and Nagy, 2009). The atmosphere is then assumed to be isothermal, compressible and inviscid to rule out the source and dissipation mechanisms (Hines, 1960; Schunk and Nagy, 2009). Additionally, the continuity, momentum and energy equations for a single-component neutral gas are given by the following equations respectively (Schunk and Nagy, 2009):

$$\frac{\partial \rho}{\partial t} + \nabla \bullet (\rho u) = 0, \qquad 3.19$$

$$\rho \left(\frac{\partial}{\partial t} + u \bullet \nabla \right) u + \nabla p - \rho G = 0, \qquad 3.20$$

$$\left(\frac{\partial}{\partial t} + u \bullet \nabla \right) p + \gamma p (\nabla \bullet u) = 0, \qquad 3.21$$

where u, G, $\gamma = 5/3$ is atmospheric velocity, gravitational acceleration and the ratio of specific heat respectively. Utilisation of linearisation theory to expand the atmospheric variables to a background and perturbed state $\rho = \rho_0 + \rho_1$, $p = p_0 + p_1$ and $u = u_1$. 0 and 1 subscripts denote the unperturbed (or initial) and perturbed states of the atmosphere, respectively (Schunk and Nagy, 2009). p_0 and ρ_0 in terms of the scale height are as follows p_0, $\rho_0 \; \alpha \; e^{-\frac{z}{H_0}}$ where $H_0 = kT_0/mg$ and k is the Boltzmann constant, 1.381 × 10^{-23}J/K, which shows that the initial atmospheric state varies with z exponentially. Substituting the above expressions for the terms containing $\nabla \rho_0$ and ∇p_0 results in $u_1 \cdot \nabla \rho_0 = -\rho_0 \, H_0 \, u_{1z}$ and $u_1 \cdot \nabla p_0 = -p_0 \, H_0 \, u_{1z}$. The equations of continuity, momentum and energy respectfully simplifies to the given equations,

$$\frac{\partial}{\partial t} \left(\frac{\rho_1}{\rho_0} \right) - \frac{1}{H_0} u_{1z} + (\nabla \bullet u_1) = 0, \qquad 3.22$$

$$\frac{\partial u_1}{\partial t} + \frac{p_1}{\rho_0 p_0} \nabla p_0 + \frac{p_0}{\rho_0} \nabla \frac{p_1}{p_0} - \frac{\rho_1}{\rho_0} G = 0, \qquad 3.23$$

$$\frac{\partial}{\partial t} \left(\frac{p_1}{p_0} \right) - \frac{1}{H_0} u_{1z} + \gamma \, (\nabla \bullet u_1) = 0, \qquad 3.24$$

u_{1z} is the vertical component of the perturbed velocity. Perturbations in density, pressure and velocity are represented by plane wave equation (Schunk and Nagy, 2009) as given here,

$$\frac{\rho_1}{\rho_0},\ \frac{p_1}{p_0},\ u_1\ \propto\ e^{i(K\bullet r-\omega t)}, \qquad 3.25$$

with K being the wave vector and ω is the wave frequency. The assumption that the gravity wave propagates in x-z plane ($K\ =\ (K_x,\ K_z)$) is made, thus the momentum equation becomes two equations with the velocity in x and z components ($u\ =\ (u_x,\ u_z)$). This results in four equations with four unknowns (Schunk and Nagy, 2009):

$$-i\omega\left(\frac{\rho_1}{\rho_0}\right)+iK_xu_{1x}+\left(iK_z-\frac{1}{H_0}\right)u_{1z}=0, \qquad 3.26$$

$$\frac{ik_xc_0^2}{\gamma}\frac{p_1}{p_0}-i\omega u_{1x}=0, \qquad 3.27$$

$$\left(iK_z-\frac{1}{H_0}\right)\frac{c_0^2}{\gamma}\frac{p_1}{p_0}-i\omega u_{1z}+g,\left(\frac{\rho_1}{\rho_0}\right)=0, \qquad 3.28$$

$$-i\omega\left(\frac{p_1}{p_0}\right)+i\gamma K_xu_x+\left(i\gamma K_z-\frac{1}{H_0}\right)u_z=0, \qquad 3.29$$

c_0, K_x, K_z is the speed of sound in the neutral gas, the horizontal and vertical wave numbers, respectively. The dispersion relation for internal gravity waves is expressed by (Hines, 1960; Schunk and Nagy, 2009):

$$\omega^4-\omega c_0^2\left(K_x^2+K_z^2\right)+(\gamma-1)g^2K_x^2-i\gamma g\omega^2K_z^2=0, \qquad 3.30$$

Equation 3.30 can be solved by ignoring gravity ($g\ =\ 0$) which gives the dispersion relation of sound waves. In the case of sound waves both K and ω are real and the wave propagates without growth or attenuation ($\omega\ ^2\ =\ c_0^2K^2$) (Hines, 1960; Schunk and Nagy, 2009). There will be no solution where both K_x and K_y are purely real and different from zero, if gravity is not set to zero in Equation 3.30. This is the case for gravity waves, where waves experience attenuation as they propagate. Therefore, one of the wave vector components has to be complex ($K_z\ =\ K_{zr}\ +\ iK_{zi}$), where K_{zr} is the real part and K_{zi} is the imaginary part. Equation 2.30 then becomes

$$\omega^4-\omega c_0^2\left(K_x^2+K_{zr}^2+K_{zi}^2\right)+(\gamma-1)g^2K_x^2+\gamma gK_{zi}^2\omega^2-\\ i\omega^2K_{zr}^2\left(\gamma g+2c_0^2K_zi\right)=0, \qquad 3.31$$

where the imaginary part of the equation becomes

$$K_{zi}=\ -\frac{\gamma g}{2c_0^2}=-\frac{1}{2H_0}, \qquad 3.32$$

and the velocity perturbation equation ($u_1\ \propto\ e^{i(K\bullet r-\omega t)}$) becomes

$$u_1 \propto \ e^{\frac{z}{2H_0}} e^{i(K_x x + K_{zr} z - wt)}, \qquad 3.33$$

Gravity waves are characterized by constant wave perturbation energy ($\frac{1}{2}\rho_0 u\,_{1z}^{\,2}$) because $\rho_0 \ \propto \ e^{-\frac{z\gamma g}{c_0^2}}$ and $u_{1z} \ \propto \ e^{-\frac{z\gamma g}{2c_0^2}}$ (Schunk and Nagy, 2009). The amplitude of the wave increases exponentially as the wave propagates towards higher altitudes where the density decreases ($e^{\frac{z\gamma g}{2c_0^2}}$) (Hines, 1960; Nappo, 2002; Schunk and Nagy, 2009).

3.4 Ionospheric Response to Gravity Waves

Understanding the ionosphere's variations relies on the continuity equation of electron density. It depicts the rate of change in electron density at each altitude as

$$\frac{dN_e}{dt} = \ P_e - L_e - \nabla \bullet (N_e V_e)\,, \qquad 3.34$$

According to Hooke (1970), Beer (1974) and Kelley (2009) electron density (N_e), velocity (V_e), and production and loss rates (P_e and L_e) all play a role in this equation. Gravity waves disrupt electron density, resulting in two parts: background (N_{e0}) and disturbed ($N_e^{'}$) (Hooke, 1970).

The electron density is given as:

$$N_e = N_{e0} + N_e^{'}, \qquad 3.35$$

Similarly, the electron velocity is expressed as

$$V_e = V_{e0} + V_e^{'}, \qquad 3.36$$

Assuming minimal production and loss coefficient perturbations and a windless background ionosphere, the perturbations are as follows.

$$\frac{dN_{e1}}{dt} = -\nabla \bullet \left(N_e V_e^{'}\right), \qquad 3.37$$

The AGW-induced velocity ($V_e^{'}$) is linked to the perturbation velocity of neutral gas (U_n) by balancing Lorentz force and ion drag (Beer, 1974; Kelley, 2009):

$$M_e V_d \left(V_e^{'} - U_n\right) + e^{-} \left(V_e^{'} \times B\right) = 0, \qquad 3.38$$

where B is the geomagnetic field, M_e is the electron mass, and V_d is the electron-neutral collision frequency. Macleod (1966) described the solution as

$$V_e^{'} = \frac{1}{1+r^2}\left[r^2 U_n + r\,(U_n \times b) + (U_n \times b)\,b\right], \qquad 3.39$$

where r is the ratio of ion-neutral frequency to electron gyro-frequency, and b is a unit vector pointing in the direction of the geomagnetic field. According to Macleod (1966), at altitudes beyond 170 km, $r << 1$. This leads to

$$V_e' = (U_n \times b)\, b, \qquad 3.40$$

Assume the perturbed electron density has the following form:

$$N_{e1} \propto \ e^{-i(\omega t + k_x x + k_y y)}, \qquad 3.41$$

Hooke (1970) defined perturbed electron density in equation 3.37 as:

$$N_{e1} = -\tfrac{1}{i\omega} \nabla \bullet \left[N_{e0} \left(U_n \bullet b \right) b \right] \qquad 3.42$$

The equation indicates that the electron density fluctuations induced by AGWs propagate in the atmosphere. These are known as traveling ionospheric disturbances in the ionosphere (Hines, 1960; Hooke, 1970; Hocke and Schlegel, 1996).

3.5 Propagation of AGWs

AGWs exist at different altitudes, from tropospheric altitudes to thermospheric altitudes. Thermospheric gravity waves have a larger vertical wavelength than mesospheric gravity waves (Francis, 1974; Bristow et al., 1996; Bristow and Greenwald, 1997). Gravity waves in the atmosphere move with oscillations that are perpendicular to the direction of the energy transfer, i.e. they are transverse waves (Hunsucker and Hargreaves, 2003). As waves propagate from a high density region, i.e. the lower atmosphere, to a less dense region their amplitudes increase and demonstrate instability (Vadas and Fritts, 2006). Figure 3.1 illustrates the four mechanisms of AGW propagation in the atmosphere (Mayr et al., 1991, 2013). Mode (1) is a direct gravity wave that propagates horizontally in the thermosphere. These waves travel far from the source at fast speeds and have a long wavelength. According to Mayr et al. (1991, 2013) and Hocke and Schlegel (1996), these waves spread equatorward from high to mid latitudes. The second upper gravity wave mode (2) travels diagonally from the thermosphere. Mode 2 waves have shorter vertical wavelengths than mode 1 and attenuate in the upper atmosphere due to high viscosity and thermal conduction (Hines, 1960; Mayr et al., 1991; Hocke and Schlegel, 1996; Kelley, 2009).

AGW modes 3 and 4 propagate slower than sound in the lower atmosphere. Modes 3 and 4 correlate to medium- and large-scale TID observations in the ionosphere, respectively (Hocke and Schlegel, 1996; Mayr et al., 2013). The low viscosity and thermal conduction of the lower atmosphere allow this wave to travel large distances. Mode 4 refers to a wave that bounces off the Earth's surface and travels into the thermosphere (Mayr et al., 1991, 2013; Hocke and Schlegel, 1996).

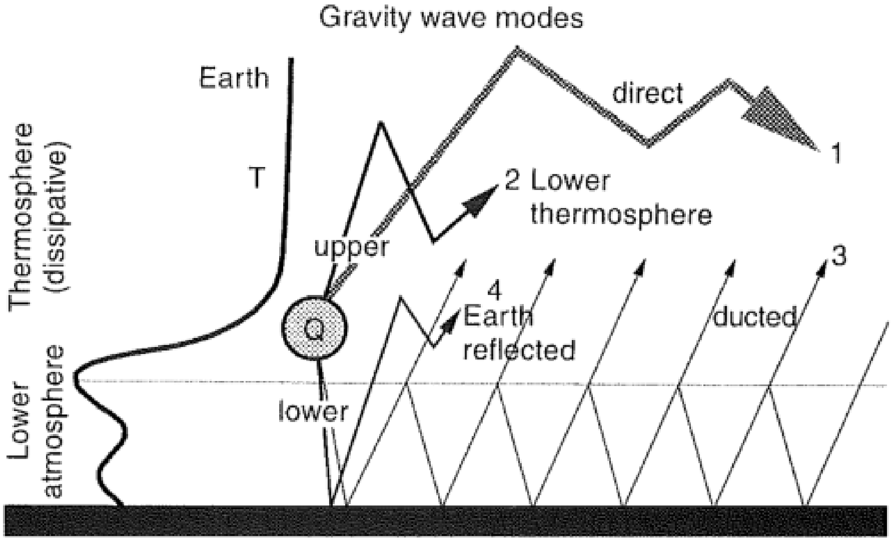

Figure 3.1: Schematic representation of the four modes of AGW propagation in the lower and upper atmosphere (Mayr et al., 1991)

3.6 Sources of AGWs

AGWs in the thermosphere and ionosphere can be caused by a variety of factors, including geomagnetic storms, auroral activity, wind shear, large-scale convective systems, solar eclipses, meteorological processes in the lower atmosphere, and man-made nuclear explosions (Hines, 1967; Hunsucker, 1982; Mayr et al., 1984; Hajkowicz and Hunsucker, 1987; Vadas, 2007; Afraimovich et al., 2008, 2009a; Vadas and Becker, 2018). The solar terminator marks the transition between day and night. Solar radiation causes rapid variations in energy intake, resulting in a sharp gradient in Earth's atmosphere and ionosphere properties like density, temperature, and pressure (Somsikov and Ganguly, 1995).

A sharp gradient causes instability and fluctuations in ionospheric plasma (Hines, 1960; Francis, 1974; Somsikov and Ganguly, 1995). According to Somsikov and Trotskii (1975), AGWs migrate in the same direction as the solar terminator due to gravity's response to perturbations. Moving solar terminators are a unique source of gravity waves due to their predictable behavior. Afraimovich et al. (2009a) suggest that if the solar terminator is a consistent source of AGWs, the reaction of the medium to this input can provide insights into atmospheric conditions. Afraimovich et al. (2003, 2009a,b) discovered that the solar terminator transit causes certain medium-scale ionospheric perturbations.

This is the wave packet that appears as a narrowband oscillation of the TEC. MacDougall et al. (2009) identified solar terminators as a cause of several observed TIDs. Recent research has linked TIDs to the solar terminator (Somsikov and Trotskii, 1975; Somsikov and Ganguly, 1995; Afraimovich et al., 2003; Hernandez-Pajares et al., 2006; Afraimovich et al., 2009a,b; MacDougall et al., 2009; Somsikov, 2011). Natural geological disasters like earthquakes, tsunamis, and volcanic eruptions can also contribute to AGWs (Hocke and Schlegel, 1996; Boška and Saulî, 2001; Ibrahim et al., 2010; Chen et al., 2017; Savastano et al., 2017; Bravo et al., 2022; Themens et al., 2022, and references therein). According to Beer (1974), Charron and Brunet (1999), and Nappo (2013), as air travels over a mountain, it creates a pressure gradient that requires momentum and energy exchange between the fluid and the earth. The pressure is often higher on the upwind side of the mountain and lower on the downwind. According to Charron and Brunet (1999), air exerts a net force on the ground, while drag is perceived within the flow. Rising surface winds create quasi-stationary waves that travel to the higher atmosphere (Nappo, 2013; Heale et al., 2020). A mountain wave (MW) is unusual in that it can only occur with the mean background wind. When the wind speed reaches zero, the layer works as a critical level that filters the wave into the mean flow (Booker and Bretherton, 1967; Heale et al., 2020). As the MW approaches the critical level, it separates into minor vertical scales. A short vertical scale leads to a significant vertical gradient in the wind and temperature structure of a wave, potentially breaking a MW. Breaking waves result in secondary atmospheric gravity waves (Bacmeister and Schoeberl, 1989; Satomura and Sato, 1999; Vadas and Becker, 2018, 2019; Heale et al., 2020).

Studies indicate that energy fluctuations in the auroral region caused by geomagnetic storms significantly impact the thermospheric composition by generating atmospheric gravity waves (Hunsucker, 1982; Hocke and Schlegel, 1996; Balthazor and Moffett, 1997). Equatorward AGWs are caused by momentum transfer via the Lorentz force and heating, as well as particle deposition by Joule heat (Hajkowicz and Hunsucker, 1987; Hocke and Schlegel, 1996; Balthazor and Moffett, 1997; Afraimovich et al., 2008; Habarulema et al., 2016). Chimonas (1970) investigated the equatorial electrojet as a potential source of gravity waves in disturbed conditions. He found that the equatorial electrojet can augment the Lorentz force, resulting in higher coupling between neutral particles and ions in the equatorial area. Ions transfer energy to neutral particles, creating gravity waves that propagate poleward. According to Knudsen (1969) and Chimonas (1969, 1970), the equatorial electrojet coupling produces less gravity waves that cause ionosphere disturbances than the auroral electrojet.

3.7 Traveling Ionospheric Disturbances

TIDs disperse energy and momentum via molecular viscosity, thermal conductivity, and ion drag (Ding et al., 2008). The study of wave motions in the high atmosphere and their manifestation in the ionosphere began in the 1940s (Waldock and Jones, 1986; Nappo, 2002). Hines (1960) conducted the first study linking AGW to TIDs, describing ionospheric abnormalities in terms of internal gravity waves. Since then, TIDs have been intensively researched theoretically using models and data. Review publications (Francis, 1975; Hunsucker, 1982; Hocke and Schlegel, 1996; Nishitani et al., 2019) provide further information and highlights. Studies reveal that TIDs have diverse properties and thus are usually classified into large-scale TIDs and medium-scale TIDs, based on their wave velocity and periods (e.g. Hunsucker, 1982; MacDougall et al., 2009).

3.7.1 Large-scale TIDs

Large-scale TIDs (LSTIDs) are defined as TIDs with horizontal velocities between 250 and 1000 ms^{-1}, wave periods between 0.5 and 3 hours, and a horizontal wavelength of more than 1000 km (Ogawa et al., 1987; Samson et al., 1989; Hocke and Schlegel, 1996). LSTIDs travel at a comparable speed to speed of sound in the thermosphere (Hocke and Schlegel, 1996). LSTIDs are capable of traveling large distances due to their high speed and long horizontal wavelengths. LS TIDs in the equatorward direction are linked to auroral area joule heating, particle precipitation, and Lorentz-coupling processes during geomagnetically disturbed conditions (Hunsucker, 1982; Hocke and Schlegel, 1996; Balthazor and Moffett, 1997; Bruinsma and Forbes, 2008). A geomagnetic storm injects energy into the thermospheric-ionospheric system at high latitudes, leading to increased winds, changes in neutral composition, and amplification of equatorward LSTIDs (Hunsucker, 1982; Richmond et al., 1992; Fuller-Rowell et al., 1994; Hocke and Schlegel, 1996; Balthazor and Moffett, 1997; Habarulema et al., 2022). Ding et al. (2013) and Habarulema et al. (2015, 2016) observed poleward LSTIDs of equatorial origin during disturbed conditions. Habarulema et al. (2015, 2016) found that poleward LSTIDs may occur due to enhanced equatorial electrojet (EEJ) during local daytime. Other poleward LSTIDs exist that propagate across narrower latitudinal regions and are unrelated to any geomagnetic activity (Ding et al., 2013). According to Vadas and Liu (2009), they might be caused by large AGWs that radiate at a speed of 480 to 510 m/s. These AGWs form as secondary waves when smaller ones dissipate in the thermosphere.

3.7.2 Medium-scale TIDs

According to several studies (Mayr et al., 1984; Hocke and Schlegel, 1996; Kotake et al., 2007; Katamzi-Joseph et al., 2019; Vadas and Becker, 2019), medium scale TIDs (MSTIDs) have wavelengths of roughly 100–1000 km, periods of 15–60 minutes, and horizontal propagation velocities of 100–250 m/s. Over the years, MSTIDs were observed by Incoherent scatter radar (Nicolls and Heinselman, 2007; Nishioka et al., 2009; Panasenko et al., 2019), ionosonde (Bowman, 1990; Kozlovsky et al., 2013), HF Doppler (Waldock and Jones, 1986; Grocott et al., 2013), airglow imager (Otsuka et al., 2004; Shiokawa et al., 2009; Vadas et al., 2009; Fukushima et al., 2012), and the total electron content approach (Afraimovich et al., 2003, 2009a; Kotake et al., 2007). These authors reported MSTIDs that occurred both during the day and at night. MSTIDs appear more frequently. MSTIDs are more common during winter days and summer nights (Kotake et al., 2007; Shiokawa et al., 2009; Ding et al., 2014; Oinats et al., 2015). According to Fukushima et al. (2012), the frequency of MSTIDs at night decreases as solar activity decreases. MSTIDs can spread in any direction, depending on the sources, troposphere and the season. Chum et al. (2012) discovered that MSTIDs propagate equatorward in the winter and poleward in the summer. During summer, nocturnal MSTIDs propagate southwest in the northern hemisphere and northeast in the southern hemisphere (Pimenta et al., 2008; Otsuka et al., 2013).

MSTIDs can be caused by natural processes such as geomagnetic storms, auroral phenomena, tsunamis, tropospheric turbulence and jet currents, severe earthquakes, volcanic eruptions, the solar terminator, vortices, cold fronts, deep convective plume, and artificial nuclear explosions (Hines, 1960; Richmond, 1978; Hunsucker, 1982; Hocke and Schlegel, 1996; Wan et al., 1998; Boška and Saulî, 2001; Afraimovich et al., 2003,2009b, references therein). MSTIDs are more vulnerable to neutral winds compared to LSTIDs with longer periods and faster propagation velocities. Chum et al. (2012) reported that MSTIDs have higher speeds in winter than in summer. Fukushima et al. (2012) found that decreasing solar activity led to an increase in the average horizontal wavelength of nocturnal MSTIDs.

Sindelarova et al. (2012) found that MSTIDs (those lasting less than 30 minutes) are independent of geomagnetic activity. During moderate magnetic storms, MSTIDs lasting 30-50 minutes are more common, according to the study. Ding et al. (2014) conducted a comprehensive study in China and discovered that the number of MSTIDs increases with geomagnetic activity and their preferred orientation is equatorward.

3.8 Conclusion

The formation mechanism and characteristics of AGWs and TIDs at different regions are discussed. Discussion on ionospheric response and dispersion relation was given. The chapter also briefly explains how TIDs dissipate energy. Lastly, a short introduction on classes of TIDs is given.

Chapter 4: Data Sources and Methodology

This chapter outlines the data sources and research methods used for this thesis. A basic introduction to GPS and its segments is provided, as well as an explanation of how TEC is calculated from GPS measurements. It also gives the methodology used to estimate the characteristics of TID activity.

4.1 GPS Overview

A GPS satellite is a spacecraft that orbits the Earth at a 55-degree inclination (Misra and Enge, 2006). Satellites are instruments that are deliberately deployed in space to orbit the Earth or another large object in the solar system. They can be placed in space for a variety of reasons, including the fact that satellites are the fastest devices capable of providing accurate information anywhere on the planet 24 hours a day.

GPS was developed by the US Department of Defence (DoD) (Hofmann-Wellenhof et al., 1992). It is the most prominent satellite constellation in the global navigation satellite system (GNSS). Other satellite systems related with GNSS include BeiDou, Galileo, GLONASS, Navigation Indian Constellation, and Quasi-Zenith (gps.gov, 2017c). GNSS aims to estimate factors such as position, velocity, and time (Misra and Enge, 2006). GPS relies on radio waves from satellites orbiting the Earth at around 20,000 km altitude (Hofmann-Wellenhof et al., 1992). The DoD offers two GPS access methods: SPS (standard positioning service) and PPS (precision positioning service). The SPS is open to civilian users, while the PPS is only accessible to approved DoD users (Misra and Enge, 2006). It employs the precision code (P-code), which is one of the transmitted GPS codes. The PPS has an estimated location accuracy of 16 m horizontally and 23 m vertically (95% confidence level) (Farrell and Barth, 1999; El-Rabbany, 2002). SPS performs less accurately than PPS. SPS is a coarse acquisition (C/A) code-only location and timing service that is freely provided to all GPS users worldwide. This level of service is delivered via the L1 frequency, which comprises C/A codes and navigation data messages (Farrell and Barth, 1999). Initially, SPS had a positioning accuracy of 100 m for horizontal components and 156 m for vertical components (95% confidence level) (El-Rabbany, 2002; Mosavi, 2013).

According to Hofmann Wellenhof et al. (1992), GPS operates in three segments namely space, control, and user segments.

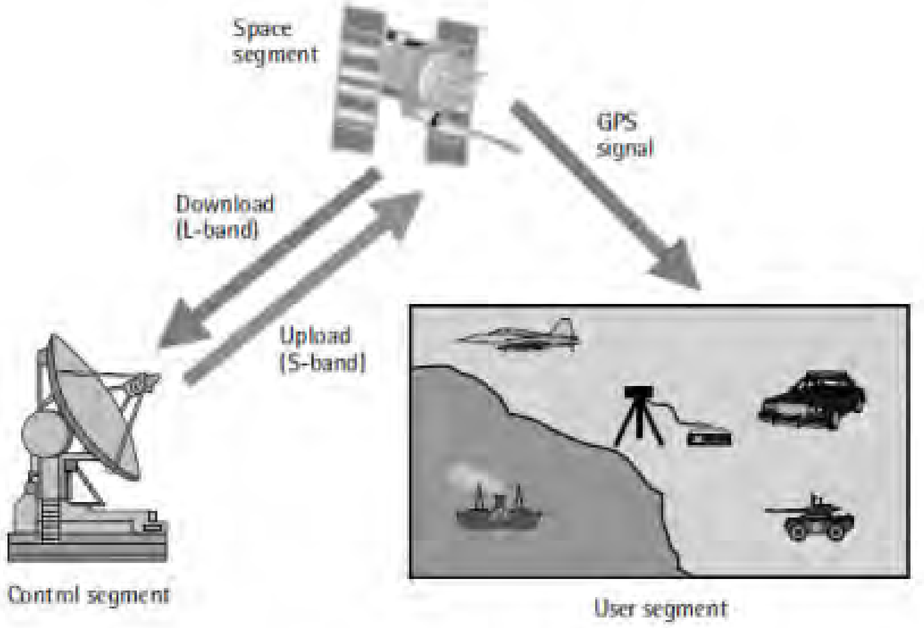

Figure 4.1: Overview of the GPS segment, space segment and user segment (El-Rabany, 2002).

4.1.1 Space segment

The space segment includes at least 24 satellites (Kumar and Moore, 2002; Misra and Enge, 2006). GPS satellites transmit a signal that includes two sine waves, digital codes, and navigation message components (El-Rabany, 2002; Kumar and Moore, 2002). The carrier receives code and navigation signals via binary two-phase modulation. Carriers and codes indicate the distance between a user's receiver and GPS satellites. Navigation messages often comprise satellite coordinates and time-based information. Satellites use a high-precision atomic clock to govern transmitted signals (Hofmann-Wellenhof et al., 1992; Ferguson, 1997; El-Rabbany, 2002). Satellites send communications at three frequencies: L1 (1575.42 MHz), L2 (1227.60 MHz), and L5 (1176.45 MHz). These frequencies are calculated by multiplying the fundamental L-band frequency of 10.23 MHz by 154, 120, and 115 (Misra and Enge, 2006). Each transmission includes a carrier, range code, and navigation data. Misra and Enge (2006) define a carrier as a sinusoidal signal with frequency L1, L2, or L5. The range code, also known as pseudo-random noise (PRN) codes, allows satellites to transmit at the same frequency without interference. PRN codes for SPS are referred to as coarse/acquisition (C/A) codes, whereas those for PPS are referred to as precision (P(Y)) codes (Misra and Enge, 2006). Navigation data includes information on the satellite's position, velocity, health status, and clock bias parameters (Hofmann-Wellenhof et al., 1992;

Misra and Enge, 2006). Satellites include four atomic clocks and broadcast radio signals with transmission times (Ferguson, 1997). Figure 4.2 shows the satellite constellation. Each satellite orbits the Earth twice daily (Hofmann-Wellenhof et al., 1992; El-Rabbany, 2002; Misra and Enge, 2006; Leick et al., 2015).

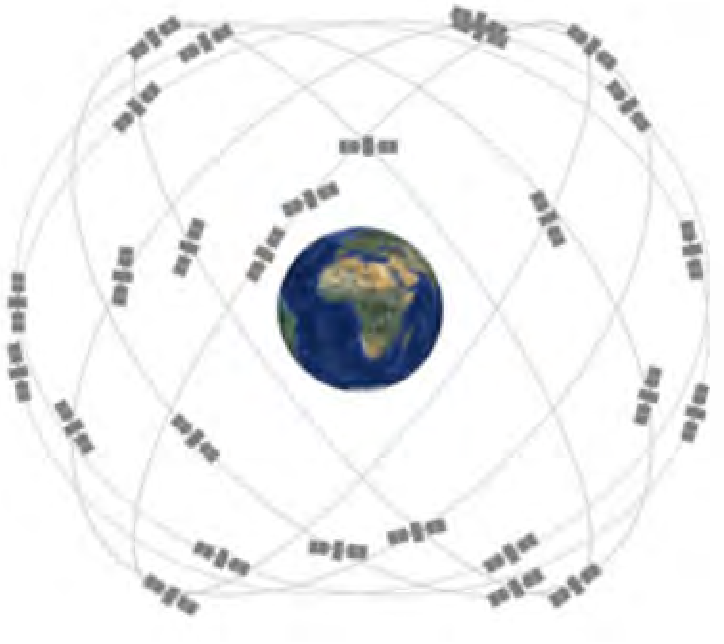

Figure 4.2: GPS constellation (https://www.gps.gov/systems/gps/).

4.1.2 Control Segment

The control segment consists of a global network of ground-based control stations. The Master Control Station is located at the United States Air Force Base in Colorado (Misra and Enge, 2006). The control segment tracks and updates navigation messages for satellites (Ferguson, 1997). Furthermore, it anticipates satellite clock parameters, velocity, and location, as well as maintaining their health (Hofmann-Wellenhof et al., 1992; Misra and Enge, 2006). Figure 4.3 depicts the GPS control segment's position. There is a master control station, an alternative master control station, 11 command and control antennas, and 16 monitoring locations. GPS satellite signals are received through the antenna and decoded by the receiver processor. The receiver processor provides precise location, speed, and time information (Hofmann-Wellenhof et al., 1992; El-Rabbany, 2002; Mulla et al., 2015).

4.1.3 User Segment

The user segment comprises devices capable of receiving GPS signals. These receivers have satellite-synchronized clocks. Each receiver provides a reference signal, similar to the one received from the satellite. The receiver compares the reference signal to the satellite-generated signal to estimate the range between them. This can be done in two ways: multiplying the received signal's transit time by the speed of light or calculating the phase difference between the reference and received signal (Hofmann-Wellenhof et al., 1992). However, because of improper synchronization between receiver and satellite clocks, the range is known as pseudorange (Misra and Enge, 2006).

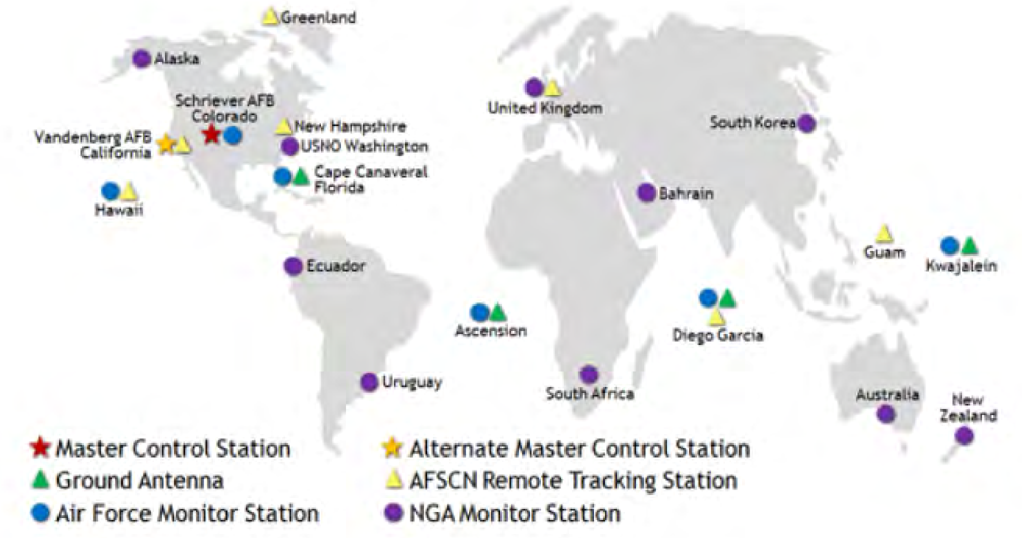

Figure 4.3: Global network of ground facilities that track the GPS satellites (GPS.gov: Control Segment).

4.2 GPS Signal

GPS satellites use atomic clocks made of caesium or rubidium to provide time information for signals they broadcast. Satellite clocks provide internal clock correction (Farrell and Barth, 1999). GPS satellites communicate constantly via two L-band radio frequencies, Link 1 (L1) and Link 2 (L2) (Kumar and Moore, 2002; Misra and Enge, 2006; Mulla et al., 2015; Xu and Xu, 2016). The L band has frequencies ranging from 1 GHz to 2 GHz. The two carrier frequencies are created at $f_1 = 1575.42$ MHz (L1) and $f_2 = 1227.60$ MHz (L2) (Saito et al., 1998; Farrell and Barth, 1999; El-Rabbany, 2002; Mulla et al., 2015). These two frequencies emanate from the fundamental frequency $f_o = 10.23$ MHz:

$$\begin{aligned} f_1 &= 154.f_0 = 1575.42 \text{ MHz}, \\ f_2 &= 120.f_0 = 1227.60 \text{ MHz}, \end{aligned} \qquad 4.1$$

Satellites combine binary phase-shift keying (BPSK) with C/A and P-code PRN codes to modify their L1 signals (El-Rabbany, 2002; Misra and Enge, 2006). The C/A code is modulated only on the L1 carrier. Satellites have unique C/A PRN codes that are approximately orthogonal to one another. The L2 signal of each is solely modified by P-code (Ferguson, 1997; Farrell and Barth, 1999). P-code is a lengthy 10.23 MHz PRN code. Anti-spoofing mode involves encrypting the P-code into the Y-code (Farrell and Barth, 1999; El-Rabbany, 2002). The encrypted Y-code can only be accessed by authorized individuals with the encryption key. According to Farrell and Barth (1999) and Misra and Enge (2006), anti-spoofing modules should be organized by receiver channel. The navigation message is modulated using both L1 and L2 carriers. Navigation messages are 50 bps signals that the GPS receiver decodes to determine satellite orbits, clock corrections, and other system characteristics (Farrell and Barth, 1999).

4.3 Pseudorange Measurement

The pseudorange is an approximation of the distance between a GPS receiver and a GPS satellite. GPS signal transmission time between satellite and receiver antenna is used to calculate distance (Farrell and Barth, 1999; El-Rabbany, 2002; Misra and Enge, 2006). The symbols t_s and t_r in Equation 4.2 represent the states of the satellite clock during transmission and the receiver clock during signal receipt. The clock delay relative to GPS system time is represented by δ_s and δ_r. The discrepancy in clock readings represents the time-shifted Δt, which aligns satellite and reference signals throughout the receiver's code correlation process (Hofmann-Wellenhof et al., 1992). Thus,

$$\begin{aligned}\Delta t = \ & t_r - t_s = [t_r(GPS) - \delta_r] - [t_s(GPS) - \delta_s] = \\ & t_r(GPS) - t_s(GPS) - \delta_r + \delta_s,\end{aligned} \tag{4.2}$$

$\Delta t(GPS) = t_r(GPS) - t_s(GPS)$, while $\Delta\delta = \delta_s - \delta_r$. The satellite clock bias, δ_s, can be represented by a polynomial, with coefficients transmitted in the first subframe of the navigation message. If δ_s corrections are done, $\Delta\delta$ equals the negative receiver clock delay (Hofmann-Wellenhof et al. (1992)). Multiply equation 4.2 by the speed of light ($c = 3 \text{ x } 10^{8}$ m/s) to calculate the pseudorange (R).

$$R = c\Delta t(GPS) + c\Delta\delta, \tag{4.3}$$

The TEC can be calculated using GPS pseudorange measurements. Gao et al. (2002), Choi et al. (2011), Sabzehee et al. (2018) use pseudorange measurements (P_1 and P_2) at L1 and L2 to express

$$P_1 = \rho + c(dt - dT) + d_{orb} + d_{trop} + I_1 + b^s_{p1} - B^r_{p1} + \epsilon\,(P_1)\,, \tag{4.4}$$

$$P_2 = \rho + c(dt - dT) + d_{orb} + d_{trop} + I_2 + b^s_{p2} - B^r_{p2} + \epsilon\,(P_2)\,, \tag{4.5}$$

In Equations 4.4 and 4.5, ρ, c, d_t, d_T, d_{trop} and d_{orb} represents the true geometric range (m) between the receiver and satellite, the speed of light (m/s), the satellite clock error with respect to GPS time (s), the receiver clock error with respect to GPS time (s), the tropospheric error (m), and the orbital error. I_1 and I_2 are the pseudorange ionospheric delays (m) at L1 and L2, respectively. $b^s{}_{p1}$ and $b^s{}_{p2}$ are the pseudorange satellite delays (m) at L1 and L2, respectively. $B^r{}_{p1}$ and $B^r{}_{p2}$

are the pseudorange receiver delays (m) at L1 and L2, respectively. $\epsilon\ (P_1)$ and $\epsilon(P_2)$ are the pseudorange measurements noises, including multipath errors (m). Pseudorange measurements remove geometric range, orbital error, clock errors, and tropospheric delay, resulting in a geometry-free linear combination by ignoring thermal noise and multipath errors and removing them from Equations 4.4 and 4.5, i.e.

$$P_2 - P_1 = I_2 - I_1 + \left(b^s_{p2} - b^s_{p1}\right) + \left(B^r_{p2} - B^r_{p1}\right) = I + b^s_p + B^r_p, \tag{4.6}$$

The equation $b_p = b^s{}_{p2} - b^s{}_{p1}$ represents the differential satellite delay, $B^r{}_p = B^r{}_{p2} - B^r{}_{p1}$ is the differential receiver delay between frequencies L1 and L2, and $I = I_1 - I_2$ gives the ionosphere delay. Hofmann-Wellenhof et al. (1992) define the ionosphere delay as

$$I = \tfrac{40.3}{f^2} TEC, \tag{4.7}$$

where 40.30 is the constant coefficient. Substitute equation 4.7 into equation 4.6 to yield:

$$P_2 - P_1 = 40.3 TEC \left(\tfrac{1}{f_2^2} - \tfrac{1}{f_1^2}\right) + b^s_p + B^r_p, \tag{4.8}$$

Solving the *TEC* for pseudorange data at two frequencies produces

$$TEC = \tfrac{1}{40.3}\left(\tfrac{f_1^2 f_2^2}{f_1^2 - f_2^2}\right)\left[(P_2 - P_1) - \left(b^s_p + B^r_p\right)\right], \tag{4.9}$$

Then, the expression of *TEC* obtained from the pseudorange measurements is

$$TEC = 9.524\left[(P_2 - P_1) - \left(b^s_p + B^r_p\right)\right], \tag{4.10}$$

By neglecting the bias term from the equation, *TEC* can be represented in TECU units:

$$TEC = 9.524\left[(P_2 - P_1)\right], \tag{4.11}$$

1 TECU is equal to 10^{16} electrons/m^2. According to Araujo-Pradere (2005), code pseudorange measurements provide unambiguous but noisy and imprecise *TEC* results.

4.4 Carrier Phase Measurement

The carrier phase refers to the phase difference between the internal oscillator of the receiver and the satellite's signal (Hofmann-Wellenhof et al., 1992; Farrell and Barth, 1999; El-Rabbany, 2002; Misra and Enge, 2006). The phase refers to the unit of the cycle for a whole carrier wave. The range of a signal is calculated by changing the receiver's phase to match the received phase, multiplied by the carrier wavelength (El-Rabbany, 2002; Misra and Enge, 2006). This includes both full and partial carrier cycles. Electronics can accurately determine the fractional carrier phase to within 1% of the wavelength, equivalent to millimeter precision (Xu and Xu, 2016). This explains why phase measurements are more accurate than code pseudorange. Because of the uncertainty of the first carrier phase, the total number of complete carrier cycles between the receiver and the satellite cannot be determined (Hofmann-Wellenhof et al., 1992; El-Rabbany, 2002; Xu and Xu, 2016). Thus, measuring the carrier phase is equivalent to counting both the entire carrier waves and the received fractional phase (El-Rabbany, 2002; Misra and Enge, 2006; Xu and Xu, 2016). According to (Gao et al., 2002; Choi et al., 2011; Sabzehee et al., 2018), the measured carrier phase at L1 and L2 frequencies can be expressed as

$$\phi_1 = \rho + c(dt - dT) + d_{orb} + d_{trop} + \lambda_1 N_1 - I_1 + b^s_{\phi_1} - B^r_{\phi_1} + \epsilon\left(\phi_1\right), \qquad 4.12$$

$$\phi_2 = \rho + c(dt - dT) + d_{orb} + d_{trop} + \lambda_2 N_2 - I_2 + b^s_{\phi 2} - B^r_{\phi 2} + \epsilon\left(\phi_2\right), \qquad 4.13$$

In Equations 4.12 and 4.13, λ_1 and λ_2 are carrier signal wavelengths at L1 and L2 frequencies, N_1 and N_2 are integer ambiguities, I_1 and I_2 are ionospheric delays, $b^s_{\phi_1}$ and $b^s_{\phi_2}$ are satellite delays or interfrequency biases (m), $B^r_{\phi_1}$ and $B^r_{\phi_2}$ are carrier phase receiver delays (m), and $\epsilon(\phi_1)$ and $\epsilon(\phi_2)$ are carrier phase measurement noises with multipath errors. The *TEC* can be calculated from carrier phase observations using the same equation as for code pseudo range measurements.

$$TEC = \tfrac{1}{40.3}\left(\tfrac{f_1^2 f_2^2}{f_1^2 - f_2^2}\right)\left[(\phi_2 - \phi_1) - \left(b^s_p + B^r_p\right)\right], \qquad 4.14$$

Thus, the expression of *TEC* obtained from the carrier phase measurements is

$$TEC = 9.524\left[(\phi_2 - \phi_1) - \left(b^s_p + B^r_p\right)\right], \qquad 4.15$$

Solving for a *TEC* value free of ambiguity and biases yields

$$TEC = 9.524\left[(\phi_2 - \phi_1)\right], \qquad 4.16$$

which is precise (Araujo-Pradere, 2005).

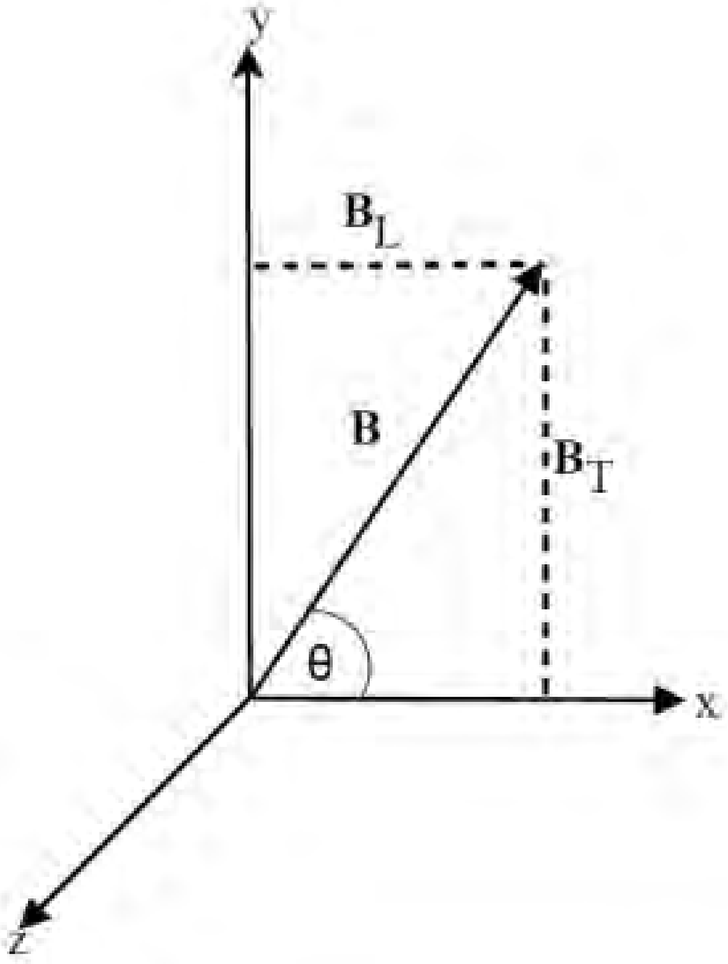

Figure 4.4: A schematic illustration of the system of orthogonal axes (Davies, 1990).

4.5 The effect of the Ionosphere on GPS

Signals generated by GPS satellites travel through the ionosphere to the GPS receiver. According to Misra and Enge (2006), these signals are assumed to travel through the ionosphere at the speed of light. GPS signals bend as they travel through the ionosphere, following Fermat's principle. According to Hofmann-Wellenhof et al. (1992), Fermat's principle states that GPS signals, radio waves, or light waves take the shortest path between two points. Appleton Lassen's equation describes how radio waves propagate in the ionosphere based on the Earth's magnetic field (Rishbeth and Garriott, 1969). According to Rishbeth and Garriott (1969), the refractive index n can be expressed using the following equation:

$$n^2 = 1 - \frac{X(1-X)}{(1-X)-\frac{1}{2}Y_T^2 \pm \left[\frac{1}{4}Y_T^2+(1-X)^2Y_L^2\right]^{\frac{1}{2}}}, \qquad 4.17$$

The equation above is also known as the Appleton-Hartree formula (Zolesi and Cander, 2014), where,

$X = \frac{N_e e^2}{M_e \omega^2 \epsilon_0} = \frac{\omega_p^2}{\omega^2}$,

$Y_L = \frac{eB_L}{M_e \omega} = \frac{\omega_{ce}}{\omega}$,

$Y_T = \frac{eB_T}{M_e \omega}$,

$Z = \frac{v}{\omega}$,

Where the variables are as such:

B: the geomagnetic field strength,

N_e: electron density,

e: electron charge (-1.602×10^{-19} C),

ϵ_0 : the electric permittivity of free space (8.854×10^{-12} Fm^{-1}),

M_e : electron mass (9.11×10^{-31} kg),

ω: angular wave frequency,

ω_p : angular plasma frequency, and

v: electron collision frequency with heavy particles,

$Y_L = Y\ cos\ \theta$ and $Y_T = Y\ sin\ \theta$, where, as schematically shown in Figure 4.4 (Rishbeth and Garriott, 1969; Davies, 1990), the two subscripts L and T stand for the longitudinal and transverse components of the imposed magnetic field, and θ is the angle between the direction of propagation of the radio waves and the Earth's magnetic field. The system of orthogonal axes is schematically illustrated in Figure 4.4 (Davies, 1990). Extra-ordinary waves are denoted by a negative sign and ordinary waves by a plus sign (Rishbeth and Garriott, 1969). Neglecting both collision and magnetic field effects, equation 4.17 can be simplified to

$$n^2 = 1 - \frac{X(1-X)}{1-X} = 1 - X, \qquad 4.18$$

After expanding equation 4.18, the solution yields

$$n = 1 - \frac{1}{2}X + \frac{\frac{1}{2}\left(\frac{1}{2}-1\right)}{2!}X^2 + \ldots \qquad 4.19$$

Since the higher order powers often contribute far less than the first order term at higher frequencies in the ionosphere, they are disregarded. The approximation for the refractive index is:

$$n \approx 1 - \tfrac{1}{2}X = 1 - \tfrac{1}{2}\tfrac{\omega_p^2}{\omega^2} \ , \qquad 4.20$$

where,

$$\omega_p^2 = 2\pi f_p \ , \ \omega^2 = 2\pi f, \qquad 4.21$$

f_p is the plasma frequency (Hz), while f is the signal carrier frequency (Hz). Substituting 4.21 into equation 4.20 to obtain

$$n \approx 1 - \tfrac{1}{2}\left(\tfrac{2\pi f_p}{2\pi f}\right)^2 = 1 - \tfrac{1}{2}\tfrac{f_p^2}{f^2} \ , \qquad 4.22$$

Rishbeth and Garriott (1969) defined plasma frequency as

$$f_p^2 = \tfrac{N_e e^2}{4\pi^2 m_e \epsilon_0} \ , \qquad 4.23$$

and then, substituting the relevant constants in 4.23 yields

$$f_p^2 = \tfrac{\left(-1.602\times10^{-19} \ C\right)^2}{4\pi^2(9.11\times10^{-31} \ kg)\left(8.854\times10^{-12} \ Fm^{-1}\right)} N_e = 80.594 N_e, \qquad 4.24$$

Equation 4.22 can be substituted for equation 4.24 to obtain

$$\begin{aligned} n &\approx 1 - \tfrac{1}{2}\tfrac{80.594 N_e}{f^2} \ , \\ n_\phi &\approx 1 - \tfrac{40.30 N_e}{f^2} \ , \qquad 4.25 \end{aligned}$$

Therefore, the phase refractive index is used to express the group refractive index as follows (Hofmann-Wellenhof et al., 1992).

$$n_g = n_\phi + f\tfrac{dn_\phi}{df} \ , \qquad 4.26$$

When the phase refractive index is differentiated, it results in

$$dn_\phi = \tfrac{40.30 N_e}{f^3} df, \qquad 4.27$$

To obtain the group refractive index, substitute equations 4.25 and 4.27 into equation 4.26.

$$n_g = 1 + \tfrac{40.30 N_e}{f^2}, \qquad 4.28$$

Consequently, the wave's group velocity and phase are given as

$$\begin{aligned} v_\phi &= \tfrac{c}{1-\frac{40.3 N_e}{f^2}} \ , \\ v_g &= \tfrac{c}{1+\frac{40.3 N_e}{f^2}} \ , \qquad 4.29 \end{aligned}$$

GPS satellite signals travel through the ionosphere to reach the GPS receiver. GPS signals take longer to reach a receiver from a satellite (τ) due to the non-uniform composition of the ionosphere compared to passing through a vacuum (τ_0) (Hofmann-Wellenhof et al., 1992; Misra and Enge, 2006). The ionospheric time delay is defined as the difference between these times ($\Delta\tau = \tau - \tau_0$). The radio signal's propagation time from satellite to receiver is calculated by incorporating the refraction profile index throughout the journey (Misra and Enge, 2006).

$$\tau = \frac{1}{c}n(l)\ dl, \qquad 4.30$$

In Equation 4.30, $n(l)$ represents the medium's refractive index, c is the speed of light in vacuum, S is the satellite, and R is the receiver. If the ionosphere behaves like a vacuum, signal travel time is

$$\tau_0 = \frac{1}{c}1\ dl, \qquad 4.31$$

An expression for excessive delay in signal propagation owing to refraction can be stated as:

$$\Delta\tau = \frac{1}{c}[n(l) - 1]\ dl, \qquad 4.32$$

whereas the following represents the corresponding path length delay:

$$\Delta\rho = \frac{1}{c}[n(l) - 1]\ dl, \qquad 4.33$$

Equation 4.31 can be substituted into equations 4.32 and 4.33 to obtain the excess phase delay (in seconds) that a signal experiences while traveling through the ionosphere that is expressed as

$$\begin{aligned} &\Delta\tau_\phi = -\frac{1}{c}\frac{40.3N_e(l)}{f^2}\ dl = -\frac{40.3}{cf^2}TEC, \\ &I_\Phi = c\Delta\tau_\phi = -\frac{40.3}{f^2}TEC, \qquad 4.34 \end{aligned}$$

In a similar manner, group delay is stated as follows in both seconds and meters:

$$\begin{aligned} &\Delta\tau_g = \frac{40.3}{cf^2}TEC, \\ &I_\rho = \frac{40.3}{f^2}TEC, \qquad 4.35 \end{aligned}$$

TEC, as described by (Hofmann-Wellenhof et al., 1992; Misra and Enge, 2006), is the total number of electrons integrated along the path from the receiver to each GPS satellite. TEC can be expressed mathematically as

$$TEC = N_e\ dl, \qquad 4.36$$

where N_e represents electron density (Hofmann-Wellenhof et al., 1992; Araujo-Pradere, 2005; Misra and Enge, 2006). Hofmann-Wellenhof et al. (1992) described TEC as an indicator of ionospheric fluctuation, derived from free electron modified

GPS signals. The Slant Total Electron Content (STEC) refers to the TEC measured along the satellite-receiver signal path. STEC is determined by the ray path geometry across the ionosphere, resulting in an equivalent vertical value of TEC (VTEC) that is not affected by ray path elevation (Hofmann-Wellenhof et al., 1992; Silwal et al., 2021). VTEC values are attained if a satellite passed directly overhead a specific geographic location. To do this, assume the ionosphere is a thin shell at 350 km altitude, as depicted in Figure 4.5 (Klobuchar, 1986; Seemala, 2023). The ionospheric pierce point (IPP) refers to the estimated geographic place where the line of sight intersects the shell.

Figure 4.5 depicts the projection of STEC from the satellite line of sight onto VTEC at the ionospheric piercing point (IPP). According to (Hofmann-Wellenhof et al., 1992), the IPP is the point where the GPS signal meets the ionospheric shell. According to (Hofmann-Wellenhof et al., 1992); Silwal et al., 2021), the process of converting STEC to VTEC involves

$$VTEC = STEC \times \cos\ \chi' \ , \tag{4.37}$$

Where

$$\sin\ \chi' \ = \tfrac{R_E}{R_E+h} \cos\ \theta \ \ , \tag{4.38}$$

Hence,

$$VTEC = STEC \times \cos\ \left[\left(\tfrac{R_E}{R_E+h_m} \right) \right] \ , \tag{4.39}$$

Given that: R_E, χ, χ', h_m is the Earth's radius; which is about 6,371 km, the satellite's elevation angle (degrees), the zenith angle (degrees), and the expected ionosphere height respectively.

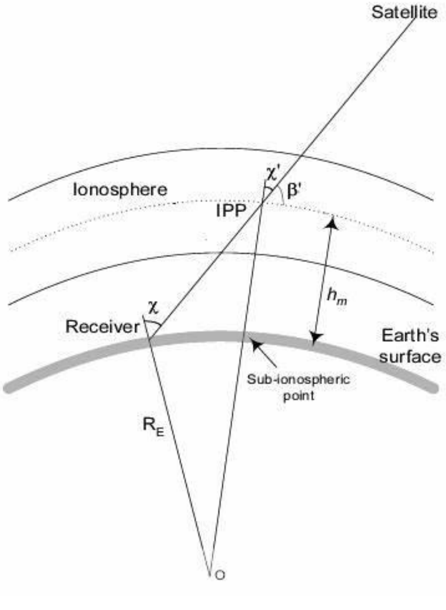

Figure 4.5: The VTEC value obtained from STEC (Silwal et al., 2021).

4.6 GPS Data Processing

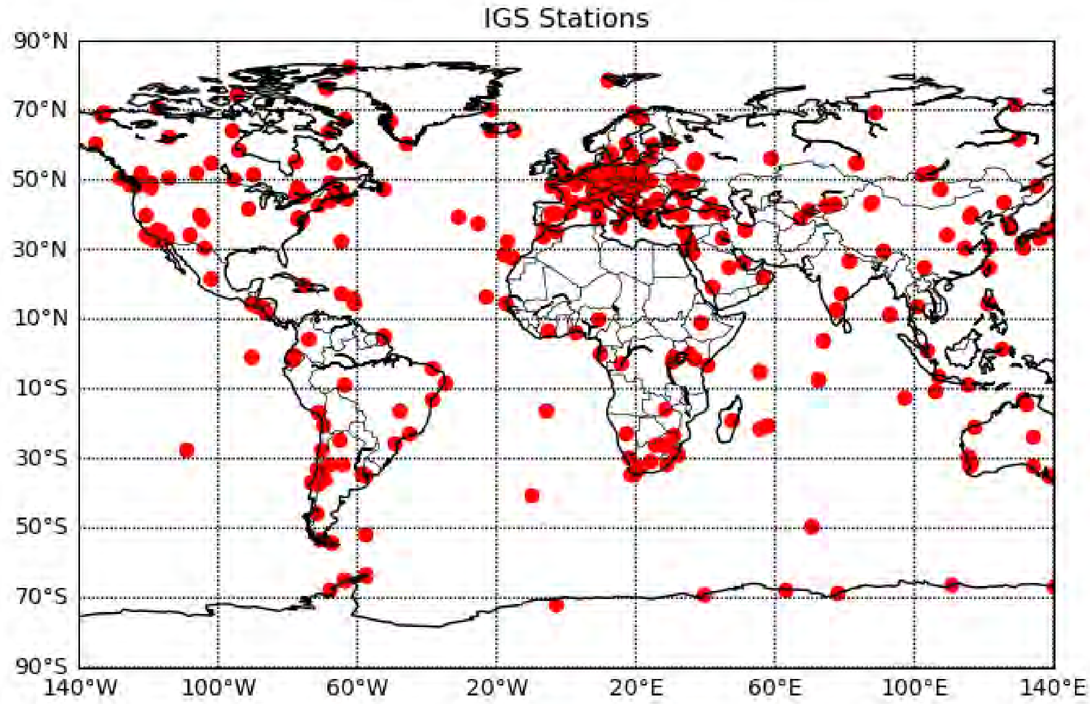

Figure 4.6: GNSS receiver stations (red dots) (https://igs.org/). Some receiver stations are not shown as they were obtained from different data sources

TEC data from the African-European sector was obtained using Global Navigation Satellite Systems (GNSS). The University NAVSTAR Consortium (UNAVCO: www.unavco.org/), the International GNSS Service (IGS) network (https://igs.org/), and South Africa's Trignet (ftp://ftp.trignet.co.za/) were the sources of the GNSS data. Figure 4.6 depicts the geographical position of GNSS stations, which are largely within the IGS network. The GNSS data was collected over the African-European sectors within the longitudinal range of 20–40° E. VTEC was derived from receiver independent exchange records using the GPS TEC software created at Boston College (Seemala and Valladares, 2011; Uwamahoro et al., 2018; Seemala, 2023). The program determines the phase and code TEC values, as well as the azimuth and elevation of the appropriate satellite, by reading the raw GPS data from the RINEX files (Uwamahoro et al., 2018). This software makes use of receiver biases that are determined by minimizing the TEC variation between 02:00 and 06:00 LT and differential satellite biases that are released by the University of Bern (Seemala and Valladares, 2011; Uwamahoro et al., 2018). The equivalent VTEC is computed at an IPP height of 350 km, assuming a thin shell model (Uwamahoro et al., 2018). Only TEC values corresponding to elevation angles over 20° were used during data processing in order to minimize the impacts of multipath (Habarulema et al., 2018; Uwamahoro et al., 2018). Figure 4.7 shows estimation of dTEC using a Savitzky-Golay algorithm for all PRNs over Aliwal North station (30.68° S, 26.72°E), South Africa on 13 March 2014. Figure 4.7a) illustrates original VTEC data and the Savitzky-Golay algorithm of VTEC values. Figure 4.7b) displays the filtered VTEC time series, indicated by dTEC, which was derived by subtracting the Savitzky-Golay algorithm TEC from the original time series.

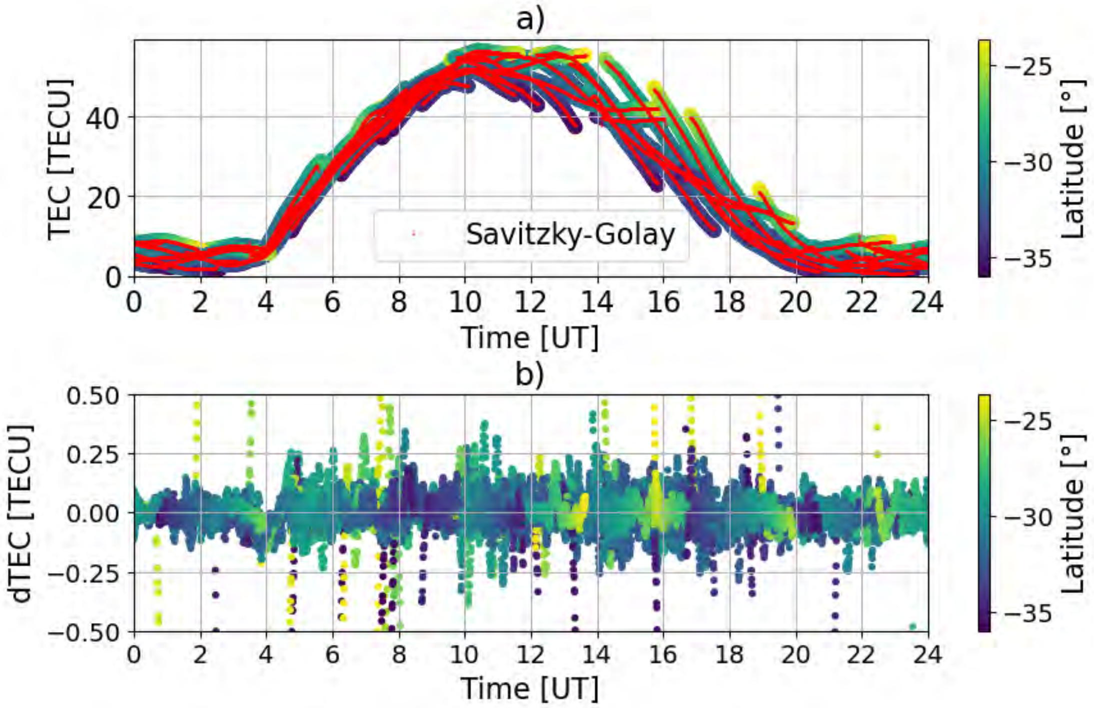

Figure 4.7: Estimation of dVTEC using a Savitzky-Golay algorithm for all PRNs over Aliwal North station (30.68° S, 26.72°E), South Africa on 13 March 2014.

4.7 Methodology

Two methods were utilized to ascertain the propagation characteristics of TID activity, which is observed by a period of enhancement and depletion of dTEC: the method of linear regression was employed for estimating velocities, and the continuous wavelet transform was utilized to determine periods. The method of linear regression for the determination of the velocity of TID activity are based on information presented in (Liu et al., 2019; Thaganyana et al., 2022).

4.7.1 dTEC Maps

GPS receiver-derived VTEC measurements contain a diurnal trend. Figure 4.7 shows the VTEC measurement taken by a receiver station at Aliwal North station (30.68° S, 26.72°E), South Africa on March 13, 2014. This random date was chosen to demonstrate normal diurnal TEC variation and data processing followed for identifying TID activity features. To minimize multipath effects, satellite data below an elevation angle of 20 ° was eliminated. To identify other patterns in VTEC measurements, Savitzky-Golay algorithm were used to remove the prominent diurnal trend (Osie-Poku et al., 2021). Figure 4.8a) illustrates the Savitzky-Golay algorithm of VTEC values from a single GPS satellite (PRN 31). Figure 4.8b) displays the filtered VTEC time series, indicated by dTEC, which was derived by subtracting the Savitzky-Golay Algorithm TEC from the original time series. Figures 4.8a) and 4.8b) clearly show wave structures (periodic oscillations) between 01:00 and 05:00 UT.

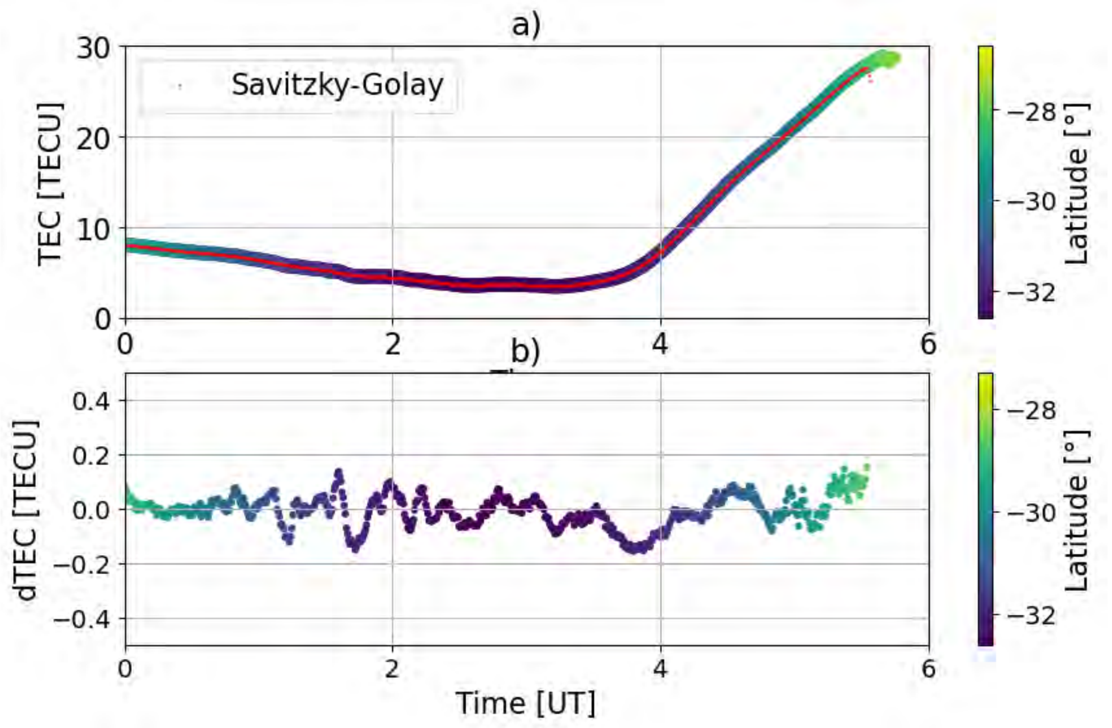

Figure 4.8: Estimation of dTEC by means of a Savitzky-Golay algorithm for one PRN over Aliwal North station (30.68° S, 26.72°E), South Africa on 13 March 2014.

$$vT^{f}(t)_{\,i,j} = b_p \,.\, t_{i,j}{}^{p} + b_{p-1} \,.\, t_{i,j}{}^{p-1} + \ldots + b_1 \,.\, t_{i,j}{}^{1} + b_0 \,.\, t_{i,j}{}^{0}\ ,$$
$$\mathrm{dTEC} = \mathrm{VTEC_o} - vT^{f}(t), \qquad 4.40$$

where $\mathrm{VTEC_o}$ is the observed VTEC, $vT^{f}(t)$ is the VTEC obtained from the fitting model and dTEC is the detrended TEC. where $j = 1, 2, 3, \ldots, 32$ represent the number of satellites; $i = 1, 2, 3, \ldots, 140+$ is the number of GNSS receiver locations, p is the polynomial order. $\mathrm{vT^f}$ is the expanded form of the Savitzky-Golay algorithm.

Figure 4.8 shows how the same approach was used to estimate dTEC throughout the day using all PRNs from the Aliwal North Station. The same approach was used to calculate dTEC for data from various stations. Using estimated dTEC, a two-dimensional (2d) map of dTEC can be created based on the time and latitude of a particular day. The 2d map was created by binning the dTEC data into 5 min × 1° (time and latitude) intervals. The diurnal TEC maps for chosen latitudinal ranges were generated within a 20° longitudinal sector (Habarulema et al., 2022;

Thaganyana et al., 2022).

Figure 4.9 depicts 2d dTEC map over the African-European longitude sector on 10 April 2015 within the longitudinal range of 20°-40°E and latitudinal range of 40°S-60°N. The GNSS receiver network is not available at 20 N and 10° S, resulting in data gaps (white spaces). Figure 4.9 shows how dotted lines are utilized to match the TID activity structure and calculate velocities. Figures 4.9 also show the estimated geomagnetic equator at 10° N (Habarulema et al., 2018), represented by horizontal black line. The fitted data points on the dTEC maps in Figure 4.9 contains longitude, latitude and time. In order to calculate the azimuth angle, longitude and latitude are needed. The propagating azimuth angle of TIDs were estimated by means of these fitted data points (Thaganyana et al., 2022).

We observe equatorward TIDs in Figures 4.9; between 60° N - 40° S and the time interval of 8 -10 UT, between 40° N - 28° °S and the time interval of 1 -2 UT , a poleward TID between 10° N - 10° S and the time interval of 6 -8 UT and equatorward TID between 20° S - 40° S and the time interval of 10 -12 UT with the speed of 425 m/s, 354 m/s, 349 m/s and 302 m/s respectively and periods of 80 min, 80 min, 111 min and 177 min with the azimuth angle of 122°, 123°, 122° and 33°. The figure demonstrates the linear regression method using dTEC (time and latitude) maps. The linear regression method is used to fit maximum dTEC within a bin interval of 1 degree latitude and 10 minutes range. Keeping the interval constant, the time was increased by 10 minutes. The black dots represent the maximum dTEC values for each latitude-time bin. The latitude data were converted to distance (km) to calculate the meridional speed. The TIDs' meridional velocity was calculated based on the gradient of fitted lines.

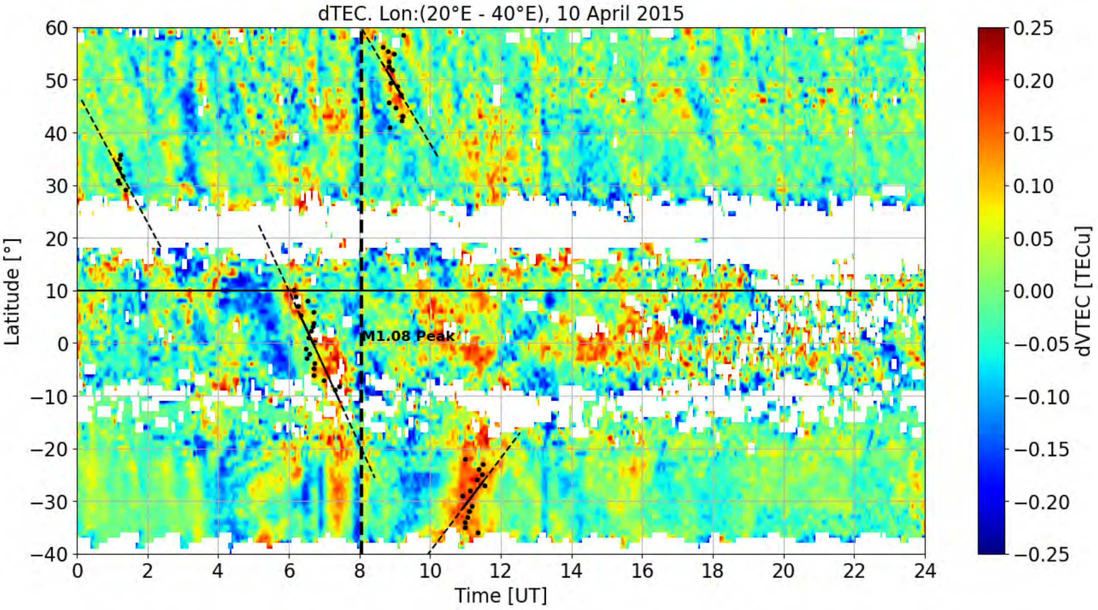

Figure 4.9: Cases of equatorward medium-scale TIDs which appear to have originated from the mid-latitudes during quiet conditions on 10 April 2015.

The average speed, period, azimuth angle of TID activity in the northern hemisphere was 390 m/s, 80 min, and 122°. The fitted data points on the TEC maps in Figures 4.9 include longitude, latitude, and time. The estimates of the propagation azimuth of TID activity were 32.55° (clockwise from north) and 122.4° (clockwise from north) in the southern hemisphere and northern hemispheres, respectively. Multiplying the period and speed of TID activity yields the wavelength.

The horizontal phase speed (c_{H}) was calculated as follows (Vadas and Becker, 2018):

$$c_H = \frac{1}{\sqrt{\frac{1}{c_x^2} + \frac{1}{c_y^2}}}, \tag{4.41}$$

where c_{x} and c_{y} represent the TID's phase velocities in the x and y directions, respectively.
Then the following formula was used:

$$\begin{aligned} c_x &= \frac{\omega_r}{k}, \\ c_y &= \frac{\omega_r}{l}, \end{aligned} \tag{4.42}$$

where k and l denote the zonal and meridional wavenumbers that can be determined using the equations below:

$$\begin{aligned} k &= k_H \times \sin\,(\phi)\ , \\ l &= k_H \times \cos\,(\phi)\ , \end{aligned} \tag{4.43}$$

Equation 4.41 can be expressed in terms of meridional propagation velocity and azimuth, where $k_{\mathrm{H}} = 2\pi/\lambda_H$ represents the horizontal wavenumber, ϕ is the azimuth (clockwise from north), and λ_H is the horizontal wavelength. Then equation 4.40 becomes:

$$c_H = \frac{c_y}{\sqrt{(1+(\tan(\theta))^2)}}, \tag{4.44}$$

The equation shown above was used to determine c_{H}. The computed c_{H} values for the northern hemisphere and southern hemisphere were 182.20 m/s and 254.34 m/s, respectively.

4.7.2 Continuous Wavelet Analysis

The technique known as continuous wavelet transform (CWT) breaks down a time series into frequency-time domain. Convolution using a scaled wavelet is the method used to accomplish this (Torrence and Compo, 1998). A real or complex wavelet (ψ(t)) is a function that fulfils

$$\psi(t) = 0, \tag{4.45}$$

and has temporal and frequency localization (Farge, 1992). A mother wavelet is one such wavelet that can be translated in time and dilated, or stretched or shrunken (Torrence and Compo, 1998). ψ_t becomes $\psi_{t,\tau}$ (t) when the dilation and translation parameters (s and τ) are applied.

$$\psi_{s,\tau}(t) = \frac{1}{\sqrt{s}}\psi\left(\frac{t-\tau}{s}\right), \qquad 4.46$$

where τ is a location parameter that moves the wavelet along the time domain, s is the scaling parameter that represents the frequency, and t is the time (Mallat, 1999). A CWT of a time series, x(t), with regard to the wavelet function, ψ(t), is known as a convolution integral.

$$CWT(s,\tau) = x(t)\psi^*(t)\ dt = \frac{1}{\sqrt{s}}x(t)\psi^*\left(\frac{t-\tau}{s}\right) dt, \qquad 4.47$$

Mallat (1999) defines $\psi^*(t)$ as the complex conjugate of the investigated wavelet function ψ(t).

Morlet, the mother wavelet, was used to transform time data into frequency-time space. Figure 4.10 shows an example of a Morlet wavelet. The chosen shape resembles various geophysical parameter features (Torrence and Compo, 1998; Materassi and Mitchell, 2007; Katamzi et al., 2012; Habarulema et al., 2013).

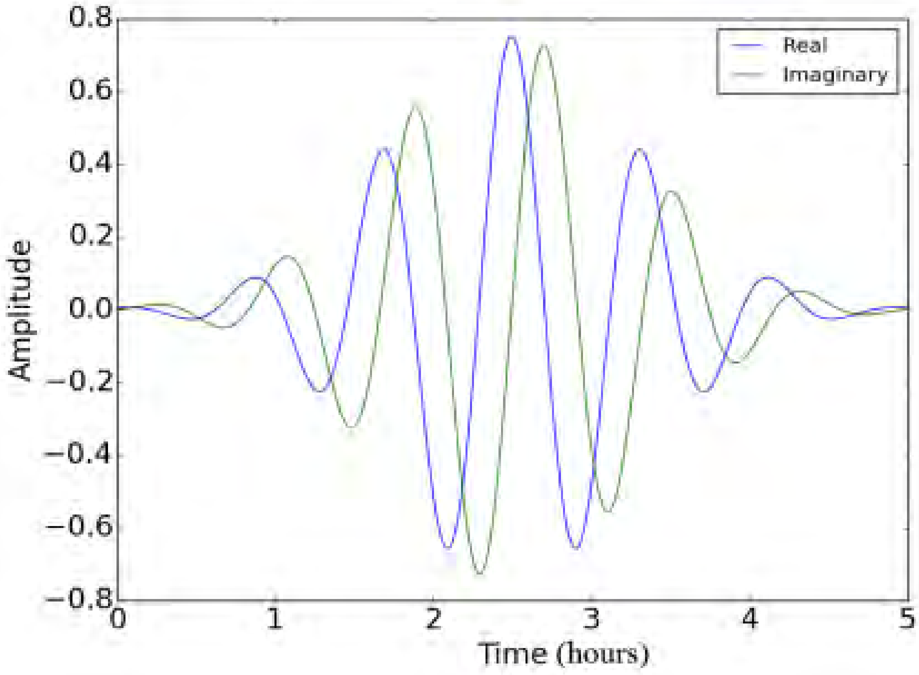

Figure 4.10: An example of Morlet wavelet.

The definition of a Morlet wavelet is

$$\psi_0(t) = \pi^{\frac{1}{4}}e^{i\omega_0 t}e^{-t^2/2}, \qquad 4.48$$

To meet the admissibility criterion (Farge, 1992), the non-dimensional frequency ω_0 is set to 6 and t denotes time. This method has been used to analyze the amplitudes and periods of TID activity in GNSS TEC data (Katamzi et al., 2012; Habarulema et al., 2013). Farge (1992), Torrence and Compo (1998), Materassi and Mitchell (2007) provide additional details on wavelets and their uses. Figure 4.11 (a) shows the dTEC perturbations for latitudes 50° ± 0.5° N, longitudinal sector of 20° -40° E in the northern hemisphere. The dTEC perturbations have been extracted from the dTEC map.

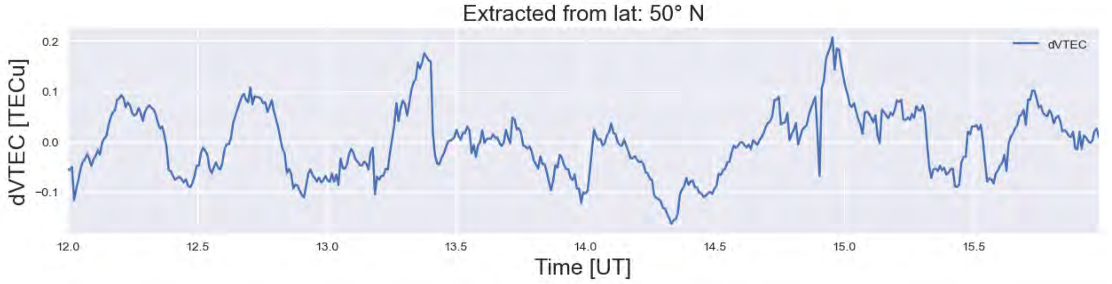

Figure 4.11a): The dVTEC perturbations for latitudes 50° ± 0.5° N

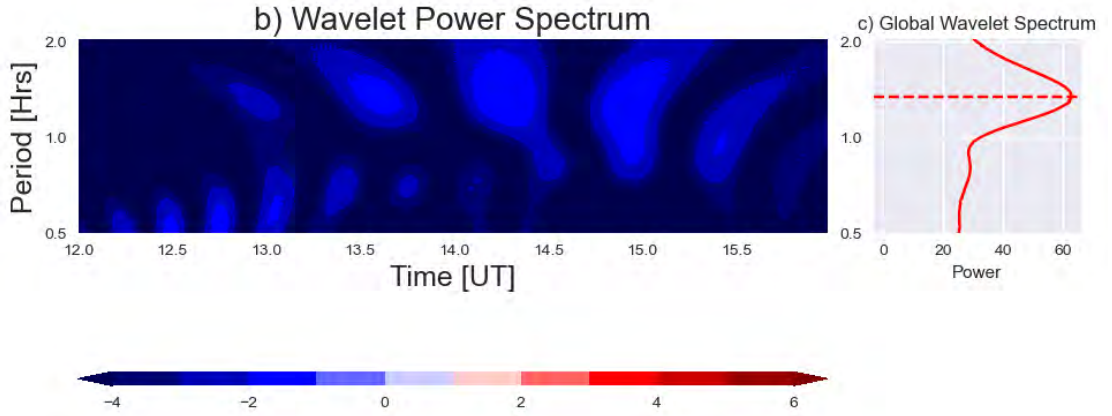

Figure 4.11: Power spectrum of wavelet transform over African-European sector computed for 50° N

Wave modes propagate for approximately 80 minutes.

To estimate the wavelength of the TID activity, we used well-known formulas (Alonso and Finn, 1967):

$$P = \frac{1}{f} \qquad 4.49$$

And

$$\lambda = \frac{v}{f} \qquad 4.50$$

4.8 Summary

This chapter outlined the research methods and data sources used in this thesis. A basic introduction of GPS and its segments is provided, as well as a discussion of how TEC is calculated from GPS data. The chapter also outlined techniques for identifying and characterizing TID activity. Signal analysis methods include CWT and linear regression. The findings and discussion are presented in the following chapter.

Chapter 5: Results and Discussion

This chapter discusses the statistical analysis of observations of poleward TID activity of equatorial origin and equatorward TID activity of high latitude region origin over the African-European sector during geomagnetically disturbed conditions between 2006 and 2022. Our method detected 196 TID activities propagating over the African-European sectors within the longitudinal range of 20–40° E between the period of 2006 and 2022. Of these TID activities, 161 and 33 were observed during geomagnetic storms, and simultaneous occurrence of geomagnetic storms and solar flares, respectively. The criterion for geomagnetically disturbed conditions were Dst $\leq$ -30 nT. Days of geomagnetic storm activity from 2006-2022 can be found on these websites: https://www.sidc.be/cactus/catalog/LASCO/250/cmelz.txt and https://cdaw.gsfc.nasa.gov/CME_list/. TEC data from GNSS was utilized to determine TID activity.

5.1 Example of TID Activities during disturbed conditions

The storm known as St Patrick's day was selected randomly and used to show and discuss the identification of equatorward TID activity before moving on to statistics. Data for African-European sector was considered within latitudes 40° S-60° N and 20 °-40 ° E. The meridional propagation velocity, period, and wavelength of the TID activities have been determined using the methods described in Section 4.4.

The storm on March 17, 2015, was generated by a coronal mass ejection (CME) that hit the Earth's magnetosphere around 0445 UT. Other sources have provided interplanetary and geomagnetic activity indices for the 17 March 2015 storm (e.g., Astafyeva et al., 2015; Ramsingh et al., 2015; Borries et al., 2016; Fagundes et al., 2016; Kuai et al., 2016; Nava et al., 2016; Zakharenkova et al., 2016). Figure 5.1 shows variations in solar wind velocity, Vsw (kilometers per second, km/s), and Bz component of the interplanetary magnetic field, IMF Bz (nanoTeslas, nT), Dst (nT) index, auroral electrojet (AE) index. The AE and Dst indices were obtained from (http://wdc.kugi.kyoto-u.ac.jp/wdc/Sec3.html). Other indeces were obtained from OMNI Data. The Vsw increased from roughly 400 km/s to 500 km/s during the sudden storm commencement (SSC). Simultaneously, the IMF Bz turned north, reaching around 26 nT at 0523 UT before temporarily reverting south. Bz fluctuated between north and south until ≈ 1146 UT, when it stayed south for over 12 hours (except for a small northward shift at ≈1337 UT) (Astafyeva et al., 2015; Borries et al., 2016; Fagundes et al., 2016; Kuai et al., 2016; Nava et al., 2016; Ramsingh et al., 2015; Zakharenkova et al., 2016). “Following the SSC, the AE index gradually increased before decreasing at approximately 1200 UT on March 17, 2015. During the main phase, it increased significantly, reaching a peak of 2,298 nT at 1358 UT. The Dst index decreased to -223 nT at 2247 UT on March 17, 2015, following a minimal of -87 nT at 0937 UT the previous day” (Habarulema et al., 2018).

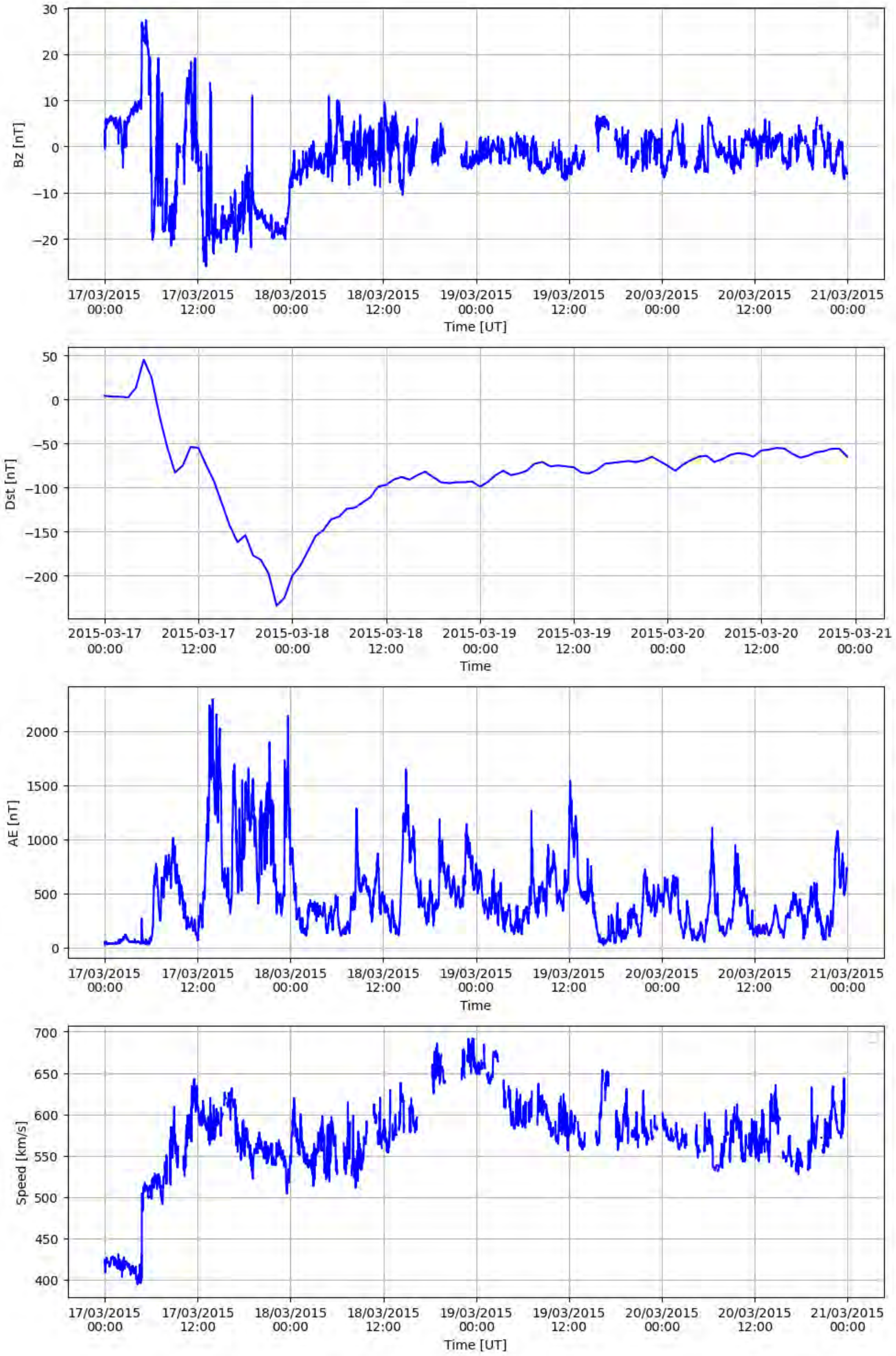

Figure 5.1: Geomagnetic conditions for 17–21 March 2015.

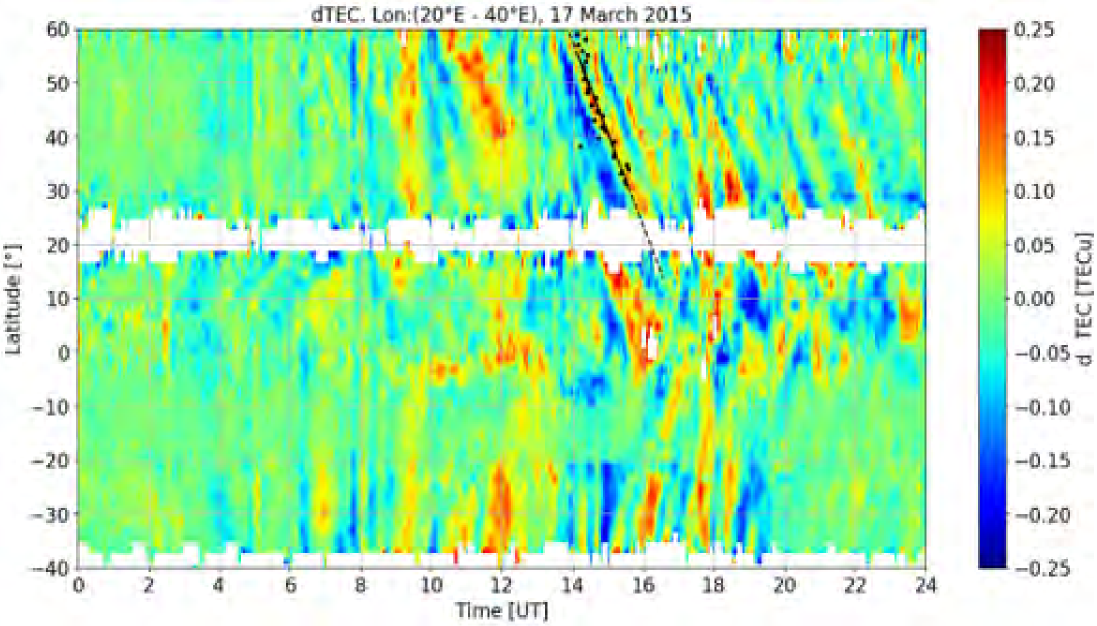

Figure 5.2: Variation of dTEC (TECU) over Africa-European sector on March 17, 2015

Figure 5.2 depicts dTEC as a function of latitude and time on March 17, 2015, within the latitude and longitude ranges of 40 ° S-60 ° N and 20 °-40 ° E, respectively. Figure 5.2 shows that a TID structure emerged in the northern hemisphere between 14:00 and 16:00 UT on the day of the storm's main phase. To determine a TID activity, each identified TID track is fitted as demonstrated in Figure 5.2 (starting at around 1400 UT). The estimated velocities are then averaged to obtain the velocity value of the TID activity on a given day. The velocity was 419.35 ± 9.1 m/s, and the period was 55 ± 8 minutes. Borries et al. (2016) estimated the characteristics wavelength: ≈2100 km, period: ≈60 min, and speed ≈600 m/s, which statistically agrees with presented results. Many studies have found a correlation between AE and LSTID parameters (Hajkowicz, 1999; Ding et al., 2008; Borries et al., 2009).

Joule heating is hypothesized to cause high-latitude air surges and meridional wind patterns (Fuller-Rowell et al., 2002; Richmond et al., 2003). This demonstrates the impact of surges in auroral electrojets on LSTID formation. Joule heating is thought to cause atmospheric surges at high latitudes as well as meridional winds. The subsequent observation of a TEC enhancement with maximum amplitudes in midlatitudes lends support to the notion of storm-induced thermospheric winds, as uplifting effects caused by meridional winds are most powerful at midlatitudes (Förster and Jakowski, 2000).

The source region of the LSTIDs is gradually shifting toward the equator. This phenomenon is associated with polar cap region extension produced by plasmasphere compression (Borries et al, 2016; Belehaki et al, 2017). The heating effect in the LSTIDs source region shows that Joule heating, rather than Lorentz force, is more likely to produce LSTIDs (Tsugawa et al, 2004; Tsagouri et al, 2023; Borries et al, 2016).

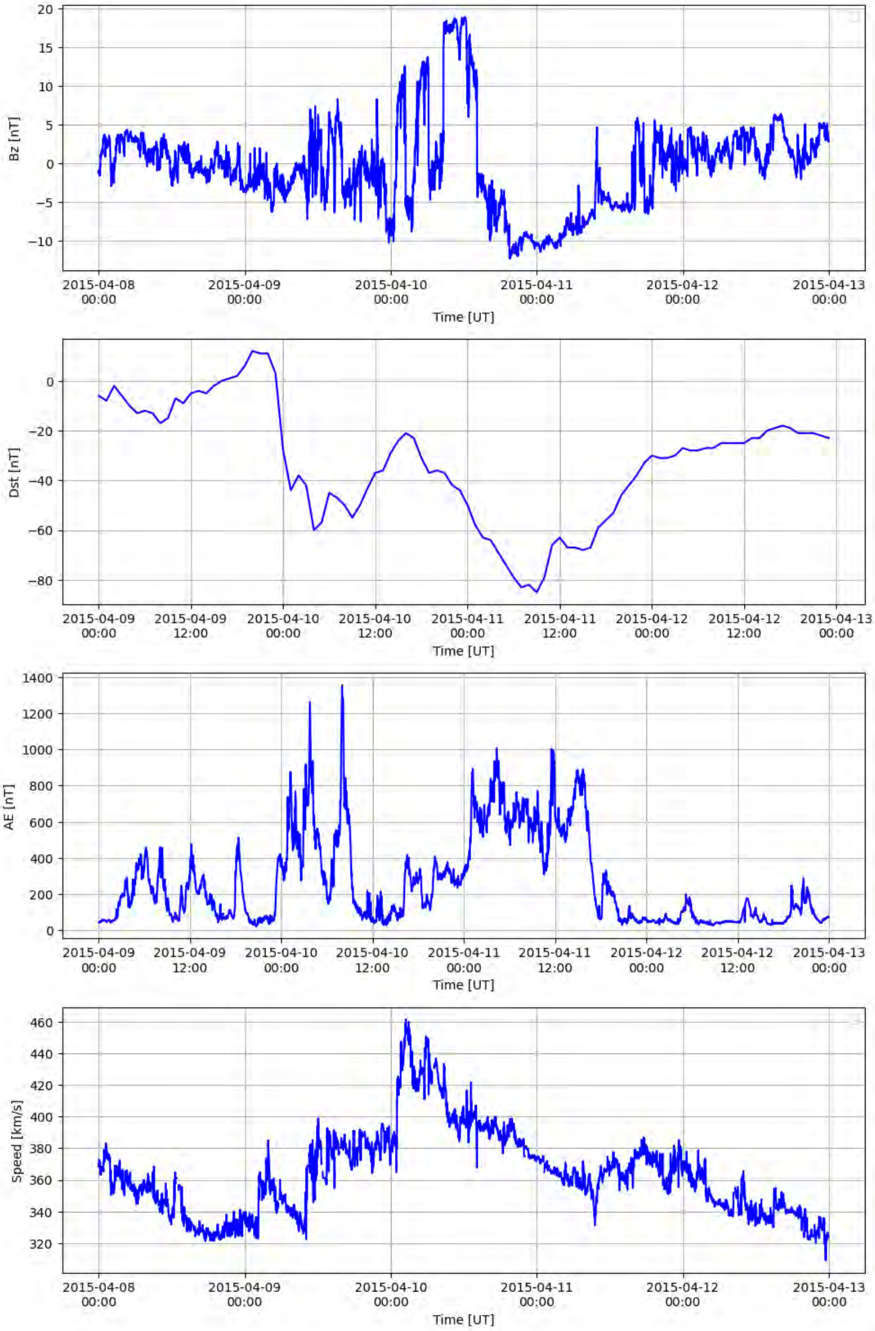

Figure 5.3: Geomagnetic conditions for 8–12 April 2015.

Figure 5.3 provides geomagnetic and solar wind activity from April 9 to April 12, 2015. The storm started on April 9, 2015 and was generated by a CME that hit the Earth's magnetosphere around 0145 UT. Figure 5.3 shows variations in Vsw, Bz, AE indices. The AE and Dst indices were obtained at http://wdc.kugi.kyoto-u.ac.jp/wdc/Sec3.html. Vsw increased from roughly 320 km/s to 460 km/s during the SSC. During the SSC, the Bz turned north, reaching around 18 nT at 1253 UT before reverting south. It stayed south for over 12 hours. After the SSC, the AE index gradually increased before decreasing to a minimum of 400 nT at around 1200 UT on April 9, 2015. During the main phase of the storm, AE index increased significantly, reaching a peak of 1200 nT at 1045 UT. The Dst index decreased to a new minimum of -83 nT at 1037 UT on April 11, 2015, following a minimum of -60 nT at 0817 UT the previous day.

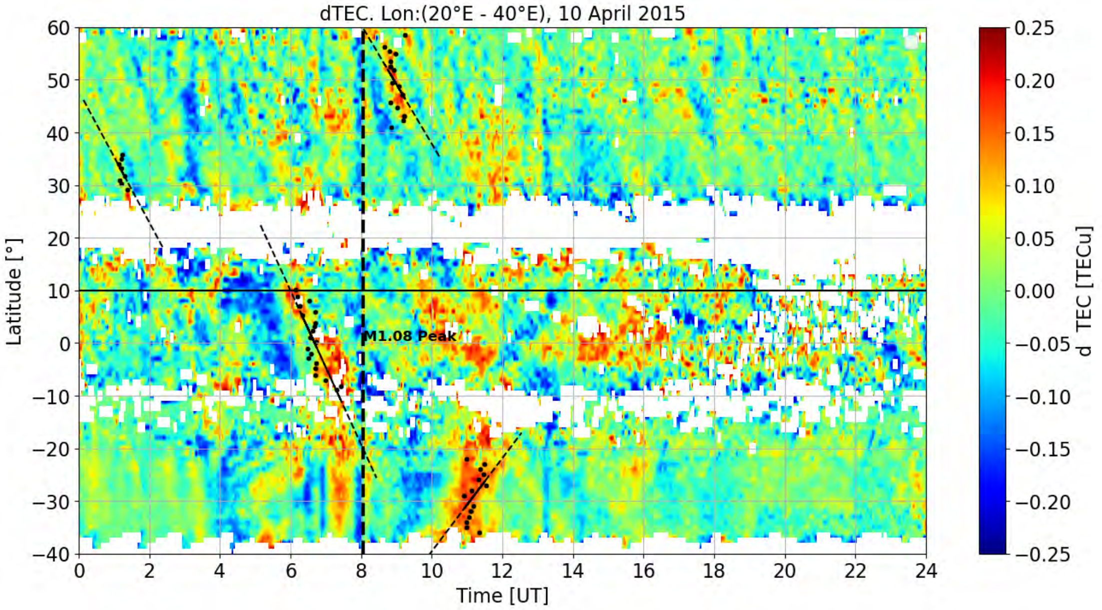

Figure 5.4: Variation of dTEC (TECU) over Africa-European sector on April 10, 2015.

Figure 5.4 is similar to Figure 5.2 but for 10 April 2015. Figure 5.4 shows that a TID structure evolved at the geomagnetic equator between 06:00 and 8:00 UT, while another TID structure emerged in the Northern Hemisphere between 08:00 and 10:00 UT and between 10:00 and 12:00 UT in the southern hemisphere. The findings for velocities and periods were 349.02 ± 32.1 m/s and 117 ± 2 min, respectively for the TID from the equator. The propagation velocity of TID activity traveling towards the equator was 340.04 m/s and 301.74 m/s in the northern hemisphere and southern hemisphere, respectively, with the periods of these equatorward TID activity being 80.4 min and 177 min in the northern hemisphere and southern hemisphere, respectively.

It is well known that the prompt penetration electric fields (PPEFs) and disturbance dynamo electric fields have an effect on the low-latitude electric field during disturbed conditions (Fejer and Scherliess, 1998; Kikuchi et al., 2008; Bagiya et al., 2011; Bagiya et al., 2014; Kikuchi and Hashimoto, 2016). The local day to dark sector of the PPEFs is eastward, and the midnight to dawn sector is westward (Fejer, 1991; Fejer, 1997; Fejer and Scherliess, 1998; Kikuchi et al., 2008). Over the equatorial latitude, PPEFs cause an increase in ΔH (vertical drift) during the day and a decrease at night (Fejer, 1997; Fejer and Scherliess, 1998; Bagiya et al., 2014). During the main phase of geomagnetic storms, PPEFs usually last for an hour (Huang, 2013; Kuai et al., 2015), but during strong storms, they can last for 6–8 hours (Huang et al., 2005; Huang, 2013). The PPEFs are linked to a southward IMF Bz and are the result of several processes related to the solar wind and magnetosphere (Fejer and Scherliess, 1998; Kikuchi et al., 2008; Bagiya et al., 2011, Bagiya et al., 2014; Kikuchi and Hashimoto, 2016). For conditions responsible for launching poleward TIDs, neutral-to-ionized component coupling becomes effective due to an increase in the Lorentz force caused by the increasing eastward electric field (Chimonas, 1969; Habarulema et al., 2015; Habarulema et al., 2016).

5.2 Statical Analysis

This section analyses poleward TIDs of equatorial origin and equatorward TID activity over the African-European sectors during geomagnetically disturbed conditions from 2006 to 2022. Poleward TIDs have received less attention than their equatorward counterparts originating from high latitude regions, which are commonly observed during geomagnetic storms. Poleward TIDs during geomagnetic storms have only lately attracted attention (Ding et al., 2013; Habarulema et al., 2015; Habarulema et al., 2016; Jonah et al., 2018; Ngwira et al., 2019). Research on poleward TIDs of equatorial origin during geomagnetic storms has been mostly done on case-by-case (Ding et al., 2013; Habarulema et al., 2015; Habarulema et al., 2016; Jonah et al., 2018; Ngwira et al., 2019). MSTIDs have periods and velocities ranging from 15 to 60 minutes and 100 to 250 m/s, respectively (Hunsucker, 1982; Kersley and Hughes, 1989). Most LSTIDs have periods ranging from 1 hour to 3 hours and velocities of 300-1,000 m/s, while some studies have reported periods ranging from 30 minutes to three hours (Hunsucker, 1982; Hocke and Schlegel, 1996). Thus, while classifying MSTIDs and LSTIDs, there may be some "overlap" in either period or velocity values. The study is done during geomagnetic storms and during simultaneous occurrence of geomagnetic storms and solar flares and it is well known that high solar activity periods exhibit higher occurrences of geomagnetic storms. Since there is additional energy coming from the solar flare, the study statistically investigates how simultaneous occurrence of geomagnetic storms and solar flares affects TIDs as compared to the cases of geomagnetic storms only. Furthermore, equatorward LSTIDs are launched from high latitudes during geomagnetic storms. The analysis is done by separately presenting different TID activities during main and recovery phases and in different hemispheres.

In this study, MSTIDs are considered to have period of 30 minutes- 1 hour and velocities in the range 100-250 m/s. LSTIDs have periods and velocities in the range of 1-3 hrs and 250-400 m/s, respectively.

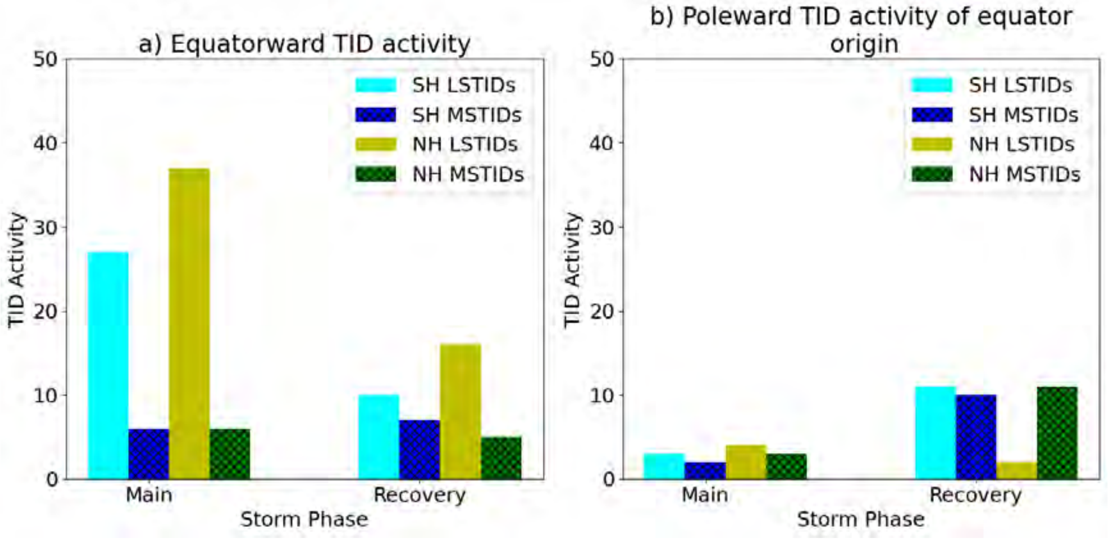

Figure 5.5: Occurrence of TID activities during geomagnetic storms between 2006-2022.

Figure 5.5 represents the analysis of the occurrence of equatorward TID activity and poleward TID activity during main and recovery phases of a geomagnetic storm. The datasets have further been divided between LSTID and MSTID activities, for both northern and southern hemispheres. The cyan bars are the Southern Hemisphere LSTID activity. The blue bars with cross hatch are the Southern Hemisphere MSTID activity. The yellow bars represent activity in the LSTID of the Northern Hemisphere. The green bars with cross hatch represent Northern Hemisphere MSTID activity. Figure 5.5(a) shows that during the main phase, the Northern Hemisphere (NH) exhibits the largest activity of LSTIDs, with nearly 40 occurrences. Similar to the NH, the Southern Hemisphere (SH) also shows intensive LSTID activities but at a relatively lower level, around 30 events in total. That means the NH undergoes much more intensive and frequent large-scale disturbances during this phase. The MSTIDs are weak during the main phase over both hemispheres, less than 5 events in total. That means, large-scale disturbances are the dominant ones during the main phase of a geomagnetic storm.

As the storm evolves into the recovery phase, the TID activity decreases in general; however, hemispherical differences persist. The NH remains more active with LSTID activity, but it reduces to around 20 occurrences, whereas the SH LSTID activity decreases to about 15 occurrences. This decrease is indicative of large-scale disturbances weakening now that the storm is waning, while the NH retains a larger amount of this activity (Zhao, 2019; Guo, 2024). Notably, the activity of MSTID increases slightly in both hemispheres during the recovery phase, represented by a slight rise of events from the main phase. Figure 5.5 (b) shows that during main phase of the storm the poleward TID activity is minimal with all occurrences of TID activity below 5 thus making hemispheric differences hard to observe or contextualize. However, during the recovery phase, hemispheric difference in LSTID activity was observed, with the SH exhibiting nearly 12 LSTID activity, 10 more than the NH.

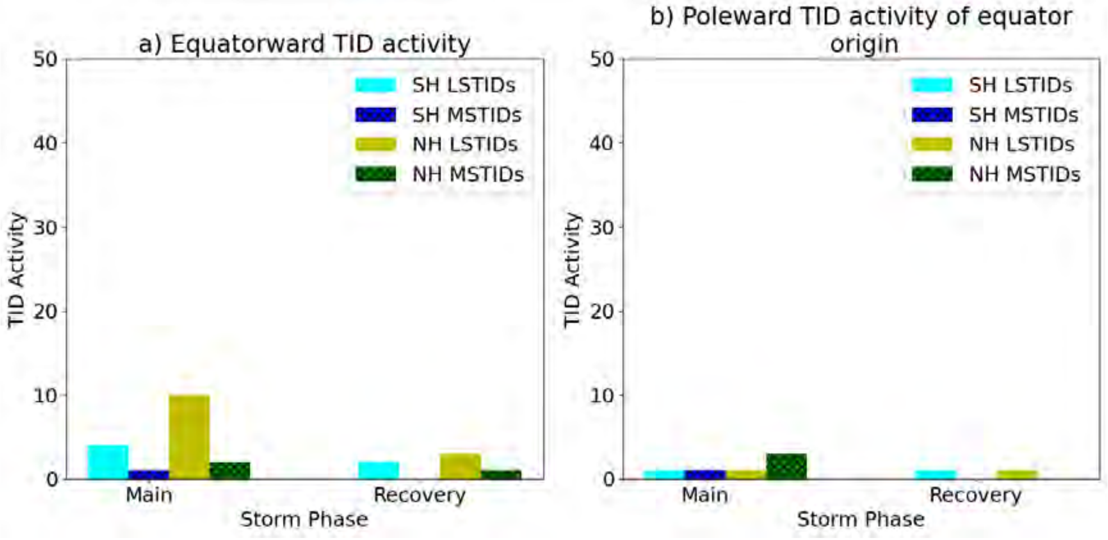

Figure 5.6: TID Activities, during simultaneous occurrence of geomagnetic storms and Solar flares between 2006-2022.

Figure 5.6 illustrates the activity of TIDs during the periods of simultaneous occurrence of geomagnetic storms and solar flares. Figure 5.6(a) focuses on the equatorward TID activity, while Figure 5.6(b) addresses the poleward TID activity originating from the equator. TID activity is examined for different storm phases and separately for the NH and SH and for LSTID activity and MSTID activity. In Figure 5.6(a) during the main storm phase, the NH shows the largest LSTID activity - about 10 events, while in the SH the activity is somewhat lower, about 4 events. MSTID activity is very low in both hemispheres during this phase. As the storm transitions to the recovery phase, LSTID activity significantly declines in both hemispheres, with the NH reporting about 3 events and the SH around 2 events. MSTID activity remains low but becomes more evenly distributed between the hemispheres. This decline in LSTID activity from the main to the recovery phase suggests that large-scale disturbances subside as the geomagnetic storm weakens (Zhao, 2019; Guo, 2024).

Figure 5.6(b), which addresses the poleward TID activity of equatorial origin, presents considerably lower activities in both phases of the storm compared to the equatorward TID activity. During the main phase, both LSTID and MSTID activities are minimal. Such a pattern may imply that poleward TID activity is less affected by the geomagnetic storm compared to the equatorward TID activity. During the recovery phase, poleward activity stays at a low level, with the slight activity seen in the SH main phase becoming almost invisible. Such consistency may again support that the poleward TIDs are less affected by the storm phases in terms of large-scale propagation.

This indicates that geomagnetic storms have a more pronounced effect on the equatorward TID activity than on the poleward TID activity of equatorial origin. The NH generally shows higher activity, especially during the main storm phase, which may indicate possible hemispheric asymmetry in the generation and propagation of TIDs (Hajkowicz, 1990; Cnossen and Förster, 2016; Förster and Cnossen, 2013; Laundal et al., 2016; Jonah et al, 2020; Wang et al, 2021). Jonah et al, (2020); noticed an imbalance in which TEC increased in the SH but decreased in the NH on two storm periods, 26–27 May 2017, and 24–25 August 2018. This finding suggests that equatorial plasma fountain effects must be accompanied by considerable changes in thermospheric composition and/or accompanying thermospheric neutral wind circulation. Furthermore, in both storm periods provided here, the NH denotes the summer hemisphere and the SH denotes the winter hemisphere. As a result, normal quiet conditions should yield plasma density levels that are greater in the summer hemisphere at low latitudes. Equatorward LSTID activity are dominant during storms, while poleward TID activity remains minimal.

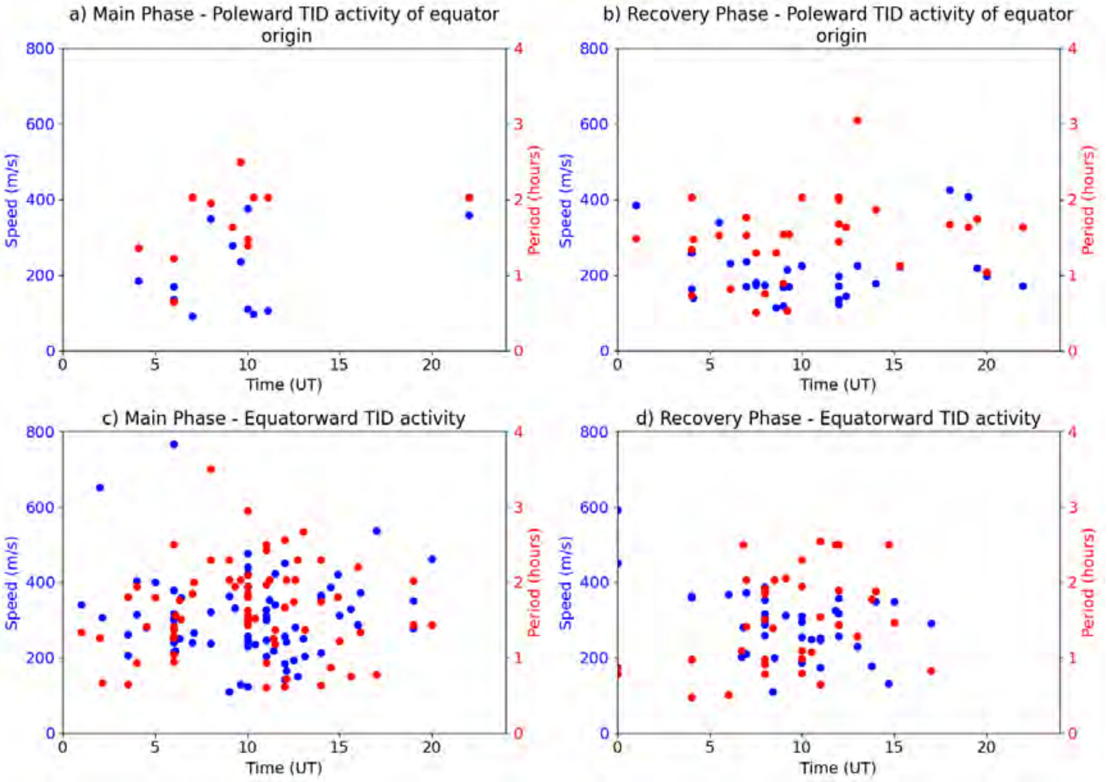

Figure 5.7: Results of velocity and period analysis of TIDs during main and recovery phases of geomagnetic storms.

Figure 5.7 shows the variation with Time (UT) of the relation between Speed (m/s) and Period (hours) for the TID activity during the respective Main and Recovery phases, distinguishing between poleward and equatorward. The poleward TID activity during the main phase, Figure 5.7(a), varies in speed (blue dots) considerably, including recorded data points as high as 400 m/s, but the periods (red dots) are mainly concentrated within the range of 1 to 2 hours. Data points that are distributed rather sparsely indicate increased variability in the disturbances observed during this phase. In Figure 5.7(b) shows poleward TID activity during recovery phase, the speed range is focused at 200 to 600 m/s, with periods consistent at 1 to 2 hours, and data points are uniformly distributed throughout the day, indicating continued activity in the TID.

In contrast, equatorward TID activity during the main phase, in Figure 5.7(c), shows more scattered data points, indicating a higher occurrence rate or stronger TID activity. The velocities have a wider spread, with more values reaching as high as 800 m/s and the periods are centered between 1 to 3 hours. The velocity distribution during the recovery phase of the equatorward activity, as shown in Figure 5.7(d) bears some resemblance to that in poleward recovery, but there is a marginal concentration within the range 200-400 m/s. The dominant durations remain around 1-2 hours with sparser dispersion compared to the Main Phase.

On the whole, it can be seen that the Main Phase shows more variability in both speed and period, being more dynamic and intensive TID activity, while during the Recovery Phase this activity becomes more focused and stable. The equatorward TID activity, especially in the Main Phase, attains higher speed and more frequent appearance; hence, stronger disturbances could be inferred in this direction.

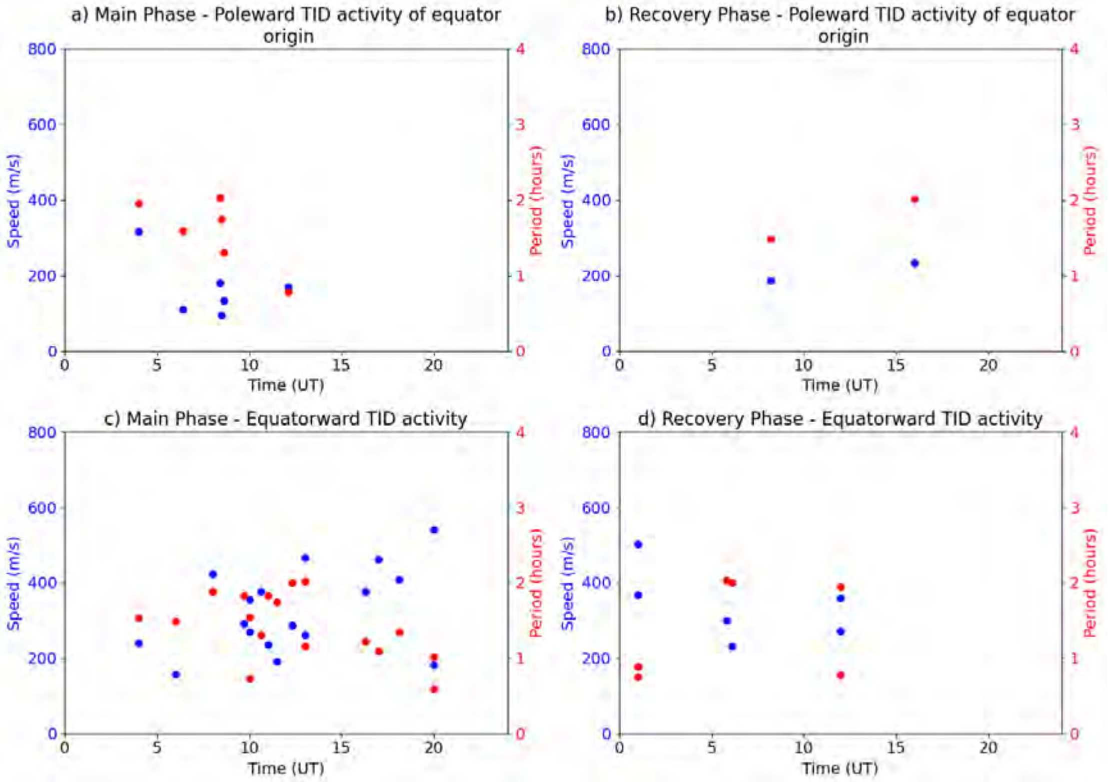

Figure 5.8: Results of the analysis of TIDs during main and recovery phases of geomagnetic storms and solar flares.

Figure 5.8 shows four scatter plots of Speed (m/s) and Period (hours) against Time (UT) for poleward and equatorward TID activities during the main and recovery phases. Each plot has a dual y-axis, where speed is plotted in blue on the left axis and period is in red on the right axis. In Figure 5.8(a), corresponding to the main phase of poleward TID activity, the predominant speeds are between 200 and 400 m/s for periods of approximately 1 to 2 hours. Figure 5.8(b) represents the recovery phase of poleward TID activity, where events were fewer in number. Figure 5.8(c), the main phase of equatorward TID activity, has much more scattered and frequent data points, with speeds ranging from 200 to 600 m/s and periods between 0 to 4 hours. Figure 5.8(d) which shows the recovery phase of equatorward TID activity, reflects fewer events with velocities in the range of 200-400 m/s and periods of about 1 to 2 hours. Overall, during the main phase, there is stronger and more frequent TID activities in general, especially those equatorward, while the recovery phase has subdued activities.

Habarulema et al. (2022) reported that throughout the main phase of geomagnetic storms, nearly all poleward TIDs were large scale with velocities ranging from 300-550 m/s, following the period range classification of 30 min to 3 hr (e.g., Hunsucker, 1982; Kersley and Hughes, 1989). Habarulema et al. (2022) also reported that during recovery phase, MSTIDs had period and velocity values ranging from 23-50 min and 190-290 m/s, respectively, while the corresponding values for LSTIDs were 30 min -1.5 hr and 300-410 m/s.

5.3 Diurnal Variation of TID Activity

Cheng et al. (2021) developed an autonomous algorithm that uses both the 3 dimensional Fast Fourier Transform (3-D FFT) and Support Vector Machines (SVM) to statistically study the MSTIDs in the low-latitude equatorial ionization anomaly region over Taiwan from 2013 to 2015. The statistical results demonstrate that the seasonal, local time (LT) changes of TEC perturbations in low latitude across Taiwan are broadly consistent with earlier MSTID investigations (Otsuka, 2021). MSTID occurrence rates and propagation directions are clearly seasonal and time dependent. MSTIDs moving southward are seen virtually every day between 0800-2100 LT in the spring and winter, primarily around 2100-0300 LT in the summer, and with the least occurrence in the autumn. From Spring to Autumn, however, northward MSTIDs are more typically recorded around 1200-2100 LT, with a secondary peak around 0000-0300 LT. There are little studies done on the diurnal variation of LSTIDs. Song et al. (2013), performed a statistical study of LSTIDs formed by the solar terminator over China, focused on the dusk and dawn local time. Tsugawa et al. (2004) did a statistical study of LSTIDs utilizing the GPS network in Japan, and shown that there are more LSTID in the local nighttime than the local daytime.

5.3.1 Results during geomagnetic storms

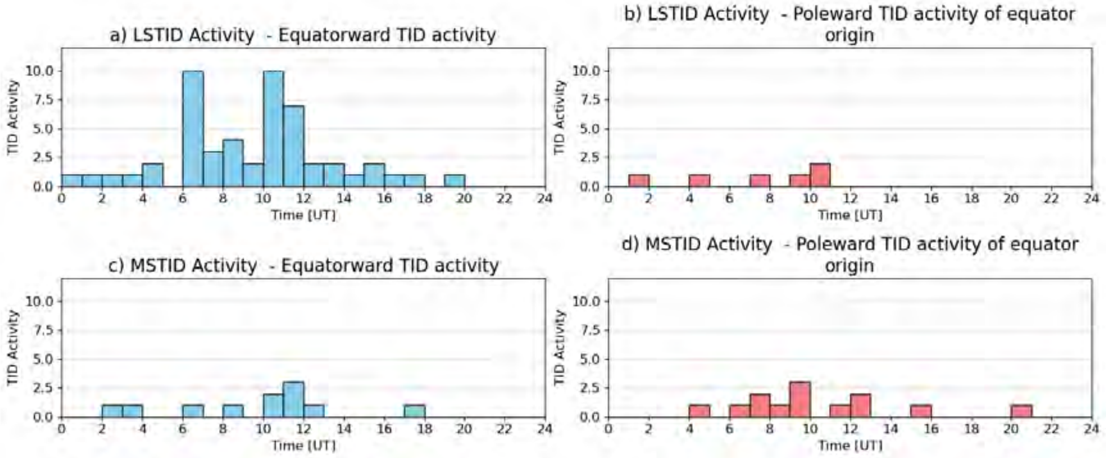

Figure 5.9: Diurnal Variation of TID Activity in the Northen Hemisphere during Geomagnetic storms between 2006-2022.

Figure 5.9 provides statistical distribution of TID activity for both LSTID activity and MSTID activity for geomagnetic storms in the Northern Hemisphere. The Time [UT] in the x axis, which is defined as the estimated start of TID activity, are obtained from the average of the start of TIDs observed. The activities are further categorized into equatorward and poleward activities.
In Figure 5.9(a), equatorward LSTID activity is most prominent between 6 UT and 12 UT, peaking at about 6-7 UT and 10-11 UT, this activity was much stronger compared to all the other categories during peak hours, while tapering off in the afternoon and turning negligible in the evening. On the contrary, to the equatorward LSTID activity, in Figure 5.9(b) the poleward LSTID activity originating from the equator is minimal with little activities around 2 UT, 4 UT, 8 UT, and 10 UT.

The poleward MSTID activity in Figure 5.9d) shows small peaks around 8-10 UT and another minor peak at 12 UT. MSTID activity is not as strong as it is for the equatorward LSTID activity. There are very few poleward TID activity of equator origin. From Figure 5.9 it can be concluded that equatorward LSTID activity is more dominant during geomagnetic storms.

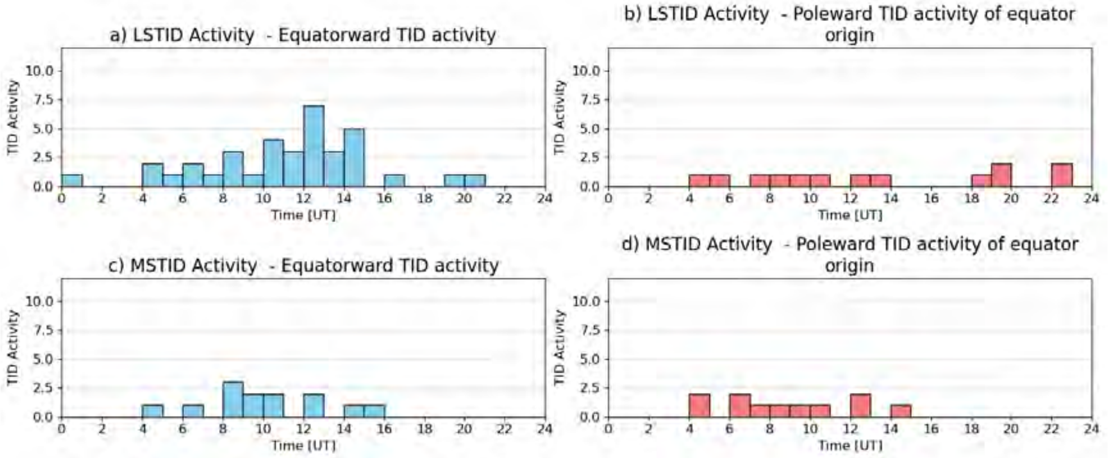

Figure 5.10: Diurnal Variation of TID Activity in the Southern Hemisphere during Geomagnetic storms between 2006-2022.

Figure 5.10 is similar to Figure 5.9, but in the southern hemisphere. In Figure 5.10(a) The peak of equatorward LSTID activity lies between 10 and 14 UT. By contrast, in Figure 5.10(b) the poleward LSTID activity is small throughout the day. This poleward propagation activity is, however, relatively low, with less notable clustering. In Figure 5.10(c) the equatorward MSTID activity does not show clear peaks, having only minor peaks around 8 UT and 12 UT, which indicate some level of TID activity in the morning and midday hours, even though these are much weaker than the equatorward LSTID activity.

Similarly, in Figure 5.10(d) the poleward MSTID activity is sparse and stretched over the day, with minor occurrences at around 6 UT and 12 UT, but remain low. During geomagnetic storms, TID activity in the Southern Hemisphere is distinctly different from that in the Northern Hemisphere. The equatorward TID activity maximum occurs later in the day between 10 and 14 UT. On the whole, from the overall pattern, it is observed that TIDs tend to propagate equatorward during both storm phases while poleward propagation remains a rather rare activity. The study is done during geomagnetic storms and it is well known that high solar activity periods exhibit higher occurrences of geomagnetic storms. Furthermore, equatorward LSTIDs are launched from high latitudes during geomagnetic storms. TIDs during geomagnetic storms are usually associated with solar wind-magnetosphere-ionosphere coupling, which leads to a surge in the generation of AGWs in auroral/high-latitude regions as a result of enhanced Lorentz coupling, Joule heating, and particle precipitation (e.g., Hunsucker, 1982; Hajkowicz and Hunsucker, 1987; Hocke and Schlegel, 1996; Balthazor and Moffett, 1997; Bruinsma and Forbes, 2009). LSTIDs exhibit a dominant equatorward direction from both the northern and southern hemispheres. During geomagnetic storms, equatorward LSTIDs are also launched from high latitudes (Habarulema et al., 2022).

5.3.2 Results during simultaneous occurrence of geomagnetic storms and solar flares

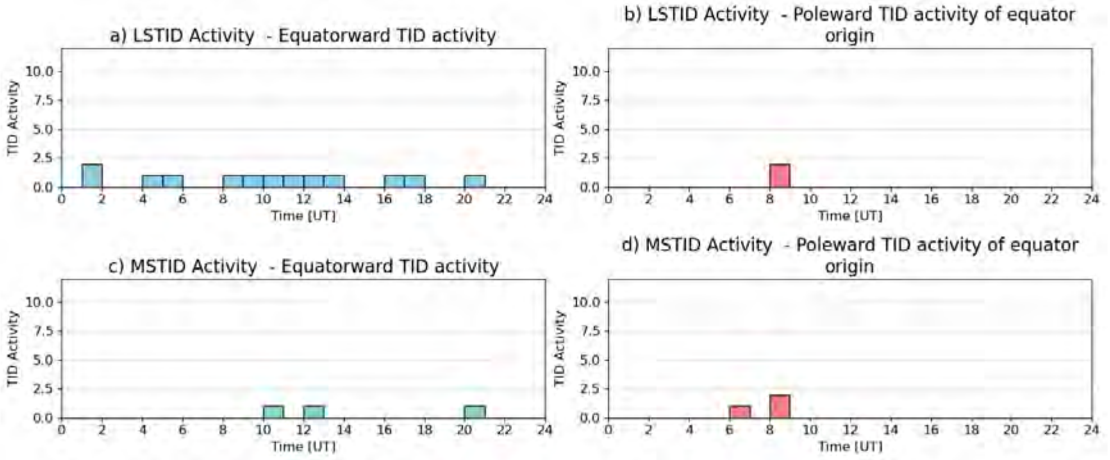

Figure 5.11: Diurnal Variation of TID Activity in the Northern Hemisphere during simultaneous occurrence of Geomagnetic storms and Solar Flares between 2006-2022.

Figure 5.11 displays the distribution of both LSTID and MSTID activities for simultaneous occurrences of storm and solar flares in the Northern Hemisphere. The activities are further categorized into equatorward and poleward activities.

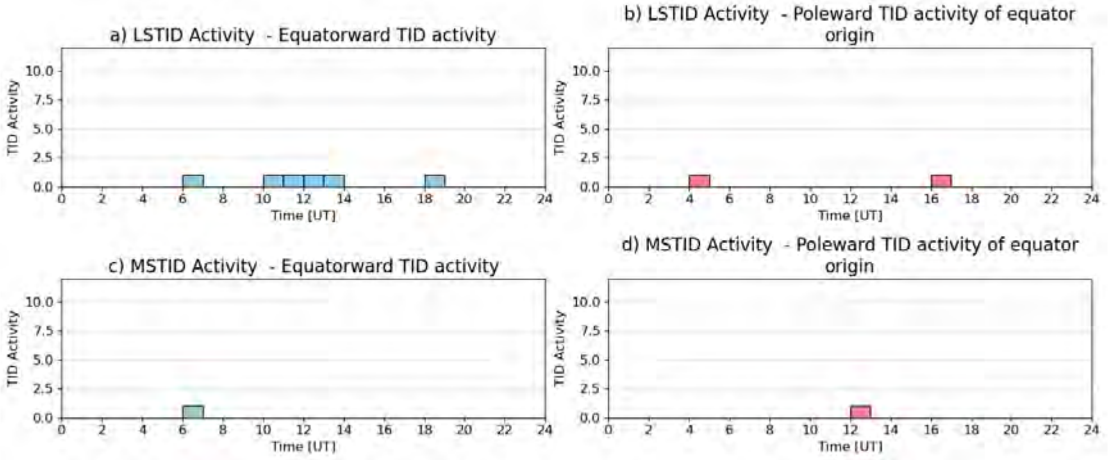

Figure 5.12: Diurnal Variation of TID Activity in the Southern Hemisphere during simultaneous occurrence of Geomagnetic storms and Solar Flares between 2006-2022.

Figure 5.12 is similar to Figure 5.11, but for the southern hemisphere. Results in both hemispheres agree with low occurrences of TID activity during the simultaneous occurrence of geomagnetic storms and solar flares.

5.4 Seasonal Variation of TID Activity

Several studies have focused on the characteristics of seasonal variations in AGW and TID activity (Garcia et al., 2000; Shiokawa et al., 2003; Hernandez-Pajares et al., 2006; Kotake et al., 2006; Grocott et al., 2013). Recent research has found that TID activity varies annually, with a winter peak throughout the North American sector and a significant reduction during the summer (Frissell et al., 2014; Frissell et al., 2016) for both quiet and disturbed conditions.

According to Ogawa (1988), their 10 month statistical study showed that TID activity is highest in August (SH winter) and lowest in January (SH summer). This observation is also partially compatible with that of Evans et al. (1983), who noted that the seasonal variation is less obvious, although the occurrence appears to be enhanced in winter and around the equinoxes and decreased in summer. They explained the seasonal change by pointing out that detectability is dependent on total electron content. That is, the detectability of an acoustic gravity wave is determined by the ambient ionization density (foF_2), and some techniques may fail to detect it if the ambient ionization density is less than a certain threshold value.

Shiokawa et al. (2003) found a semi-annual change in TID activity across Japan at similar latitudes, however the airglow all-sky imager only detected nocturnal TIDs. Kotake et al. (2006) discovered a similar trend over the Eastern North American continent using Global Positioning System total electron content data, while Negrea et al. (2018) found a substantially bigger amplitude for this semi-annual variation in TID activity.

5.4.1 Seasonal Variation results during geomagnetic storms

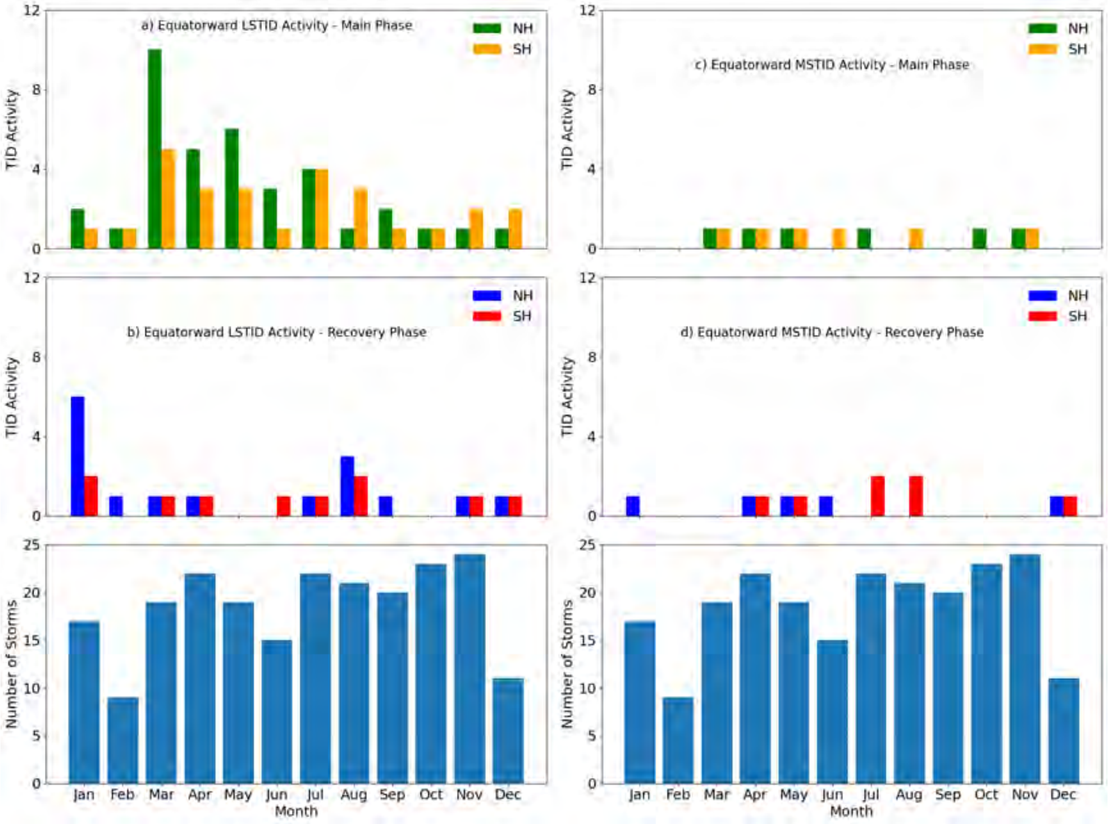

Figure 5.13: Seasonal Variation of equatorward TID Activity during Geomagnetic storms between 2006-2022.

Figure 5.13 shows the seasonal distribution of TID activity during geomagnetic storms which occurred from 2006-2022 for the main and recovery phases. In Figure 5.13(a) and (c), the green and yellow colors represent TID activities for the NH and SH, respectively during main phase. In Figure 5.13(b) and (d), the blue and red colors represent TID activities for the NH and SH, respectively during recovery phase. The bottom row of plots shows the seasonal distribution of storms, reflecting a distinct peak in storm occurrences in October-November, while during spring in SH and early summer in SH months, the count of storms was low. Figure 5.13(a) and (c) depict that during the main phase, the equatorward LSTID activity is stronger in the NH than that in the SH around March, April, and May. This indicates a hemispheric asymmetry in ionospheric disturbances where equatorward LSTID events occur more frequently in the NH (Hajkowicz, 1990; Förster and Cnossen, 2013; Cnossen and Förster, 2016; Laundal et al., 2016; Jonah et al, 2020; Wang et al, 2021). During the recovery phase, equatorward LSTID activity is reduced; however, the NH still presents higher activity than the SH.

On the other hand, in Figure 5.13(b) and (d) the equatorward MSTID activity is small through both the main and recovery phases, having a slight increase during the latter, in the SH in July and August. Figure 5.13 underlines the complicated interaction between the storm phases, hemispheric differences, and seasonal variations of equatorward TID activity. Equatorward LSTID activity is more frequent and stronger in the NH, and its seasonal peak coincides with storm occurrences. The NH generally shows higher activity, especially during the main storm phase, which may indicate possible hemispheric asymmetry in the generation and propagation of TIDs (Hajkowicz, 1990; Förster and Cnossen, 2013; Cnossen and Förster, 2016; Laundal et al., 2016; Jonah et al, 2020; Wang et al, 2021).

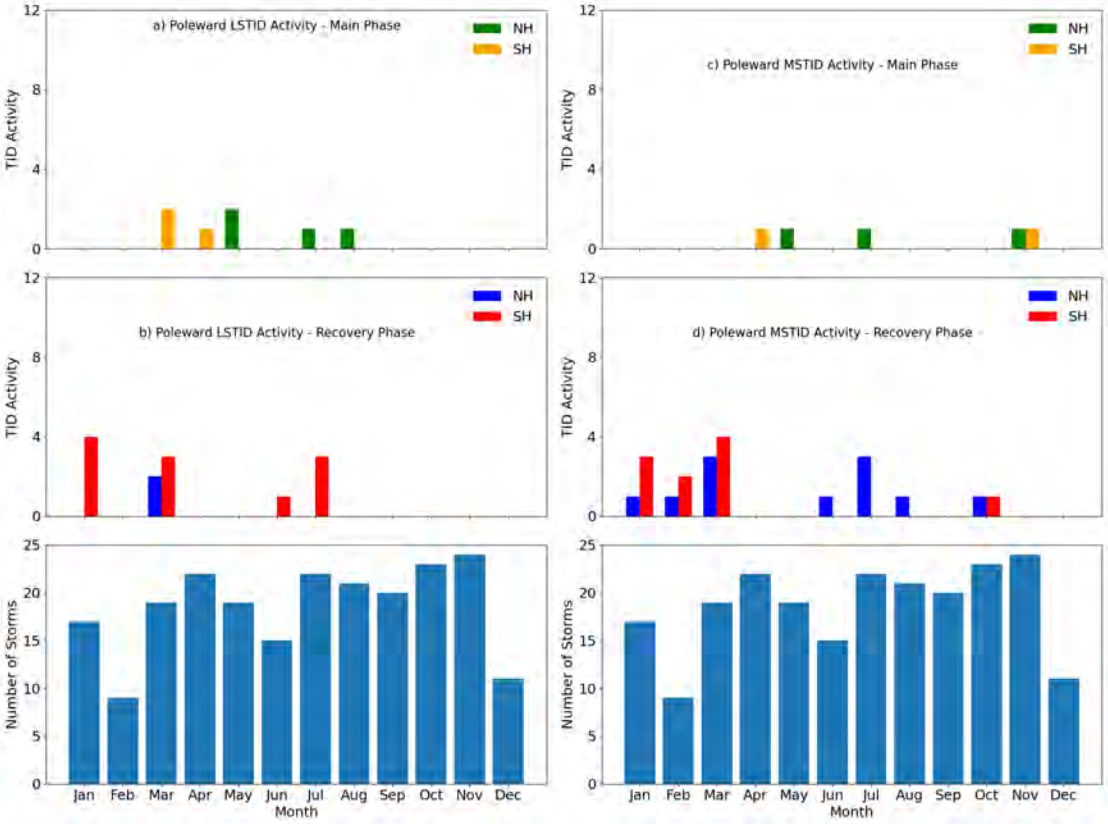

Figure 5.14: Seasonal Variation of poleward TID Activity during Geomagnetic storms between 2006-2022)

Figure 5.14 shows the seasonal distribution of poleward TID activity during geomagnetic storms which occurred from 2006-2022 for the main and recovery phases. In Figure 5.14(a) and (c), the green and yellow colours represent TID activities for the NH and SH, respectively during main phase. In Figure 5.14(b) and (d), the blue and red colours represent TID activities for the NH and SH, respectively during recovery phase. During the main phase of storms, poleward LSTID activity is relatively low in both hemispheres, the SH being slightly more active, especially during the months, of March and May. In turn, the scarce occurrence of poleward LSTID activity is distributed around June in the NH. The poleward LSTID activity is certainly more salient in the recovery phase.

Similarly, poleward MSTID activity is minimal during the main phase. During the recovery phase, however, MSTID activity significantly develops in both hemispheres. This agrees with the above-described pattern for poleward LSTID activity, where the recovery phase appears to favor the generation of poleward TIDs. Equatorward

TIDs are frequently associated with geomagnetic storm conditions. These storms inject energy into the auroral regions, causing gravity waves to spread equatorward (Habarulema et al, 2016; Jonah et al, 2017). This process occurs more frequently because geomagnetic storms are relatively widespread and have a substantial impact on the ionosphere. Poleward TIDs, on the other hand, are linked to different sources including local atmospheric gravity wave sources, such as convection activities (Jonah et al, 2017). Furthermore, the mechanisms that drive poleward TIDs are more limited and less likely to cause large-scale disturbance.

5.4.2 Seasonal Variation results during simultaneous occurrence of geomagnetic storms and solar flares

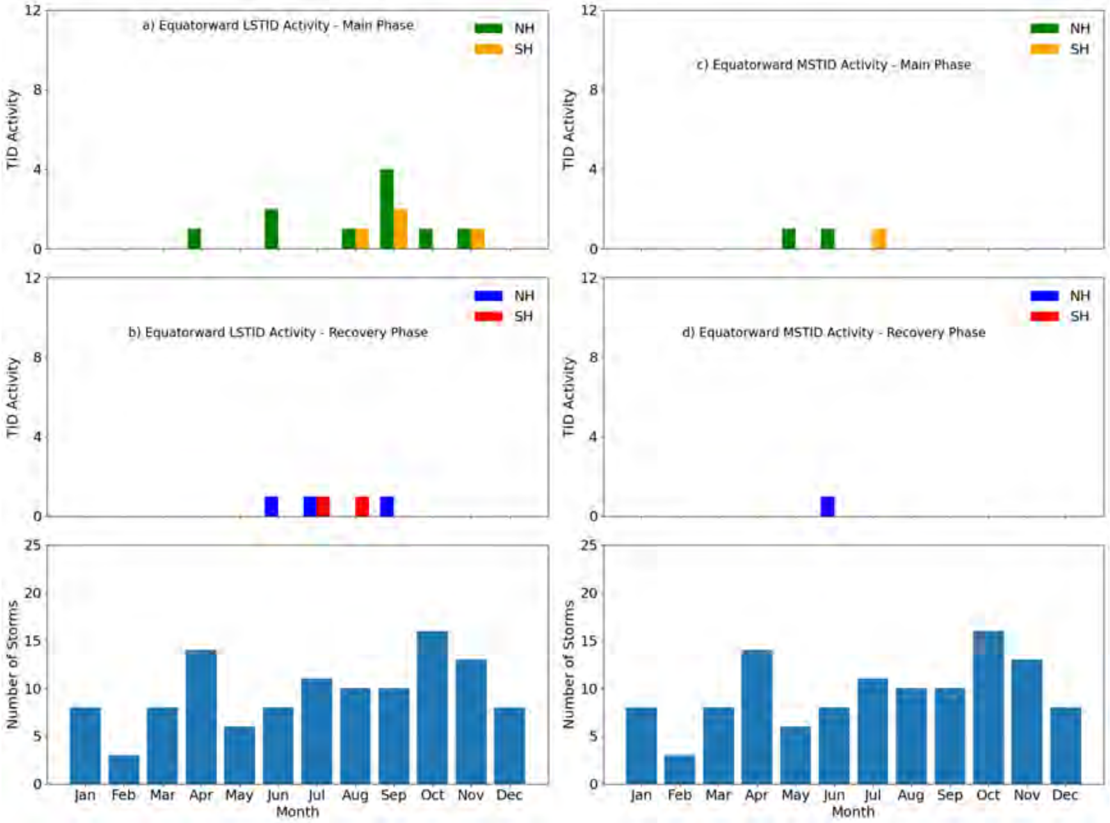

Figure 5.15: Seasonal Variation of equatorward TID Activity during simultaneous occurrence of Geomagnetic storms and solar flares between 2006-2022.

Figure 5.15 shows the seasonal distribution of TID activity during simultaneous occurrences of storm and solar flares which occurred from 2006-2022 for the main and recovery phases. In Figure 5.15(a) and (c), the green and yellow colours represent TID activities for the NH and SH, respectively during main phase. In Figure 5.15(b) and (d), the blue and red colours represent TID activities for the NH and SH, respectively during recovery phase. The seasonal distribution of geomagnetic storms with respect to months is provided in the bottom row.

During the main phase, prominent LSTID activities in the NH are mainly observed during April, June, and September. The number of events is the highest in

September. In the SH, the number of events is low, main activities have been observed during August, September and November. During the recovery phase, the LSTID activity reduced significantly, showing only a few events in July, August, September, October and November. It is interesting to note that during this recovery phase the activities of NH and SH are quite balanced.

In Figure 5.15(b) MSTID activity occured only on a few instances, concentrated in May and June for the NH and in July for the SH. In figure 5.15(d) during the recovery phase, MSTID activity becomes very scarce, having only one event in the NH in June. (Habarulema et al., 2022) showed that during main phase of geomagnetic storms poleward TIDs are mostly large scale and during recovery phase, poleward TIDs were dominantly medium scale.

Figure 5.15 shows that LSTIDs have larger occurrences than MSTIDs, and that there is more TID activity during the main phase than during the recovery phase of storms. Also, the hemispheric asymmetry in the occurrence of TIDs may be seen to exist, with more in the NH, especially around the main phase. The NH generally shows higher activity, especially during the main storm phase, which may indicate possible hemispheric asymmetry in the generation and propagation of TIDs (Hajkowicz, 1990; Förster and Cnossen, 2013; Cnossen and Förster, 2016; Laundal et al., 2016; Jonah et al, 2020; Wang et al, 2021). Additionally, the seasonal distribution of storms could suggest that some specific periods of the year, especially around the equinoxes, may be more favorable for storm activity and the eventual occurrence of TIDs, as Cheng et al. (2021) suggested.

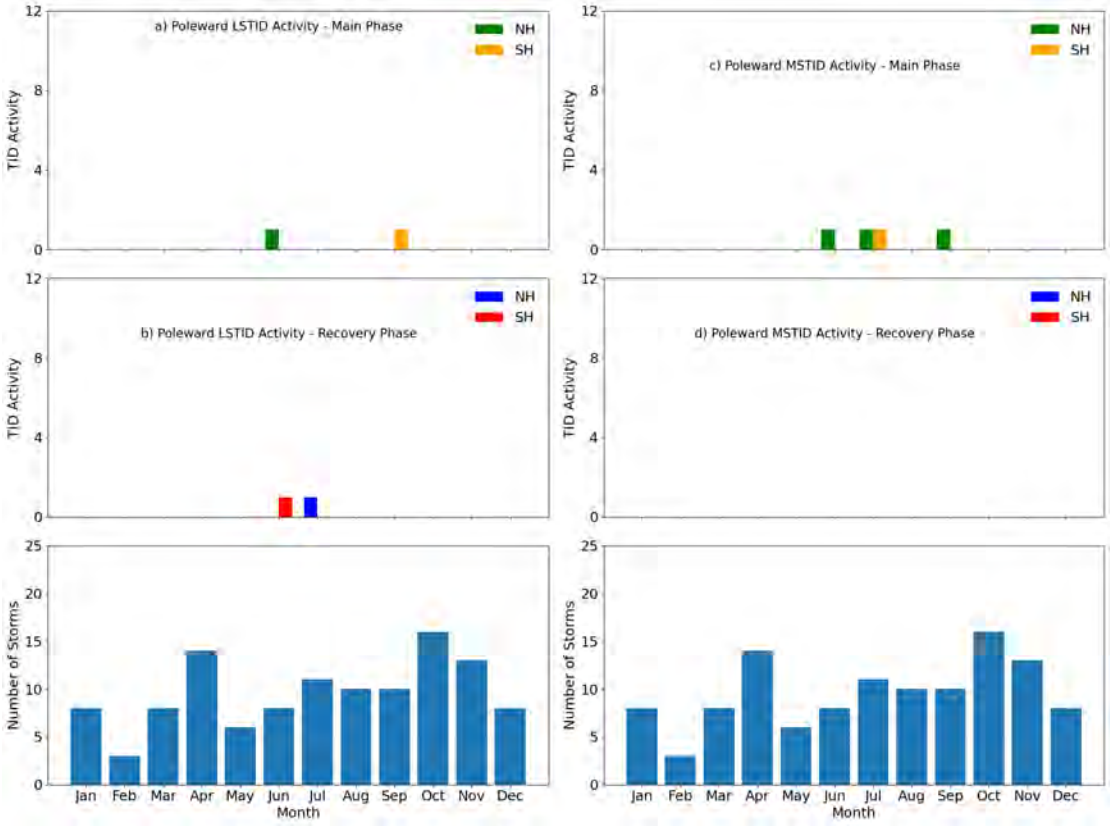

Figure 5.16: Seasonal Variation of poleward TID Activity during simultaneous occurrence of Geomagnetic storms and solar flares between 2006-2022.

Figure 5.16 shows the seasonal distribution of poleward TID activity during simultaneous occurrences of storm and solar flares which occurred from 2006-2022 for the main and recovery phases. In Figure 5.16(a) and (c), the green and yellow colours represent poleward TID activities for the NH and SH, respectively during main phase. In Figure 5.16(b), the blue and red colours represent poleward TID activities for the NH and SH, respectively during recovery phase.

Figure 5.16(a) and (c), shows poleward TID activity, revealing little poleward TID activity during the main phase, with peaks in specific months June, July and September.

In Figure 5.16(b) and (d), the poleward MSTID activity, on the other hand, is minimal during the main phase, none was observed during the recovery phase. The data in Figure 5.16 is very small to truly draw a definative conclusion thus making it hard to analyse.

5.5 Annual Variation of TID Activity

Medvedev et al. (2013) have shown that wave activity (the number of wave-like disturbances) in the ionosphere increases with both solar and geomagnetic activity in a study that was done in the period 2003-2012 (Ratovsky et al., 2015).

5.5.1 Annual Variation results during geomagnetic storms

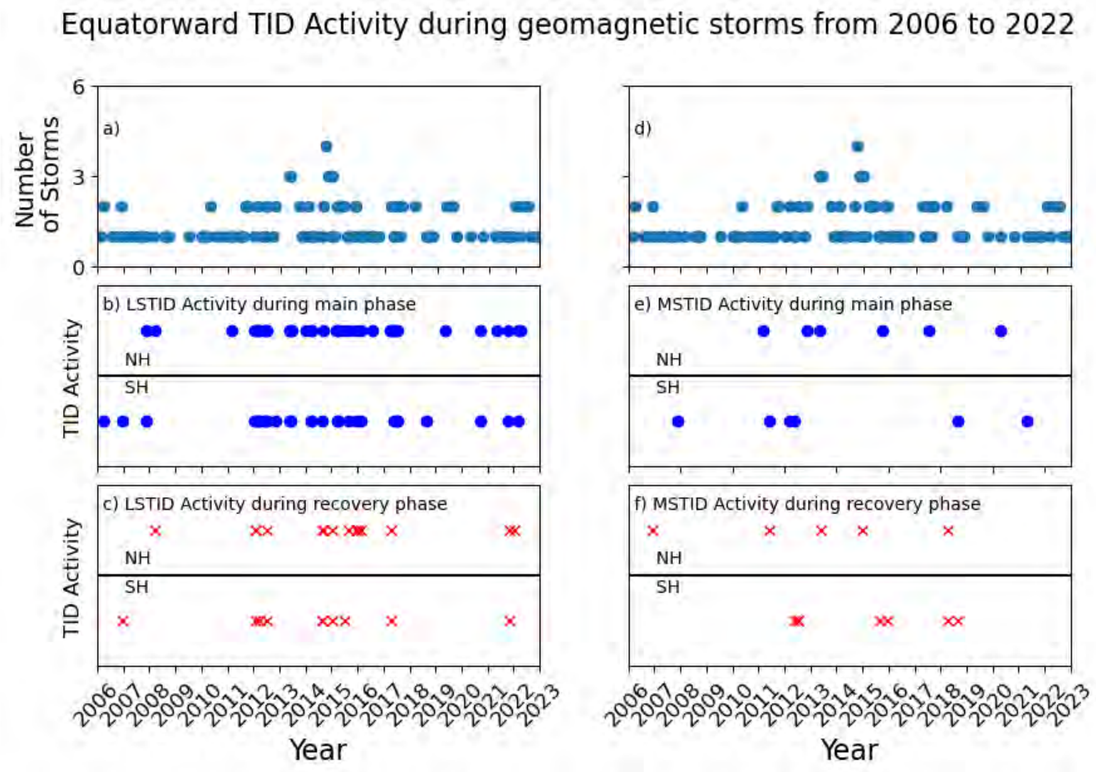

Figure 5.17: Annual Variation of equatorward TID Activity during geomagnetic storms.

Figure 5.17 presents an in-depth analysis of equatorward TID activity during geomagnetic storms from 2006 to 2022. The analysis is divided into six panels, each focusing on different aspects of TID activity across storm phases and hemispheres.

Figures 5.17 (a) and (d) are similar and depict the number of geomagnetic storms between 2006 to 2022, with both showing fluctuations in storm counts over time. The storm occurrence is indicated at exactly the time, month and year when the storms occurred explaining why some dots are very close to each other. Notable peaks are observed between 2012 and 2017, which may correlate with periods of higher solar activity, where geomagnetic storms are typically more frequent. This trend underscores the influence of the solar cycle on geomagnetic activity (Legrand et al, 1989; Papitashvili et al, 2000; Georgieva et al, 2011). Figures 5.17(b)-(c) and (d)-(e) are presented in a format where TID activity occurrences are split into NH and SH, respectively, for comparative purposes. For-example, in Figure 5.17(b), there is an observation of a LSTID activity in the SH in 2006 which is absent in the NH during the same geomagnetic storm main phase.

Figure 5.17 (b) and (e) focus on TID activity during the main phase of storms. LSTID activity, shown in Figure 5.17(b), is relatively consistent across both hemispheres, with some years, like 2013 and 2015, showing higher frequencies of events. MSTID activity, presented in Figure 5.17(e), appears less frequent overall, suggesting that LSTIDs are more prominent during the main phase of geomagnetic storms.

In contrast, Figures 5.17(c) and (f) illustrate TID activity during the recovery phase. Both LSTID and MSTID activities are less frequent during this phase compared to the main phase. The activity is more concentrated in specific years and hemispheres, with the NH generally showing more events. The analysis highlights notable hemispheric differences, with the NH often exhibiting more TID activity (Hajkowicz, 1990; Cnossen and Förster, 2016; Förster and Cnossen, 2013; Laundal et al., 2016; Jonah et al, 2020; Wang et al, 2021). The data also reveal that TID occurrences vary significantly over time, likely influenced by solar cycles, and that TID activity is generally stronger during the main phase of storms (Bowman, 2001; Klausner et al, 2009).

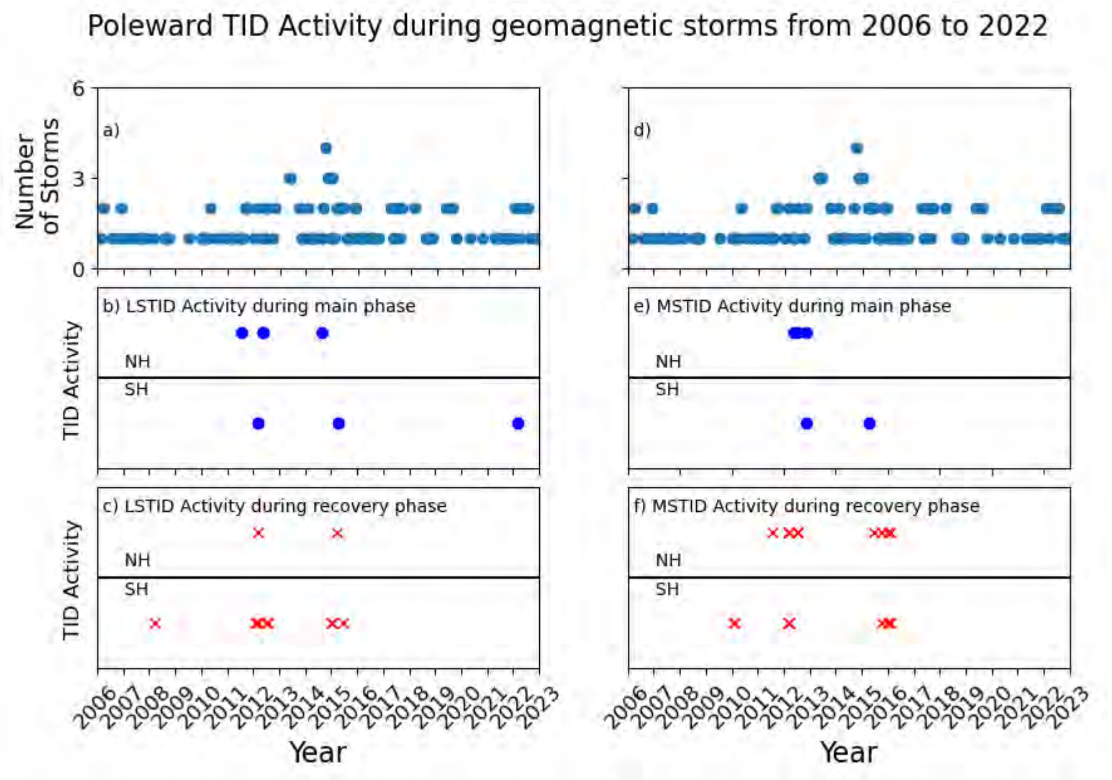

Figure 5.18: Annual Variation of poleward TID Activity during geomagnetic storms.

Figure 5.18 is similar to Figure 5.17, but for the poleward TID activity during the geomagnetic storms from 2006 to 2022. There are significant peaks in Figure 5.18(a) and (d) in the years 2012-2015, hence coinciding with the solar maximum of Solar Cycle 24. In this period of high solar activity, there are more storm events, which are indeed known to drive TID activity.

Figure 5.18 (b) and (c) shows LSTID activity during main phase and recovery phase, respectively, with the occurrence of a couple of events in 2013-2015. MSTID activity, shown in Figure 5.18 (e) and (f), tend to have more sporadic activity during both storm phases, with activity clusters around 2014 and 2017. A hemispheric asymmetry is also evident in the data: SH dominates slightly for LSTID activity. This difference could be because of hemispheric differences which cause different effects in the different hemispheres in the geomagnetic conditions (Hajkowicz, 1990; Förster and Cnossen, 2013; Cnossen and Förster, 2016; Laundal et al., 2016; Jonah et al, 2020; Wang et al, 2021). The NH has fewer events during some periods. Habarulema et al. (2022) showed that during main phase of geomagnetic storms poleward TIDs are mostly large scale, while the recovery phase was dominantly medium scale.

5.5.2 Annual Variation results during simultaneous occurrence of geomagnetic storms and solar flares

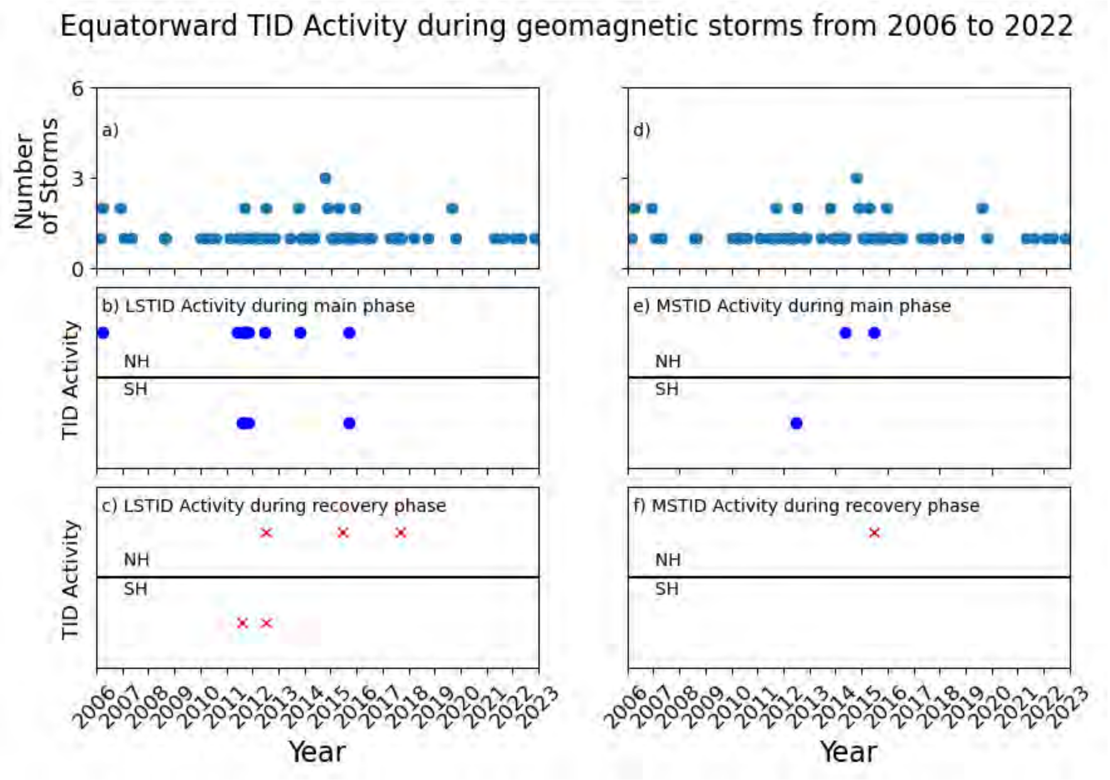

Figure 5.19: Annual Variation of equatorward TID Activity during simultaneous occurrence of geomagnetic storms and solar flares.

Figures 5.19 (a) and (d) are similar and depict the number of geomagnetic storms between 2006 to 2022. Figures 5.19 (b) and (c) depict equatorward LSTID activity during the main and recovery phases of these geomagnetic storms. During the main phase, indicated in Figure 5.19 (b), there is a notable presence of equatorward TID activity in both hemispheres, with years such as 2012 and 2015 showing significant occurrences. Conversely, Figure 5.19 (c) examines equatorward LSTID activity during the recovery phase, where the data reveals fewer events, with more activity observed in the NH compared to the SH.

Figures 5.19(e) and (f) show equatorward MSTID activity, during the main and recovery phases of geomagnetic storms. The main phase, shown in Figure 5.19 (e), reveals instances of equatorward MSTID activity, particularly in 2015, across both hemispheres. However, during the recovery phase, depicted in Figure 5.19 (f), equatorward MSTID activity is minimal, with only one occurrence, in the NH.

Figure 5.19 demonstrates a clear distinction between equatorward TID activity during the main and recovery phases of geomagnetic storms. The main phase consistently shows more equatorward TID occurrences, while the recovery phase exhibits fewer events, particularly in the SH. The data also highlights annual variations, with specific years like 2012 and 2015 experiencing heightened equatorward TID activity, suggesting these years had more significant geomagnetic disturbances and solar flares as it was around the solar maximum, thereby impacting the ionosphere.

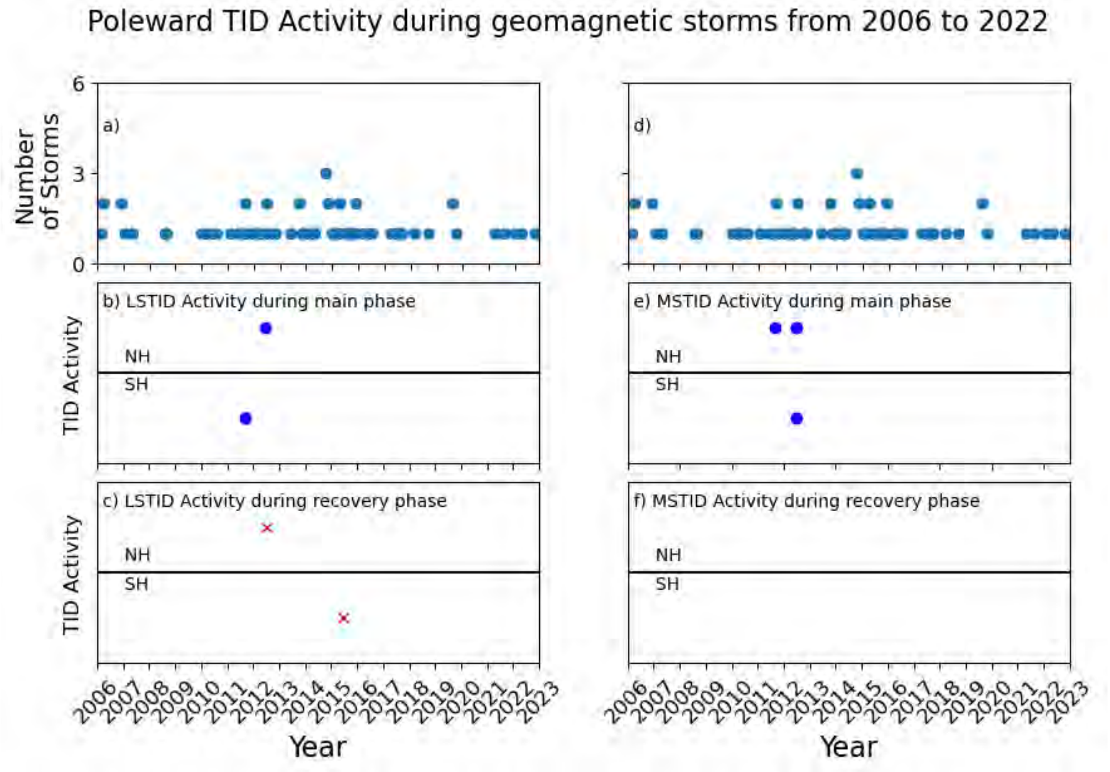

Figure 5.20: Annual Variation of poleward TID Activity during simultaneous occurrence of geomagnetic storms and solar flares.

Figure 5.20 is similar to Figure 5.19, but for poleward TID activity results during simultaneous occurrence of geomagnetic storms and solar flares. There are generally fewer cases of TID activity occurrence during both main and recovery phases.

5.6 Summary

This chapter discussed the statistical analysis of observations of poleward TID activity of equatorial origin and equatorward TID activity over the African-European sector during geomagnetic storms and simultaneous occurrences of geomagnetic storms and solar flares between 2006 and 2022. Geomagnetic storms were determined by Dst $\leq$ -30 nT. TIDs were discovered in GNSS TEC-derived data. The years with peak storm activity do fall within Solar Cycle 24 when most of the TID events occurred, and these disturbances may be closely related to solar conditions and those involving geomagnetic activity. LSTIDs exhibit a dominant equatorward direction from both the northern and southern hemispheres. In both hemispheres, it appears that the LSTIDs are dominant during storms, with time of occurrence around 10-12 UT.

Chapter 6: Conclusions and Future Work

The main goal of this study was to conduct a statistical analysis of equatorward TID activities and poleward TID activities of equator origin over the African-European sector between 2006 and 2022 during geomagnetic storms and simultaneous occurrence of geomagnetic storms and solar flares. Geomagnetically disturbed conditions were identified based on Dst < -30 nT. Global Navigation Satellite Systems (GNSS) data were used to identify TID activity.

The method presented detected 196 TID activities propagating over the African-European sector within the longitudinal range of 20–40° E during the period from 2006 to 2022. Of these TID activities, 161 and 33 were observed during geomagnetic storms, and simultaneous occurrence of geomagnetic storms and solar flares, respectively. The present research examined both equatorward medium- to large-scale TID activity and poleward medium- to large- scale TID activity originating from the equator in the southern and northern hemispheres. In this project equatorward TIDs are TID originating from higher latitudes towards the equator while poleward TIDs are the TIDs that are originating from the equator to the poles (Bowman and Mortimer, 2011; Habarulema et al., 2016; Habarulema et al., 2017; Thaganyana et al., 2022).

The poleward TID activity during the main phase had speeds as high as 400 m/s, with the periods mainly concentrated within the range of 1 to 2 hours. During recovery phase the poleward activity were observed to have speed of 200 to 600 m/s, with the periods consistent at 1 to 2 hours. Habarulema et al. (2022) found that poleward TIDs during the main phase of geomagnetic storms had speeds ranging from 300 to 550 m/s and period ranging from 0.5 to 2 hr. During the recovery phase, poleward MSTIDs with (period, speed) ranging from (23–50 min, 190–290 m/s) and poleward LSTIDs with (period, speed) ranging from (30 min–1.5 hr, 300–410 m/s). The poleward LSTID activity originating from the equator were minimal as compared to the equatorward LSTID activity. The poleward LSTID activity showed some sporadic activities around 2 UT, 8 UT, and 10 UT. The poleward MSTID activity originating from the equator was minimal and activity was most prominent between 6 UT and 14 UT in the northern hemisphere however in the southern hemisphere, the sporadic pattern is observed. Habarulema et al. (2022) found that poleward TIDs are observed between 0400–1530 UT. The poleward LSTID activity was certainly more salient in the recovery phase. During recovery phase in the SH, this activity was very high in months like March, April, and October, while there was also significant activity in the NH in months like February and November. Poleward MSTID activity was minimal during the main phase, particularly in the SH around March and September.

The equatorward TID activity during the main phase had speeds reaching as high as 800 m/s. The periods associated with these equatorward TID activities were centered between 1 to 3 hours. During the recovery phase, however, the speed of equatorward TID activity were distributed within the range 200-400 m/s, with the dominant periods ranging from around 1 to 3 hours. It was also found that the equatorward LSTID activity was most prominent between 6 UT and 16 UT in both hemispheres. The equatorward MSTID activity was most prominent between 8 UT and 14 UT in both hemispheres. During the main phase of the storm, the equatorward LSTID activity was more in the NH than in the SH around March, April, and May. The equatorward MSTID activity was small through both the main and recovery phases, having a slight increase during the latter, in the SH in July and August. (Sivakandan et al., 2021; Oluwadare et al., 2022) explained that the high GW activity is the cause of the high TID activity, as evidenced by the fact that the winter peak of the daytime TIDs and the winter peak in the amplitude of the meridional wind variations coincide. However, there is no rise in TID activity throughout the summer. This is due to the fact that GWs in the thermosphere propagate equatorward in the winter and poleward in the summer, and that GWs that propagate equatorward cause significant perturbations in plasma density in contrast to those that propagate poleward.

During the main phase of storms, equatorward LSTID activity was relatively consistent across both hemispheres, with years of solar maximum, between 2013 and 2015, showing higher frequencies of events. Equatorward MSTID activity appeared less frequent overall, particularly in the SH, suggesting that equatorward LSTID activity are more prominent during the main phase of geomagnetic storms. During the recovery phase, both equatorward LSTID and MSTID activities were less frequent compared to the main phase. Poleward MSTID activity tends to have more sporadic activity during both storm phases, with activity clusters around 2014 and 2017.

Future Work

The study was performed by visually identifying TIDs on the generated 2d TEC maps. It would be good to automate this process in order to make it faster and easier. It would also be good to study in detail more differences in the TID activities launched in both hemispheres and how the TID activities launched at solar minimum and solar maximum behaves and their characteristics.

References

Abdu, M., Sobral, J., Nelson, O. and Batista, I. 1985. Solar cycle related range type spread-F occurrence characteristics over equatorial and low latitude stations in brazil. Journal of Atmospheric and Terrestrial Physics, 47(8-10): 901–905. doi: https://doi.org/10.1016/0021- 9169(85)90065-0.

Afraimovich, E., Edemskiy, I., Voeykov, S., Yasyukevich, Y. V. and Zhivetiev, I. 2009a. The first GPS-TEC imaging of the space structure of MS wave packets excited by the solar terminator. Annales Geophysicae, 27(4): 1521–1525. doi: https://doi.org/10.5194/angeo27-1521-2009.

Afraimovich, E., Edemskiy, I., Voeykov, S., Yasyukevich, Y. V. and Zhivetiev, I. 2009b. Spatio-temporal structure of the wave packets generated by the solar terminator. Advances in Space Research, 44(7): 824–835. doi: https://doi.org/10.1016/j.asr.2009.05.017.

Afraimovich, E., Perevalova, N. and Voyeikov, S. 2003. Traveling wave packets of total electron content disturbances as deduced from global GPS network data. Journal of Atmospheric and Solar-Terrestrial Physics, 65(11-13): 1245–1262. doi: https://doi.org/10.1016/j.jastp.2003.08.007.

Afraimovich, E., Terekhov, A., Udodov, M. Y. and Fridman, S. 1992. Refraction distortions of transionospheric radio signals caused by changes in a regular ionosphere and by travelling ionospheric disturbances. Journal of Atmospheric and Terrestrial Physics, 54(7-8): 1013– 1020. doi: https://doi.org/10.1016/0021-9169(92)90068-V.

Afraimovich, E., Voeykov, S., Perevalova, N. and Ratovsky, K. 2008. Large-scale traveling ionospheric disturbances of auroral origin according to the data of the GPS network and ionosondes. Advances in Space Research, 42(7): 1213–1217. doi: https://doi.org/10.1016/j.asr.2007.11.023.

Ahmed, M., Sagalyn, R., Wildman, P. and Burke, W. 1979. Topside ionospheric trough morphology: Occurrence frequency and diurnal, seasonal, and altitude variations. Journal of Geophysical Research: Space Physics, 84(A2): 489–498. doi: https://doi.org/10.1029/JA084iA02p00489.

Akasofu, S.-I. 1981. Energy coupling between the solar wind and the magnetosphere. Space Science Reviews, 28(2): 121–190.

Alonso, M., and Finn, E. J. 1969. Fundamental University

Physics Volume 1 Mechanics. *Addison-Wesley Publishing Company.* https://is.muni.cz/publication/269617

Amabayo, E.B., Edward, J., Cilliers, P.J. and Habarulema, J.B., 2014. Climatology of ionospheric scintillations and TEC trend over the Ugandan region. Advances in Space Research, 53(5), pp.734-743.

Anthes, R. A. 2011. Exploring Earth's atmosphere with radio occultation: Contributions to weather, climate and space weather. *Atmospheric Measurement Techniques*, *4*(6), 1077–1103. https://doi.org/10.5194/amt-4-1077-2011

Araujo-Pradere, E. 2005. GPS-derived total electron content response for the Bastille Day magnetic storm of 2000 at a low mid-latitude station. Geof´ısica Internacional, 44(2): 211– 218.

Astafyeva, E., I. Zakharenkova, and M. Förster, 2015, Ionospheric responseto the 2015 St. Patrick's Day storm: Aglobal multi-instrumental overview,J. Geophys. Res. Space Physics, 120,9023–9037, doi:10.1002/2015JA021629.

Atiq, M. 2018. *Historical Review of Ionosphere in Perspective of Sources of Ionization and Radio Waves Propagation.* https://www.semanticscholar.org/paper/Historical-Review-of-Ionosphere-in-Perspective-of-Atiq/dd324b27346fb18a2b86815822c12dc29f5a3bb0

Azeem, I., Yue, J., Hoffmann, L., Miller, S. D., Straka, W. C., III, and Crowley, G. 2015. Multisensor profiling of a concentric gravity wave event propagating from the troposphere to the ionosphere. Geophysical Research Letters, 42(19), 7874–7880. https://doi.org/10.1002/2015GL065903

Azpilicueta, F., Brunini, C. and Radicella, S. 2012. Semi-annual anomaly and annual asymmetry on TOPEX TEC during a full solar cycle. Geodesy for Planet Earth, pp. 769–774. doi: 10.1007/978-3-642-20338-1 96.

Bagiya, M. S., K. N. Iyer, H. P. Joshi, S. V. Thampi, T. Tsugawa, S. Ravindran, R. Sridharan, and B. M. Pathan 2011, Low-latitude ionospheric-thermospheric response to storm time electrodynamical coupling between high and low latitudes, *J. Geophys. Res.*, 116, A01303, doi:10.1029/2010JA015845.

Bagiya, M. S., R. Hazarika, F. I. Laskar, S. Sunda, S. Gurubaran, D. Chakrabarty, P. K. Bhuyan, R. Sridharan, B. Veenadhari, and D. Pallamraju 2014, Effects of prolonged southward interplanetary magnetic field on low-latitude ionospheric electron density, *J. Geophys. Res. Space Physics*, 119, 5764–5776, doi:10.1002/2014JA020156.

Balachandran, N. K. 1980. Gravity waves from thunderstorms. Monthly Weather Review, 108(6), 804–816. https://doi.org/10.1175/1520-0493(1980)108<0804:gwft>2.0.co;2

Balan, N., Liu, L. and Le, H. 2018. A brief review of equatorial ionization anomaly and ionospheric irregularities. Earth and Planetary Physics, 2(4): 257–275. doi: https://doi.org/10.26464/epp2018025.

Balogh, A., Gosling, J., Jokipii, J., Kallenbach, R. and Kunow, H. 2000. Corotating Interaction Regions: Proceedings of an ISSI Workshop 6-13 June 1998, Bern, Switzerland. Vol. 7, Kluwer Academic Publishers.

Balthazor, R., and Moffett, R. 1997. A study of atmospheric gravity waves and travelling ionospheric disturbances at equatorial latitudes. Annales Geophysicae, 15(8), 1048–1056. https://doi.org/10.1007/s00585-997-1048-4

Balthazor, R.L., Moffett, R.J., 1997 A study of atmospheric gravity waves and travelling ionospheric disturbances at equatorial latitudes. *Annales Geophysicae* 15, 1048–1056 . https://doi.org/10.1007/s00585-997-1048-4

Basu, S., Groves, K., Basu, S. and Sultan, P. 2002. Specification and forecasting of scintillations in communication/navigation links: Current status and future plans. Journal of Atmospheric and Solar-Terrestrial Physics, 64(16): 1745–1754. doi: https://doi.org/10.1016/S1364-6826(02)00124-4.

Basu, S., MacKenzie, E. and Basu, S. 1988. Ionospheric constraints on VHF/UHF communications links during solar maximum and minimum periods. Radio Science, 23(03): 363–378. doi: 10.1029/RS023i003p00363.

Becker, E., and Vadas, S. L. 2020. Explicit global simulation of gravity waves in the thermosphere. Journal of Geophysical Research: Space Physics, 125(10), e2020JA028034. https://doi.org/10.1029/2020JA028034

Beer, T. 1974. Atmospheric waves. New York: John Wiley

Belehaki, A., *et al. 2017*, Ionospheric electron density perturbations during 7–10 March 2012 geomagnetic storm period, Adv. Space Res.

Bilitza, D. (1994). Ionospheric Models: Proceedings of the Topical Meeting of the COSPAR Interdisciplinary Scientific Commission C (Meeting C6) and Symposium B4 of the COSPAR Twenty-ninth Plenary Meeting: 1992, Washington. Elsevier Science Limited.

Blagoveshchenskii, D.V. Effect of magnetic storms (substorms) on HF propagation: A review. Geomagn. Aeron. 53, 409–423 (2013). https://doi.org/10.1134/S0016793213040038

Blanc, M. and Richmond, A.D. 1980 The Ionospheric Disturbance Dynamo. Journal of Geophysical Research: Space Physics, 85, 1669-1686. https://doi.org/10.1029/JA085iA04p01669

Borovsky, J. E., and Denton, M. H. 2006. Differences between CME-driven storms and CIR-driven storms. *Journal of Geophysical Research: Space Physics*, *111*(A7). https://doi.org/10.1029/2005JA011447

Borries, C., A. M. Mahrous, N. M. Ellahouny, and R. Badeke 2016, Multiple ionospheric perturbations during the Saint Patrick's Day storm 2015 in the European-African sector, *J. Geophys. Res. Space Physics*, 121, 11,333–11,345, doi:10.1002/2016JA023178.

Borries, C., Mahrous, A. M., Ellahouny, N. M., and Badeke, R. 2016. Multiple ionospheric perturbations during the Saint Patrick's Day storm 2015 in the European-African sector. Journal of Geophysical Research: Space Physics, 121(11), 11. https://doi.org/10.1002/2016JA023178

Borries, C., N. Jakowski, and V. Wilken 2009, Storm induced large scale TIDs observed in GPS derived TEC, *Ann. Geophys.*, 27(4), 1605–1612, doi:10.5194/angeo-27-1605-2009.

Bowman, G. G. 2001, A comparison of nighttime TID characteristics between equatorial-ionospheric-anomaly crest and midlatitude regions, related to spread F occurrence, J. Geophys. Res., 106(A2), 1761–1769, doi:10.1029/2000JA900123.

Bravo, M., Benavente, R., Foppiano, A., Urra, B. and Ovalle, E. 2022. Traveling ionospheric disturbances observed over South America after lithospheric events: 2010– 2020. Journal of Geophysical Research: Space Physics, 127(4): e2021JA030060. doi: https://doi.org/10.1029/2021JA030060.

Bristow, W. and Greenwald, R. 1997: On the spectrum of thermospheric gravity waves observed by the Super Dual Auroral Radar Network, Journal of Geophysical Research: Space Physics, 102, 11585-11595.

Bristow, W., Greenwald, R., and Samson, J. 1994: Identification of high-latitude acoustic gravity wave sources using the Goose Bay HF radar, Journal of Geophysical Research: Space Physics, 99, 319-331.

Bruinsma, S. L., and Forbes, J. M. 2009. Properties of traveling atmospheric disturbances (TADs) inferred from CHAMP accelerometer observations. Advances in Space Research, 43(3), 369-376.

Buchert, S., Zangerl, F., Sust, M., André, M., Eriksson, A., Wahlund, J.-E., and Opgenoorth, H. 2015. SWARM observations of equatorial electron densities and topside GPS track losses. *Geophysical Research Letters*, *42*(7), 2088–2092. https://doi.org/10.1002/2015GL063121

Burns, A. G., Solomon, S. C., Wang, W., and Killeen, T. L. (2007). The ionospheric and thermospheric response to CMEs: Challenges and successes. *Journal of Atmospheric and Solar-Terrestrial Physics*, *69*(1), 77–85. https://doi.org/10.1016/j.jastp.2006.06.010

Campbell, W. H. 1997. Introduction to geomagnetic fields. Cambridge: Cambridge University Press. Campbell, W. H. 2001. Earth magnetism: a guided tour through magnetic fields. San Diego: Academic Press.

Chamberlain, G, Asymptotic efficiency in estimation with conditional moment restrictions, Journal of Econometrics, 34, 3, 1987, 305-334, 0304-4076, https://doi.org/10.1016/0304-4076(87)90015-7.

Chan, K., and Villard, O., Jr. (1962). Observation of large-scale traveling ionospheric disturbances by spaced-path high-frequency instantaneous-frequency measurements. Journal of Geophysical Research, 67(3), 973–988.

https://doi.org/10.1029/JZ067i003p00973

Chen, G.-m., Xu, J., Wang, W. and Burns, A. G. 2014. A comparison of the effects of CIRand CME-induced geomagnetic activity on thermospheric densities and spacecraft orbits: Statistical studies. Journal of Geophysical Research: Space Physics, 119(9): 7928–7939. doi: https://doi.org/10.1002/2014JA019831.

Cheng, PH., Lin, C., Otsuka, Y. *et al.* Statistical study of medium-scale traveling ionospheric disturbances in low-latitude ionosphere using an automatic algorithm. *Earth Planets Space* 73, 105 (2021). https://doi.org/10.1186/s40623-021-01432-1

Chimonas, G. (1969), Wind-driven instability in the lower E region, *J. Geophys. Res.*, 74(16), 4091–4098, doi:10.1029/JA074i016p04091.

Choi, B., Cho, J. and Lee, S. 2011. Estimation and analysis of GPS receiver differential code biases using KGN in Korean Peninsula. Advances in Space Research, 47(9): 1590–1599. doi: https://doi.org/10.1016/j.asr.2010.12.021.

Cnossen, I., and M. Förster (2016), North-south asymmetries in the polar thermosphere-ionosphere system: Solar cycle and seasonal influences, *J. Geophys. Res. Space Physics*, 121, 612–627, doi:10.1002/2015JA021750.

Crooker, N., Joselyn, J. A. and Feynman, J. 1997. Coronal Mass Ejections. Washington, D.C.:American Geophysical Union.

Daniel Fiso Mahlangu. (2017). *Statistical Study of Traveling Ionospheric Disturbances over South Africa* [MSc, Rhodes University].

Danilov, A., and Laštovička, J. (2002). Effects of geomagnetic storms on the ionosphere and atmosphere. *Int. J. Geomagn. Aeron.*, *7*, 278–286.

Danilov, A.D., 2013. Ionospheric F-region response to geomagnetic disturbances. Advances in Space Research, 52(3), pp.343-366.

Datta-Barua, S., Lee, J., Pullen, S., Luo, M., Ene, A., Qiu, D., et al. (2010). Ionospheric threat parameterization for local area global-positioning-system-based aircraft landing systems. Journal of Aircraft, 47(4), 1141–1151. https://doi.org/10.2514/1.46719

Davies, B., and Harré, R. (1990). Positioning: The Discursive Production of Selves. *Journal for the Theory of Social Behaviour*, *20*(1), 43–63. https://doi.org/10.1111/j.1468-5914.1990.tb00174.x

Davis, M. (1971). On polar substorms as the source of large-scale traveling ionospheric disturbances. Journal of Geophysical Research, 76(19), 4525–4533. https://doi.org/10.1029/JA076i019p04525

Dessler, A. J., and Parker, E. N. (1959). Hydromagnetic theory of geomagnetic storms. *Journal of Geophysical Research (1896-1977)*, *64*(12), 2239–2252. https://doi.org/10.1029/JZ064i012p02239

Dieminger, W., Hartmann, G. K., and Leitinger, R. (1996a). Geomagnetic Activity Indices. In W. Dieminger, G. K. Hartmann, and R. Leitinger (Eds.), *The Upper Atmosphere: Data Analysis and Interpretation* (pp. 887–911). Springer. https://doi.org/10.1007/978-3-642-78717-1_26

Dieminger, W., Hartmann, G., and Leitinger, R. (1996b). *The Upper Atmosphere: Data Analysis and Interpretation.* https://www.semanticscholar.org/paper/The-Upper-Atmosphere%3A-Data-Analysis-and-Dieminger-Hartmann/d1abeeaafca0dF2c96040a0779d8a7536040781b

Ding, F, W. Wan, B. Ning, L. Liu, B. Zhao, Q. Li, and R. Zhang (2013), Statistical study of large-scaletraveling ionospheric disturbances generated by the solar terminator over China, J. Geophys. Res. Space Physics, 118,4583–4593, doi:10.1002/jgra.50423

Ding, F., Wan, W., Ning, B., Zhao, B., Li, Q., Wang, Y., Hu, L., Zhang, R., and Xiong, B.: Observations of poleward-propagating large-scale traveling ionospheric disturbances in southern China, Annales Geophysicae, 31, 377-385, 2013.

Doyle, J. D., Shapiro, M. A., Jiang, Q., and Bartels, D. L. (2005). Large-amplitude mountain wave breaking over Greenland. Journal of the Atmospheric Sciences, 62(9), 3106–3126. https://doi.org/10.1175/JAS3528.1

Dubazane, M. B., and Habarulema, J. B. (2018). An empirical model of vertical plasma drift over the African sector. Space Weather, 16(6), 619–635. https://doi.org/10.1029/2018SW001820

Dugassa, T., Mezgebe, N., Habarulema, J.B., Habyarimana, V. and Oljira, A., 2023. Ionospheric response to the 23–31 August 2018 geomagnetic storm in the Europe-African longitude sector using multi-instrument observations. Advances in Space Research, 71(5), pp.2269-2287.

Eastes, R., Solomon, S., Daniell, R., Anderson, D., Burns, A., England, S., Martinis, C. and McClintock, W. 2019. Global-scale observations of the equatorial ionization anomaly. Geophysical Research Letters, 46(16): 9318–9326. doi: https://doi.org/10.1029/2019GL084199.

Echer, E., Gonzalez, W. and Tsurutani, B. 2011. Statistical studies of geomagnetic storms with peak Dst $\leq$ -50 nT from 1957 to 2008. Journal of Atmospheric and Solar-Terrestrial Physics, 73(11-12): 1454–1459.

Eckermann, S., Hoffmann, L., Höpfner, M., Wu, D., and Alexander, M. (2009). Antarctic NAT PSC belt of June 2003: Observational validation of the mountain wave seeding hypothesis. Geophysical Research Letters, 36(2). https://doi.org/10.1029/2008GL036629

El-Rabbany, A. (2002) Introduction to GPS: The Global Positioning System. Artech House, Norwood.

Evans, J.V. *et al.,* On the formation of daytime troughs in the F-region within the plasmasphere, Geophys. Res. Lett.(1983)

Fagundes, P. R., F. A. Cardoso, B. G. Fejer, K. Venkatesh, B. A. G. Ribeiro, and V. G. Pillat (2016), Positive and negative GPS-TEC ionospheric storm effects during the extreme space weather event of March 2015 over the Brazilian sector, *J. Geophys. Res. Space Physics*, 121, 5613–5625, doi:10.1002/2015JA022214.

Farge, M. (1992). Wavelet transforms and their applications to turbulence. Annual Review of Fluid Mechanics, 24(1), 395–458. https://doi.org/10.1146/annurev.fl.24.010192.002143

Farge, M. 1992. Wavelet transforms and their applications to turbulence. Annual Review of Fluid Mechanics, 24(1): 395–458. doi: https://doi.org/10.1146/annurev.fl.24.010192.002143.

Farrell J.A. and Barth M. (1999) The Global Positioning System and Inertial Navigation. McGraw-Hill.

Fejer, B. G., and L. Scherliess, Mid- and low-latitude prompt-penetration ionospheric zonal plasma drifts, Geophys. Res. Lett., 25, 3071, 1998. https://doi.org/10.1029/98GL02325

Fejer, B. G., Low latitude electrodynamic plasma drifts: A review, J. Atmos. Terr. Phys., 53, 677, 1991.

Fejer, B. G., Low latitude ionospheric electrodynamics, Space Sci. Rev., 158, 145-166, doi:10.10007/s11214-010-9690-7, 2011.

Fejer, B.G., The electrodynamics of the low-latitude ionosphere: Recent results and future challenges, Journal of Atmospheric and Solar-Terrestrial Physics, 59, 13, 1997, 1465-1482, 1364-6826, https://doi.org/10.1016/S1364-6826(96)00149-6.

Ferguson, M. 1997. GPS land navigation: A complete guidebook for backcountry users of the NAVSTAR satellite system. Boiso, ID: Glassgord Publishers.

Figueiredo, C., Wrasse, C., Takahashi, H., Otsuka, Y., Shiokawa, K., and Barros, D. (2017). Large-scale traveling ionospheric disturbances observed by GPS dTEC maps over North and South America on Saint Patrick's Day storm in 2015. Journal of Geophysical Research: Space Physics, 122(4), 4755–4763. https://doi.org/10.1002/2016JA023417

Forster, M. and Jakowski, N.: Geomagnetic storm effects on the topside ionosphere and plasmasphere: a compact tutorial and new results. Surveys in Geophysics, 21, 47-87, 2000.

Fovell, R., Durran, D., and Holton, J. (1992). Numerical simulations of convectively generated stratospheric gravity waves. Journal of the Atmospheric Sciences, 49(16), 1427–1442. https://doi.org/10.1175/1520-0469(1992)049<1427:nsocgs>2.0.co;2

Frissell, N. A., Baker, J. B., Ruohoniemi, J. M., Greenwald, R. A., Gerrard, A. J., Miller, E. S., and West, M. L. (2016). Sources and characteristics of medium-scale traveling ionospheric disturbances observed by high-frequency radars in the North American sector. Journal of Geophysical Research: Space Physics, 121(4), 3722–3739. https://doi.org/10.1002/2015JA022168

Frissell, N. A., E. S. Miller, S. R. Kaeppler, F. Ceglia, D. Pascoe, N. Sinanis, P. Smith, R. Williams, and A. Shovkoplyas (2014), Ionospheric Sounding Using Real-Time Amateur Radio Reporting Networks, *Space Weather*, 12, 651–656, doi:10.1002/2014SW001132.

Frissell, N. A., J. B. H. Baker, J. M. Ruohoniemi, R. A. Greenwald, A. J. Gerrard, E. S. Miller, and M. L. West (2016), Sources and characteristics of medium-scale traveling ionospheric disturbances observed by high-frequency radars in the North American sector, *J. Geophys. Res. Space Physics*, 121, 3722–3739, doi:10.1002/2015JA022168.

Fritts, D. C., and Alexander, M. J. (2003). Gravity wave dynamics and effects in the middle atmosphere. Reviews of geophysics, 41(1). https://doi.org/10.1029/2001RG000106

Fuller-Rowell, T. J., Codrescu, M. V., Moffett, R. J., and Quegan, S. (1994). Response of the thermosphere and ionosphere to geomagnetic storms. *Journal of Geophysical Research: Space Physics*, *99*(A3), 3893–3914. https://doi.org/10.1029/93JA02015

Fuller-Rowell, T.J., G.H. Millward, A.D. Richmond, M.V. Codrescu, Storm-time changes in the upper atmosphere at low latitudes, Journal of Atmospheric and Solar-Terrestrial Physics, 64, 12–14, 2002, 1383-1391, 1364-6826, https://doi.org/10.1016/S1364-6826(02)00101-3.

Förster, M., and I. Cnossen (2013), Upper atmosphere differences between northern and southern high latitudes: The role of magnetic field asymmetry, J. Geophys. Res. Space Physics, 118, 5951–5966, doi:10.1002/jgra.50554.

Gao, Y., Liu, Z. et al., 2002. Precise ionosphere modeling using regional GPS network data. Journal of Global Positioning Systems, 1(3): 18–24.

Garcia, F. J., M. C. Kelley, J. J. Makela, and C.-S. Huang (2000), Airglow observations of mesoscale low-velocity traveling ionospheric disturbances at midlatitudes, *J. Geophys. Res.*, 105(A8), 18407–18415, doi:10.1029/1999JA000305.

Garcia-Fernandez, M., Advisors, J., Juan, J., Zornoza, Manuel, H., and Pajares, M. (n.d.). *Contributions to the 3D ionospheric sounding with GPS data.*

Gonzalez, W. D., Joselyn, J. A., Kamide, Y., Kroehl, H. W., Rostoker, G., Tsurutani, B. T., and Vasyliunas, V. M. (1994). What is a geomagnetic storm? *Journal of Geophysical Research: Space Physics*, *99*(A4), 5771–5792. https://doi.org/10.1029/93JA02867

Gopalswamy, N. 2006. Consequences of coronal mass ejections in the heliosphere. Sun and Geosphere, 1(2): 5–12.

Grocott, A., K. Hosokawa, T. Ishida, M. Lester, S. E. Milan, M. P. Freeman, N. Sato, and A. S. Yukimatu (2013), Characteristics of medium-scale traveling ionospheric disturbances observed near the Antarctic Peninsula by HF radar, *J. Geophys. Res. Space Physics*, 118, 5830–5841, doi:10.1002/jgra.50515.

Guo, X., Zhao, B., Yu, T., Hao, H., Sun, W., Wang, G., et al. (2024). East–west difference in the ionospheric response during the recovery phase of May 2024 super geomagnetic storm over the East Asian. *Journal of Geophysical Research: Space Physics*, 129, e2024JA033170. https://doi.org/10.1029/2024JA033170

Habarulema, J. B., Katamzi, Z. T. and McKinnell, L.-A. 2013. Estimating the propagation characteristics of large-scale traveling ionospheric disturbances using ground-based and satellite data. Journal of Geophysical Research: Space Physics, 118(12): 7768–7782. doi: https://doi.org/10.1002/2013JA018997.

Habarulema, J. B., Katamzi, Z. T., and McKinnell, L. -A. (2013). Estimating the propagation characteristics of large-scale traveling ionospheric disturbances using ground-based and satellite data. Journal of Geophysical Research: Space Physics, 118(12), 7768–7782. https://doi.org/10.1002/2013JA018997

Habarulema, J. B., Thaganyana, G. P., Katamzi-Joseph, Z. T., Yizengaw, E., Moldwin, M. B. and Ngwira, C. M. 2022. A statistical study of poleward traveling ionospheric disturbances over the African and American sectors during geomagnetic storms. Journal of Geophysical Research: Space Physics, 127(4): e2021JA030162. doi: https://doi.org/10.1029/2021JA030162.

Habarulema, J. B., Yizengaw, E., Katamzi-Joseph, Z. T., Moldwin, M. B. and Buchert, S. 2018. Storm time global observations of large-scale TIDs from ground-based and in situ satellite measurements. Journal of Geophysical Research: Space Physics, 123(1): 711–724. doi: https://doi.org/10.1002/2017JA024510.

Habarulema, J. B., Yizengaw, E., Katamzi-Joseph, Z. T., Moldwin, M. B., and Buchert, S. (2018). Storm time global observations of large-scale TIDs from ground-based and in situ satellite measurements. Journal of Geophysical Research: Space Physics, 123(1), 711–724. https://doi.org/10.1002/2017JA024510

Habarulema, J. B., Z. T. Katamzi, andE. Yizengaw (2015), First observationsof poleward large-scale travelingionospheric disturbances overthe African sector duringgeomagnetic storm conditions,J. Geophys. Res. SpacePhysics, 120, 6914–6929,doi:10.1002/2015JA021066.

Habarulema, J. B., Z. T. Katamzi,E. Yizengaw, Y. Yamazaki, and G.Seemala (2016), Simultaneous stormtime equatorward and polewardlarge-scale TIDs on a global scale,Geophys. Res. Lett., 43, 6678–6686,doi:10.1002/2016GL069740

Hajkowicz, L. A. (1999), Monitoring ionospheric response to auroral electrojet activity from sub-auroral to equatorial latitudes in the East Asian-Australian longitudinal sector over a solar cycle (1978–1986), *J. Atmos. Sol. Terr. Phys.*, 61, 857–866.

Hargreaves, J. K. (1979). *The upper atmosphere and solar-terrestrial relations: An introduction to the aerospace environment.* Van Nostrand Reinhold.

Hargreaves, J. K. (John K. (with Internet Archive). (1992). *The solar-terrestrial environment: An introduction to geospace--the science of the terrestrial upper atmosphere, ionosphere, and magnetosphere.* Cambridge [England] ; New York, NY, USA : Cambridge University Press. http://archive.org/details/solarterrestrial0000harg

Heale, C. J., Bossert, K., Vadas, S., Hoffmann, L., D¨ornbrack, A., Stober, G., Snively, J. and Jacobi, C. 2020. Secondary gravity waves generated by breaking mountain waves over Europe. Journal of Geophysical Research: Atmospheres, 125(5): e2019JD031662. doi: https://doi.org/10.1029/2019JD031662.

Heelis, R. A., Hanson, W. B., and Bailey, G. J. (1990). Distributions of He+ at middle and equatorial latitudes during solar maximum. *Journal of Geophysical Research: Space Physics*, *95*(A7), 10313–10320. https://doi.org/10.1029/JA095iA07p10313

Heisler, L. H., and J. D. Whitehead (1960), F-region traveling disturbances and sporadic-E ionization, J. Geophys. Res., 65(9), 2767–2773, doi:10.1029/JZ065i009p02767.

Hernández-Pajares, M., J. M. Juan, and J. Sanz (2006), Medium-scale traveling ionospheric disturbances affecting GPS measurements: Spatial and temporal analysis, *J. Geophys. Res.*, 111, A07S11, doi:10.1029/2005JA011474.

Hines, C. O. (1960). Internal atmospheric gravity waves at ionospheric heights. Canadian Journal of Physics, 38(11), 1441–1481. https://doi.org/10.1139/p60-150

Hines, C. O. 1960. Internal atmospheric gravity waves at ionospheric heights. Canadian Journal of Physics, 38(11): 1441–1481. doi: https://doi.org/10.1029/GM018p0248.

Hobara, Y. and Parrot, M., 2005. Ionospheric perturbations linked to a very powerful seismic event. Journal of Atmospheric and Solar-Terrestrial Physics, 67(7), pp.677-685.

Hocke, K., and Schlegel, K. (1996). A review of atmospheric gravity waves and traveling ionospheric disturbances. Annales Geophysicae, 14, 917–940. https://doi.org/10.1007/s00585-996-0917-6

Hocke, K., and Schlegel, K. (1996). A review of atmospheric gravity waves and travelling ionospheric disturbances: 1982–1995. Annales Geophysicae, 14(9), 917–940. https://doi.org/10.1007/s00585-996-0917-6

Hocke, K., Schlegel, K. A review of atmospheric gravity waves and travelling ionospheric disturbances: 1982-1995. *Annales Geophysicae* **14**, 917–940 (1996). https://doi.org/10.1007/s00585-996-0917-6

Hoffmann, L., Grimsdell, A. W., and Alexander, M. J. (2016). Stratospheric gravity waves at Southern Hemisphere orographic hotspots: 2003–2014 AIRS/Aqua observations. Atmospheric Chemistry and Physics, 16(14), 9381–9397. https://doi.org/10.5194/acp-16-9381-2016

Holton, J. R., Curry, J. A. and Pyle, J. A. 2003. Encyclopedia of Atmospheric Sciences. Vol. 3, New York: Academic Press.

Hooke, W. H.: The ionospheric response to internal gravity waves 1. The F_2-region response, Journal of Geophysical Research: Space Physics, 70, 1970.

Horvath, I. and Lovell, B. C.: Positive and negative ionospheric storms occurring during the 15 May 2005 geomagnetic superstorm, Journal of Geophysical Research: Space Physics, 120, 7822-7837, 2015.

Horvath, I.: Impact of 10 January 1997 geomagnetic storm on the nighttime Weddell Sea Anomaly: A study utilizing data provided by the TOPEX/Poseidon mission and the Defense Meteorological Satellite Program, and simulations generated by the Coupled Thermosphere/Ionosphere Plasmasphere model, Journal of Geophysical Research: Space Physics, 112, A06 329, 2007.

Huang, C.-S., Foster, J. C., Goncharenko, L. P., Erickson, P. J., Rideout, W., and Coster, A. J. (2005). A strong positive phase of ionospheric storms observed by the Millstone Hill incoherent scatter radar and global GPS network. *Journal of Geophysical Research: Space Physics*, *110*(A6). https://doi.org/10.1029/2004JA010865

Huang, C.-S., O. de La Beaujardière, P. A. Roddy, D. E. Hunton, J. O. Ballenthin, M. R. Hairston, and R. F. Pfaff (2013), Large-scale quasiperiodic plasma bubbles: C/NOFS observations and causal mechanism, *J. Geophys. Res. Space Physics*, 118, 3602–3612, doi:10.1002/jgra.50338.

Huba, J., Joyce, G., Sazykin, S., Wolf, R. and Spiro, R. 2005. Simulation study of penetration electric field effects on the low-to mid-latitude ionosphere. Geophysical Research Letters, 32(23). doi: https://doi.org/10.1029/2005GL024162.

Hunsucker, R. D. (1982), Atmospheric gravity waves generated in the high-latitude ionosphere: A review, *Rev. Geophys.*, 20(2), 293–315, doi:10.1029/RG020i002p00293.

Hunsucker, R., and Hargreaves, J. (2002). *The High-Latitude Ionosphere and its Effects on Radio Propagation.* https://doi.org/10.1017/CBO9780511535758

Jing, N., and Hunsucker, R. (1993). A theoretical investigation of sources of large and medium scale atmospheric gravity waves in the auroral oval. Journal of Atmospheric and Terrestrial Physics, 55(13), 1667–1679. https://doi.org/10.1016/0021-9169(93)90171-T

Jonah, O. F., Coster, A., Zhang, S., Goncharenko, L., Erickson, P. J., de Paula, E. R., and Kherani, E. A. (2018). TID observations and source analysis during the 2017 Memorial Day weekend geomagnetic storm over North America. *Journal of Geophysical Research: Space Physics*, 123, 8749–8765. https://doi.org/10.1029/2018JA025367

Jonah, O. F., Coster, A., Zhang, S.,Goncharenko, L., Erickson, P. J., de Paula,E. R., and Kherani, E. A. (2018). TIDobservations and source analysis duringthe 2017 Memorial Day weekendgeomagnetic storm over North

America.Journal of Geophysical Research: SpacePhysics, 123, 8749–8765. https://doi.org/10.1029/2018JA025367

Jonah, O. F., Goncharenko, L., Erickson, P. J., Zhang, S., Coster, A., and Chau, J. L., et al. (2020). Anomalous behavior of the equatorial ionization anomaly during the 2 July 2019 solar eclipse. *Journal of Geophysical Research: Space Physics*, 125, e2020JA027909. https://doi.org/10.1029/2020JA027909

K. Georgieva, B. Kirov / Journal of Atmospheric and Solar-Terrestrial Physics 73 (2011) 207–222, https://doi.org/10.1016/j.jastp.2010.03.003.

Kamide, Y., and Baumjohann, W. (1993). Magnetosphere-Ionosphere Coupling. In *Magnetosphere-Ionosphere Coupling, X, 178 pp. 80 figs.. Springer-Verlag Berlin Heidelberg New York. Also Physics and Chemistry in Space, volume 23.* https://doi.org/10.1007/978-3-642-50062-6

Kamide, Y., and Chian, A. (Eds.). (2007). *Handbook of the Solar-Terrestrial Environment.* Springer. https://doi.org/10.1007/978-3-540-46315-3

Karpachev, A. and Afonin, V. 1998. Ionospheric trough observation probability dependence on the season, local time, longitude and magnetic activity level. Geomagnetizm i Aehronomiya, 38(3): 79–91.

Karpachev, A. T., Klimenko, M. V., Klimenko, V. V., Chirik, N. V., Zhbankov, G. A. and Pustovalova, L. V. 2022. Satellite model of foF$_2$ in winter high-latitude ionosphere describing the trough structure. Advances in Space Research, 69(1): 2–15. doi: https://doi.org/10.1016/j.asr.2021.07.014.

Karpachev, A., Klimenko, M., Klimenko, V. and Pustovalova, L. 2016. Empirical model of the main ionospheric trough for the nighttime winter conditions. Journal of Atmospheric and Solar-Terrestrial Physics, 146: 149–159. doi: https://doi.org/10.1016/j.jastp.2016.05.008.

Katamzi, Z. T., and Habarulema, J. B. (2014). Traveling ionospheric disturbances observed at South African midlatitudes during the 29–31 October 2003 geomagnetically disturbed period. Advances in Space Research, 53(1), 48–62. https://doi.org/10.1016/j.asr.2013.10.019

Katamzi, Z. T., Smith, N., Mitchell, C., Spalla, P., and Materassi, M. (2012). Statistical analysis of travelling ionospheric disturbances using TEC observations from geostationary satellites. Journal of Atmospheric and Solar-Terrestrial Physics, 74, 64–80. https://doi.org/10.1016/j.jastp.2011.10.006

Katamzi, Z., Smith, N., Mitchell, C., Spalla, P. and Materassi, M. 2012. Statistical analysis of travelling ionospheric disturbances using TEC observations from geostationary satellites. Journal of Atmospheric and Solar-Terrestrial Physics, 74: 64–80. doi: https://doi.org/10.1016/j.jastp.2011.10.006.

Katamzi-Joseph, Z. T., Aruliah, A. L., Oksavik, K., Habarulema, J. B., Kauristie, K., and Kosch, M. J. (2019). Multi-instrument observations of large-scale atmospheric gravity waves/traveling ionospheric disturbances associated with enhanced auroral activity over Svalbard. Advances in Space Research, 63(1), 270–281. https://doi.org/10.1016/j.asr.2018.08.042

Kelley, M. C. 2009. The Earth's ionosphere: plasma physics and electrodynamics. Academic Press.

Kelley, M., and Heelis, R. (1989). *The Earth's Ionosphere: Plasma Physics and Electrodynamics.*

Kersley, L., and Hughes, J. A. (1989). On the distinction between large scale and medium-scale atmospheric gravity waves. Annales Geophysicae, 7, 459–462.

Kersley, L., Pryse, S. and Wheadon, N. 1988. Amplitude and phase scintillation at high latitudes over northern Europe. Radio Science, 23(03): 320–330. doi: 10.1029/RS023i003p00320.

Kikuchi, T., Hashimoto, K.K. Transmission of the electric fields to the low latitude ionosphere in the magnetosphere-ionosphere current circuit. *Geosci. Lett.* 3, 4 (2016). https://doi.org/10.1186/s40562-016-0035-6

Kikuchi, T., K. K. Hashimoto, and K. Nozaki (2008), Penetration of magnetospheric electric fields to the equator during a geomagnetic storm, J. Geophys. Res., 113, A06214, doi:10.1029/2007JA012628.

Kivi, R., Dörnbrack, A., Sprenger, M., and Vömel, H. (2020). Far-ranging impact of mountain waves excited over Greenland on stratospheric dehydration and rehydration. Journal of Geophysical Research: Atmospheres, 125(18), e2020JD033055. https://doi.org/10.1029/2020JD033055

Klausner, V., P. R. Fagundes, Y. Sahai, C. M. Wrasse, V. G. Pillat, and F. Becker-Guedes (2009), Observations of GW/TID oscillations in the $F2$ layer at low latitude during high and low solar activity, geomagnetic quiet and disturbed periods, *J. Geophys. Res.*, 114, A02313, doi:10.1029/2008JA013448.

Klobuchar, J. A. 1987. Ionospheric time-delay algorithm for single-frequency GPS users. IEEE Transactions on Aerospace and Electronic Systems, AES-23(3): 325–331. doi: https://doi.org/10.1029/JZ070i005p01254.

Kogure, M., Yue, J., Nakamura, T., Hoffmann, L., Vadas, S. L., Tomikawa, Y., et al. (2020). First direct observational evidence for secondary gravity waves generated by mountain waves over the Andes. Geophysical Research Letters, 47(17), e2020GL088845. https://doi.org/10.1029/2020GL088845

Kotake, N., Otsuka, Y., Ogawa, T., Tsugawa, T., and Saito, A. (2007). Statistical study of medium-scale traveling ionospheric disturbances observed with the gps networks in Southern California. Earth, planets and space, 59(2), 95–102. https://doi.org/10.1186/BF03352681

Kotake, N., Y. Otsuka, T. Tsugawa, T. Ogawa, and A. Saito (2006), Climatological study of GPS total electron content variations caused by medium-scale traveling ionospheric disturbances, *J. Geophys. Res.*, 111, A04306, doi:10.1029/2005JA011418.

Kuai, J., L. Liu, J. Liu, S. Sripathi, B. Zhao, Y. Chen, H. Le, and L. Hu (2016), Effects of disturbed electric fields in the low-latitude and equatorial ionosphere during the 2015St. Patrick's Day storm, *J. Geophys. Res. Space Physics*, 121, 9111–9126, doi:10.1002/2016JA022832.

Kuai, J., Liu, L., Lei, J., Liu, J., Zhao, B., Chen, Y., Le, H., Wang, Y. and Hu, L. 2017. Regional differences of the ionospheric response to the July 2012 geomagnetic storm. Journal of Geophysical Research: Space Physics, 122(4): 4654–4668. doi: https://doi.org/10.1002/2016JA023844.

Kuai, J., Liu, L., Liu, J., Zhao, B., Chen, Y., Le, H. and Wan, W. 2015. The long-duration positive storm effects in the equatorial ionosphere over Jicamarca. Journal of Geophysical Research: Space Physics, 120(2): 1311–1324. doi: https://doi.org/10.1002/2014JA020552.

Kuai, J., Wang, K., Zhong, J., Wan, X., Huang, F., Sun, H., Chen, J., Song, X. and Han, H. 2022. Analysis of the Ionospheric Irregularities and Phase Scintillation at Low and Middle Latitudes Based on Swarm Observations. Remote Sensing, 14(19): 4780. doi: https://doi.org/10.3390/rs14194780.

Kumar, S., Moore, K.B. The Evolution of Global Positioning System (GPS) Technology. *Journal of Science Education and Technology* 11, 59–80 (2002). https://doi.org/10.1023/A:1013999415003

Laundal, K. M., J. W. Gjerloev, N. Østgaard, J. P. Reistad, S. Haaland, K. Snekvik, P. Tenfjord, S. Ohtani, and S. E. Milan (2016), The impact of sunlight on high-latitude equivalent currents, *J. Geophys. Res. Space Physics*, 121, 2715–2726, doi:10.1002/2015JA022236.

Laštovička, J., and Burešová, D. (2023). Relationships Between foF$_2$ and Various Solar Activity Proxies. *Space Weather*, *21*. https://doi.org/10.1029/2022SW003359

Leadon, R. E., Woods, A. J., Wenaas, E. P., and Klein, H. H. (1981). *Analytical Investigation of Emitting Probes in an Ionized Plasma.:* Defense Technical Information Center. https://doi.org/10.21236/ADA104166

Legrand, J.P, and P.A. Simon, Solar cycle and geomagnetic activity: A review for geophysicists. Part I. The contributions to geomagnetic activity of shock waves and of the solar wind, *Ann. Geophys.*, **7 (6)**, 565–578, 1989.

Lei, J., Burns, A. G., Tsugawa, T., Wang, W., Solomon, S. C., Wiltberger, M., et al. (2008). Observations and simulations of quasiperiodic ionospheric oscillations and large-scale traveling ionospheric disturbances during the December 2006 geomagnetic storm. Journal of Geophysical Research, 113(A6). https://doi.org/10.1029/2007JA012807

Leick, A., Rapoport, L. and Tatarnikov, D. 2015. GPS satellite surveying. 4th ed. Hoboken, NJ: Wiley.

Lekshmi, D., Balan, N., Tulasi Ram, S. and Liu, J.Y., 2011. Statistics of geomagnetic storms and ionospheric storms at low and mid latitudes in two solar cycles. Journal of Geophysical Research: Space Physics, 116(A11).

Leutbecher, M., and Volkert, H. (2000). The propagation of mountain waves into the stratosphere: Quantitative evaluation of three-dimensional simulations. Journal of the atmospheric sciences, 57(18), 3090–3108. https://doi.org/10.1175/1520-0469(2000)

Leys, C., Ley, C., Klein, O., Bernard, P., and Licata, L. (2013). Detecting outliers: Do not use standard deviation around the mean, use absolute deviation around the median. Journal of Experimental Social Psychology, 49(4), 764–766. https://doi.org/10.1016/j.jesp.2013.03.013

Liu, J., Liu, L., Nakamura, T., Zhao, B., Ning, B. and Yoshikawa, A. 2014. A case study of ionospheric storm effects during long-lasting southward IMF Bz-driven geomagnetic storm. Journal of Geophysical Research: Space Physics, 119(9): 7716–7731. doi: https://doi.org/10.1002/2014JA020273.

Liu, J., Zhang, D. -H., Coster, A. J., Zhang, S. -R., Ma, G. -Y., Hao, Y. -Q., and Xiao, Z. (2019). A case study of the large-scale traveling ionospheric disturbances in the eastern Asian sector during the 2015 St. Patrick's Day geomagnetic storm. Annales Geophysicae, 37(4), 673–687. https://doi.org/10.5194/angeo-37-673-2019

Liu, L., Wan, W., Chen, Y. and Le, H. 2011. Solar activity effects of the ionosphere: A brief review. Chinese Science Bulletin, 56(12): 1202–1211. doi: 10.1007/s11434-010-4226-9.

Liu, X., Xu, J., Yue, J., Vadas, S. L., and Becker, E. (2019). Orographic primary and secondary gravity waves in the middle atmosphere from 16-year SABER observations. Geophysical Research Letters, 46(8), 4512–4522. https://doi.org/10.1029/2019GL082256

Loewe, C. A., and Prölss, G. W. (1997). Classification and mean behavior of magnetic storms. *Journal of Geophysical Research: Space Physics*, *102*(A7), 14209–14213. https://doi.org/10.1029/96JA04020

Macleod, M. A. 1966. Sporadic E theory. I. Collision-geomagnetic equilibrium. Journal of Atmospheric Sciences, 23(1): 96–109. doi: https://doi.org/10.1175/1520-0469(1966)023<0096:SETICG>2.0.CO;2.

Mallat, S. 1999. A wavelet tour of signal processing. Elsevier.

Mansilla, A.; Avila, M.; Yokoya, N. S., 2012. Current knowledge on biotechnological interesting seaweeds from the Magellan Region, Chile. Rev. Bras. Farmacogn., 22 (4): 760-76

Matamba, T. M., Habarulema, J. B., and McKinnell, L.-A.: Statistical analysis of the ionospheric response during geomagnetic storm conditions over South Africa using ionosonde and GPS data, Space Weather, 13, 536-547, 2015.

Materassi, M. and Mitchell, C. N. 2007. Wavelet analysis of GPS amplitude scintillation: A case study. Radio Science, 42(01): 1–10. doi: https://doi.org/10.1029/2005RS003415.

Materassi, M., and Mitchell, C. N. (2007). Wavelet analysis of GPS amplitude scintillation: A case study. Radio Science, 42(01). https://doi.org/10.1029/2005RS003415

Mayr, H., Harris, I., and Dube, M. (1990). Polar thermospheric joule heating, and redistribution of recombination energy in the upper mesosphere. Journal of Atmospheric and Terrestrial Physics, 52(2), 103–112. https://doi.org/10.1016/0021-9169(90)90072-U

Mayr, H., Harris, I., Varosi, F., and Herrero, F. (1984). Global excitation of wave phenomena in a dissipative multiconstituent medium: 1. Transfer function of the Earth's thermosphere. Journal of Geophysical Research, 89(A12), 10929–10959. https://doi.org/10.1029/JA089iA12p10929

McNamara, L. F. (1991). *The ionosphere: Communications, surveillance, and direction finding.* https://www.semanticscholar.org/paper/The-ionosphere-%3A-communications%2C-surveillance%2C-and-McNamara/d602ac1bdad9513802eae4d986753cfd87d9e5cd

McRae, W. M., and Thomson, N. R. (2004). Solar flare induced ionospheric D-region enhancements from VLF phase and amplitude observations. *Journal of Atmospheric and Solar-Terrestrial Physics*, *66*(1), 77–87. https://doi.org/10.1016/j.jastp.2003.09.009

Medvedev, A. S., Yigit, E., Kuroda, T., and Hartogh, P. (2013). General circulation modeling of ˘ the martian upper atmosphere during global dust storms. J. Geophys. Res. Planets 118, 1–13. doi:10.1002/jgre.20163,2013

Mendillo, M., 2006. Storms in the ionosphere: Patterns and processes for total electron content. Reviews of Geophysics, 44(4).

Meteorology and atmospheric physics, 104(3), 191–197. https://doi.org/10.1007/s00703-009-0024-9

Miller, J. (1991). Reaction time analysis with outlier exclusion: Bias varies with sample size. The Quarterly Journal of Experimental Psychology, 43(4), 907–912. https://doi.org/10.1080/14640749108400962

Mishin, E., Burke, W., Huang, C. and Rich, F. 2003. Electromagnetic wave structures within subauroral polarization streams. Journal of Geophysical Research: Space Physics, 108(A8). doi: https://doi.org/10.1029/2002JA009793.

Misra, P. and Enge, P. (2006) Global Positioning System: Signals, Measurements, and Performance. 2nd Edition, Ganga-Jamuna Press, Lincoln.

Mitra, A.P. (1974). *Ionospheric Effects of Solar Flares.* Springer. http://archive.org/details/ionosphericeffec0046apmi

Moffett, R. and Quegan, S. 1983. The mid-latitude trough in the electron concentration of the ionospheric F-layer: a review of observations and modelling. Journal of Atmospheric and Terrestrial Physics, 45(5): 315–343. doi: https://doi.org/10.1016/S0021-9169(83)80038-5.

Molchanov, O.A., 2004. On the origin of low-and middler-latitude ionospheric turbulence. Physics and Chemistry of the Earth, Parts A/B/C, 29(4-9), pp.559-567.

Moldwin, M. (2008). *An Introduction to Space Weather.* https://doi.org/10.1017/CBO9780511801365

Mosavi, M.R. Azarbad,M.R., Multipath error mitigation based on wavelet transform in L1 GPS receivers for kinematic applications, International Journal of Electronics and Communications, 67, 10, 2013, 875-884, 1434-8411, https://doi.org/10.1016/j.aeue.2013.04.011.

Muella, M., Kherani, E. d., De Paula, E., Cerruti, A., Kintner, P., Kantor, I., Mitchell, C., Batista, I. and Abdu, M. 2010. Scintillation-producing Fresnel-scale irregularities associated with the regions of steepest TEC gradients adjacent to the equatorial ionization anomaly. Journal of Geophysical Research: Space Physics, 115(A3). doi: https://doi.org/10.1029/2009JA014788.

Mukherjee, S., Sarkar, S., Purohit, P. K., and Gwal, A. K. (2010). Seasonal variation of total electron content at crest of equatorial anomaly station during low solar activity conditions. *Advances in Space Research*, *46*(3), 291–295. https://doi.org/10.1016/j.asr.2010.03.024

Mulla, A., Baviskar, J., Baviskar, A. and Bhovad, A. 2015. GPS assisted Standard Positioning Service for navigation and tracking: Review and implementation. in International Conference on Pervasive Computing (ICPC), PUne, India, 8-10 January 2015. IEEE, pp. 1–6. doi: 10.1109/PERVASIVE.2015.7087165

Nastrom, G. D., and Fritts, D. C. (1992). Sources of mesoscale variability of gravity waves. Part I: Topographic excitation. Journal of the Atmospheric Sciences, 49(2), 101–110. https://doi.org/10.1175/1520-0469(1992)049<0101:somvog>2.0.co;2

Nava B, Rodríguez-Zuluaga J, Alazo-Cuartas K, Kashcheyev A, Migoya-Orué Y, Radicella SM, Fleury R. 2016. Middle-and low-latitude ionosphere response to 2015 St. Patrick's Day geomagnetic storm. *J Geophys Res Space Phys* **121(4)**: 3421–3438. https://doi.org/10.1002/2015JA022299.

Negrea, C., Zabotin, N., and Bullett, T. (2018). Seasonal variability of the midlatitude traveling ionospheric disturbances from Wallops Island, VA, Dynasonde data: Evidence of a semiannual variation. *Journal of Geophysical Research: Space Physics*, 123, 5047–5054. https://doi.org/10.1029/2017JA025164

Ngwira, C. M., Habarulema, J. -B., Astafyeva, E., Yizengaw, E., Jonah, O. F., Crowley, G., et al. (2019). Dynamic response of ionospheric plasma density to the geomagnetic storm of 22–23 June 2015. Journal of Geophysical Research: Space Physics, 124(8), 7123–7139. https://doi.org/10.1029/2018JA026172

Ngwira, C. M., McKinnell, L. -A., Cilliers, P. J., and Yizengaw, E. (2012). An investigation of ionospheric disturbances over South Africa during the magnetic storm on 15 May 2005. Advances in Space Research, 49(2), 327–335. https://doi.org/10.1016/j.asr.2011.09.035

Ngwira, C.M. and Pulkkinen, A.A. (2019). An Introduction to Geomagnetically Induced Currents. In Geomagnetically Induced Currents from the Sun to the Power Grid (eds J.L. Gannon, A. Swidinsky and Z. Xu). https://doi.org/10.1002/9781119434412.ch1

Nicolls, M. J., Vadas, S. L., Aponte, N., and Sulzer, M. P. (2014). Horizontal parameters of daytime thermospheric gravity waves and e region nseutral winds over puerto rico. Journal of Geophysical Research: Space Physics, 119(1), 575–600. https://doi.org/10.1002/2013JA018988

Nishida, A. (1968), Geomagnetic *Dp* 2 fluctuations and associated magnetospheric phenomena, *J. Geophys. Res.*, 73(5), 1795–1803, doi:10.1029/JA073i005p01795.

Ogawa, T., Igarashi, K., Aikyo, K., and Maeno, H. (1988). SATELLITE OBSERVATION OF MEDIUM-SCALE TRAVELING IONOSPHERIC DISTURBANCES OVER SYOWA STATION. *Proc. NIPR Symp. Upper Atmos. Phys.*

Oinats, A. V., Kurkin, V. I. and Nishitani, N. 2015. Statistical study of medium-scale traveling ionospheric disturbances using SuperDARN Hokkaido ground backscatter data for 2011. Earth, Planets and Space, 67(1): 1–9. doi: 10.1186/s40623-015-0192-4.

Olafsson, H., and Agústsson, H. (2009). Gravity wave breaking in easterly flow over Greenland and associated low level barrier-and reverse tip-jets.

Oluwadare, T.S., Jakowski, N., Valladares, C.E. *et al.* Climatology of Medium-Scale Traveling Ionospheric Disturbances (MSTIDs) Observed with GPS Networks in the North African Region. *Pure Appl. Geophys.* 179, 2501–2522 (2022). https://doi.org/10.1007/s00024-022-03028-6

Ondoh, T., and Marubashi, K. (2001). *Science of Space Environment.* IOS Press.

Osei-Poku, L., Tang, L., Chen, W., and Mingli, C. (2021). Evaluating Total Electron Content (TEC) Detrending Techniques in Determining Ionospheric Disturbances during Lightning Events in A Low Latitude Region. *Remote Sensing, 13*(23), 4753. https://doi.org/10.3390/rs13234753

Otsuka, Y. (2021). Medium-Scale Traveling Ionospheric Disturbances. In Ionosphere Dynamics and Applications (eds C. Huang, G. Lu, Y. Zhang and L.J. Paxton). https://doi.org/10.1002/9781119815617.ch18

Papitashvili, V. O., Papitashvili, N. E., and King, J. H. (2000). Solar cycle effects in planetary geomagnetic Activity: Analysis of 36-year long OMNI dataset. *GEOPHYSICAL RESEARCH LETTERS*, *27*(17), 2797–2800.

Patel, N. C., Karia, S. P., and Pathak, K. N. (2017). GPS-TEC Variation during Low to High Solar Activity Period (2010-2014) under the Northern Crest of Indian Equatorial Ionization Anomaly Region. *Positioning*, *08*(02), 13–35. https://doi.org/10.4236/pos.2017.82002

Pedatella, N. M., and Forbes, J. M. (2011). Electrodynamic response of the ionosphere to high-speed solar wind streams. *Journal of Geophysical Research: Space Physics*, *116*(A12). https://doi.org/10.1029/2011JA017050

Pignalberi, A., Habarulema, J. B., Pezzopane, M., and Rizzi, R. (2019). On the development of a method for updating an empirical climatological ionospheric model by means of assimilated vTEC measurements from a GNSS receiver network. Space Weather, 17(7), 1131–1164. https://doi.org/10.1029/2019SW002185

Pradipta, R., Valladares, C. E., Carter, B. A., and Doherty, P. H. (2016). Interhemispheric propagation and interactions of auroral traveling ionospheric disturbances near the equator. Journal of Geophysical Research: Space Physics, 121(3), 2462–2474. https://doi.org/10.1002/2015JA022043

Prölss, G. W. (1995). Ionospheric F-Region Storms. In *Handbook of Atmospheric Electrodynamics (1995).* CRC Press.

Prölss, G. W. (2004). *Physics of the Earth's Space Environment.* Springer. https://doi.org/10.1007/978-3-642-97123-5

Rajana, S.S.K., Panda, S.K., Jade, S. et al. Impact of two severe geomagnetic storms on the ionosphere over Indian longitude sector during March-April 2023. Astrophys Space Sci 369, 3 (2024). https://doi.org/10.1007/s10509-024-04268-9

Ramsingh, S. Sripathi, S. Sreekumar, S. Banola, K. Emperumal, P. Tiwari, and B. S. Kumar (2015), Low-latitude ionosphere response to super geomagnetic storm of 17/18 March 2015: Results from a chain of ground-based observations over Indian sector, J. Geophys. Res. Space Physics, 120, 10,864–10,882, doi:10.1002/2015JA021509.

Ratcliffe, J. A. (1960). *Physics of the upper atmosphere.* Academic Press.

Ratcliffe, J. A., and Holzer, T. E. (1973). An Introduction to the Ionosphere and Magnetosphere. *American Journal of Physics*, *41*(5), 761–762. https://doi.org/10.1119/1.1987378

Ratovsky, K. G., A. V. Medvedev, and M. V. Tolstikov (2015), Diurnal, seasonal and solar activity pattern of ionospheric variability from Irkutsk Digisonde data, Adv. Space Res., 55(8), 2041–2047.

Rauber, R. and Ramamurthy, M. 2015. Mesoscale meteorology: Cloud and precipitation bands. Encyclopedia of Atmospheric Sciences: Second Edition, pp. 323–330.

Richardson, I. G. and Cane, H. V. 2010. Near-Earth interplanetary coronal mass ejections during solar cycle 23 (1996–2009): Catalog and summary of properties. Solar Physics, 264(1): 189–237.

Richmond, A. (1978). Gravity wave generation, propagation, and dissipation in the thermosphere. Journal of Geophysical Research, 83(A9), 4131–4145. https://doi.org/10.1029/JA083iA09p04131

Richmond, A. D., C. Peymirat, and R. G. Roble (2003), Long-lasting disturbances in the equatorial ionospheric electric field simulated with a coupled magnetosphere-ionosphere-thermosphere model, *J. Geophys. Res.*, 108(A3), 1118, doi:10.1029/2002JA009758.

Rishbeth, H. (1969). *Introduction to ionospheric physics.* New York : Academic Press. http://archive.org/details/introductiontoio0000rish

Rishbeth, H. (1975). On the Theory of Diffusion in the Ionosphere. *Geophysical Journal of the Royal Astronomical Society*, *41*(3), 311–317. https://doi.org/10.1111/j.1365-246X.1975.tb01615.x

Rishbeth, H. and Garriott, O. K. 1969. Introduction to Ionospheric Physics. Elsevier.

Rishbeth, H., and Barron, D. W. (1960). Equilibrium electron distributions in the ionospheric $F2$-layer. *Journal of Atmospheric and Terrestrial Physics*, *18*(2), 234–252. https://doi.org/10.1016/0021-9169(60)90095-7

Rousseeuw, P. J., and Croux, C. (1993). Alternatives to the median absolute deviation. Journal of the American Statistical Association, 88(424), 1273–1283. https://doi.org/10.1080/01621459.1993.10476408

Rukundo, W. (2023). The ionospheric dynamics of the African sector responding to a severe geomagnetic storm; the storm of 3–5 November 2021. Space Weather, 21, e2022SW003219. https://doi.org/10.1029/2022SW003219

Sabzehee, F., Farzaneh, S., Sharifi, M. A. and Akhoondzadeh, M. 2018. TEC regional modeling and prediction using ANN method and single frequency receiver over Iran. Annals of Geophysics, 61(1): GM103–GM103. doi: 10.4401/ag-7297.

Sahai, Y., Becker-Guedes, F., Fagundes, P.R., de Jesus, R., de Abreu, A.J., Otsuka, Y., Shiokawa, K., Igarashi, K., Yumoto, K., Huang, C.S. and Lan, H.T., 2009. Effects observed in the ionospheric F region in the east Asian sector during the intense geomagnetic disturbances in the early part of November 2004. Journal of Geophysical Research: Space Physics, 114(A3).

Saito, A., Fukao, S. and Miyazaki, S. 1998. High resolution mapping of TEC perturbations with the GSI GPS network over Japan. Geophysical Research Letters, 25(16): 3079–3082. doi: https://doi.org/10.1029/98GL52361.

Savage, B. D., and Sembach, K. R. (1996). INTERSTELLAR ABUNDANCES FROM ABSORPTION-LINE OBSERVATIONS WITH THE *HUBBLE SPACE TELESCOPE*. *Annual Review of Astronomy and Astrophysics*, *34*(1), 279–329. https://doi.org/10.1146/annurev.astro.34.1.279

Schneider, T., 2006. The general circulation of the atmosphere. Annu. Rev. Earth

Planet. Sci., 34(1), pp.655-688.

Schunk, R., and Nagy, A. (2009). *Ionospheres: Physics, Plasma Physics, and Chemistry (Cambridge Atmospheric and Space Science Series).* http://cds.cern.ch/record/2306772

Secan, J., Bussey, R., Fremouw, E. and Basu, S. 1997. High-latitude upgrade to the wideband ionospheric scintillation model. Radio Science, 32(4): 1567–1574. doi: https://doi.org/10.1029/97RS00453.

Seemala, G. and Valladares, C. 2011. Statistics of total electron content depletions observed over the South American continent for the year 2008. Radio Science, 46(5): 1–14. doi: https://doi.org/10.1029/2011RS004722.

Seemala, G. K. (2023). Estimation of ionospheric total electron content (TEC) from GNSS observations. In *Chapter 4 in atmospheric remote sensing principles and applications.* Elsevier.

Seemala, G., and Valladares, C. (2011). Statistics of total electron content depletions observed over the South American continent for the year 2008. Radio Science, 46(5). https://doi.org/10.1029/2011RS004722

Shiokawa, K., Y. Otsuka, C. Ihara, T. Ogawa, and F. J. Rich (2003), Ground and satellite observations of nighttime medium-scale traveling ionospheric disturbance at midlatitude, *J. Geophys. Res.*, 108, 1145, doi:10.1029/2002JA009639, A4.

Silwal, A., Gautam, S., Poudel, P., Karki, M., Adhikari, B., Chapagain, N., Mishra, R., Ghimire, B. and Migoya-Orue, Y. 2021. Global positioning system observations of ionospheric total electron content variations during the 15th January 2010 and 21st June 2020 solar eclipse. Radio Science, 56(5): 1–20. doi: 10.1029/2020RS007215.

Sivakandan, M., Mondal, S., Sarkhel,S., Chakrabarty, D., Sunil Krishna, M.V., Upadhayaya, A. K., et al. (2021).Evidence for the in-situ generationof plasma depletion structures overthe transition region of geomagneticlow-mid latitude. Journal ofGeophysical Research: Space Physics,126, e2020JA028837. https://doi.org/10.1029/2020JA028837

Somsikov, V. 2011. Solar terminator and dynamic phenomena in the atmosphere: A review. Geomagnetism and Aeronomy, 51(6): 707–719. doi: 10.1134/S0016793211060168.

Somsikov, V. and Ganguly, B. 1995. On the formation of atmospheric inhomogeneities in the solar terminator region. Journal of Atmospheric and Terrestrial Physics, 57(12): 1513– 1523. doi: https://doi.org/10.1016/0021-9169(95)00014-S.

Somsikov, V. and Trotskii, B. 1975. Generation of disturbances in the atmosphere during the passage of the solar terminator through it. Geomagnetism and Aeronomy. (USSR)(Engl. Transl.);(United States), 15(5). doi: https://www.osti.gov/biblio/7265156.

Song, Q., F. Ding, W. Wan, B. Ning, L. Liu, B. Zhao, Q. Li, and R. Zhang (2013), Statistical study of large-scale traveling ionospheric disturbances generated by the solar terminator over China, *J. Geophys. Res. Space Physics*, 118, 4583–4593, doi:10.1002/jgra.50423.

Stern, D. P. (1996). A brief history of magnetospheric physics during the space age. *Reviews of Geophysics*, *34*(1), 1–31. https://doi.org/10.1029/95RG03508

Suvorova, A.V., Huang, C.M., Matsumoto, H., Dmitriev, A.V., Kunitsyn, V.E., Andreeva, E.S., Nesterov, I.A. and Tsai, L.C., 2014. Low-latitude ionospheric effects of energetic electrons during a recurrent magnetic storm. Journal of Geophysical Research: Space Physics, 119(11), pp.9283-9302.

Taylor Jr, H., Grebowsky, J. and Chen, A. 1975. Ion composition irregularities and ionosphere-plasmasphere coupling: Observations of a high latitude ion trough. Journal of Atmospheric and Terrestrial Physics, 37(4): 613–623. doi: https://doi.org/10.1016/0021- 9169(75)90056-2.

Temmer, M. 2016. Kinematical properties of coronal mass ejections. Astronomical Notes, 337(10): 1010–1015. doi: https://doi.org/10.1002/asna.201612425.

Thaganyana, G. P., Habarulema, J. B., Ngwira, C. and Azeem, I. 2022. Equatorward medium to large scale traveling ionospheric disturbances of high latitude origin during quiet conditions. Journal of Geophysical Research: Space Physics, 127(3): e2021JA029558. doi:https://doi.org/10.1029/2021JA029558.

Themens, D. R., Watson, C., Zagar, N., Vasylkevych, S., Elvidge, S., McCaffrey, A., Prikryl, ˇ P., Reid, B., Wood, A. and Jayachandran, P. 2022. Global propagation of ionospheric disturbances associated with the 2022 Tonga volcanic eruption. Geophysical Research Letters, 49(7): e2022GL098158. doi: https://doi.org/10.1029/2022GL098158.

Thompson, A. R., Moran, J. M., and Swenson, G. W. (2017). *Interferometry and Synthesis in Radio Astronomy.* Springer International Publishing. https://doi.org/10.1007/978-3-319-44431-4

Titheridge, J. 1995. Winds in the ionosphere—A review. Journal of Atmospheric and Terrestrial Physics, 57(14): 1681–1714. doi: https://doi.org/10.1016/0021-9169(95)00091-F.

Torrence, C. and Compo, G. P. 1998. A practical guide to wavelet analysis. Bulletin of the American Meteorological Society, 79(1): 61–78. doi: https://doi.org/10.1175/1520- 0477(1998)079<0061:APGTWA>2.0.CO;2.

Torrence, C., and Compo, G. P. (1998). A practical guide to wavelet analysis. Bulletin of the American Meteorological Society, 79(1), 61–78. https:// doi.org/10.1175/1520-0477(1998)0792.0.co;2

Tsagouri I., Themens D., Belehaki A.1, Shim J.S., Hoque M., Nykiel G., Borries C., Morozova A., Barata T., Miloch W.J., Ionosphere Variability II: Advances in theory and modelling, Advances in Space Research 2023

Tsugawa, T., A. Saito, and Y. Otsuka (2004), A statistical study of large-scale traveling ionospheric disturbances using the GPS network in Japan, *J. Geophys. Res.*, 109, A06302, doi:10.1029/2003JA010302.

Tsugawa, T., Saito, A., and Otsuka, Y. (2004). A statistical study of large-scale traveling ionospheric disturbances using the GPS network in japan. Journal of Geophysical Research, 109(A6). https://doi.org/10.1029/2003JA010302

Tsurutani, B. T. 2001. The interplanetary causes of magnetic storms, substorms and geomagnetic quiet, edited by ia daglis. Dordrecht: Springer, 38: 103–130.

Tsurutani, B. T., and Gonzalez, W. D. (1997). The Interplanetary Causes of Magnetic Storms: A Review. In *Magnetic Storms* (pp. 77–89). American Geophysical Union (AGU). https://doi.org/10.1029/GM098p0077

Tsurutani, B. T., Gonzalez, W. D., Gonzalez, A. L., Guarnieri, F. L., Gopalswamy, N., Grande, M., Kamide, Y., Kasahara, Y., Lu, G., Mann, I. et al., 2006. Corotating solar wind streams and recurrent geomagnetic activity: A review. Journal of Geophysical Research: Space Physics, 111(A7). doi: https://doi.org/10.1029/2005JA011273.

Turner, N. E., Cramer, W. D., Earles, S. K. and Emery, B. A. 2009. Geoefficiency and energy partitioning in CIR-driven and CME-driven storms. Journal of Atmospheric and Solar-Terrestrial Physics, 71(10-11): 1023–1031. doi: https://doi.org/10.1016/j.jastp.2009.02.005.

Uwamahoro, J. C., Giday, N. M., Habarulema, J. B., Katamzi-Joseph, Z. T. and Seemala, G. K. 2018. Reconstruction of storm-time total electron content using ionospheric tomography and artificial neural networks: A comparative study over the African region. Radio Science, 53(11): 1328–1345. doi: 10.1029/2017RS006499.

Vadas, S. L. and Becker, E. 2018. Numerical modeling of the excitation, propagation, and dissipation of primary and secondary gravity waves during wintertime at McMurdo Station in the Antarctic. Journal of Geophysical Research: Atmospheres, 123(17): 9326–9369. doi: https://doi.org/10.1029/2017JD027974.

Vadas, S. L., and Becker, E. (2018). Numerical modeling of the excitation, propagation, and dissipation of primary and secondary gravity waves during wintertime at McMurdo Station in the Antarctic. Journal of Geophysical Research: Atmospheres, 123(17), 9326–9369. https://doi.org/10.1029/2017JD027974

Vadas, S. L., and Becker, E. (2019). Numerical modeling of the generation of tertiary gravity waves in the mesosphere and thermosphere during strong mountain wave events over the Southern Andes. Journal of Geophysical Research: Space Physics, 124(9), 7687–7718. https://doi.org/10.1029/2019JA026694

Vadas, S. L., and Crowley, G. (2010). Sources of the traveling ionospheric disturbances observed by the ionospheric TIDDBIT sounder near Wallops Island on 30 October 2007. Journal of Geophysical Research, 115(A7). https://doi.org/10.1029/2009JA015053

Vadas, S. L., and Liu, H. -l. (2009). Generation of large-scale gravity waves and neutral winds in the thermosphere from the dissipation of convectively generated gravity waves. Journal of Geophysical Research, 114(A10). https://doi.org/10.1029/2009JA014108

Vadas, S. L., and Liu, H. -L. (2013). Numerical modeling of the large-scale neutral and plasma responses to the body forces created by the dissipation of gravity waves from 6 h of deep convection in brazil. Journal of Geophysical Research: Space Physics, 118(5), 2593–2617. https://doi.org/10.1002/jgra.50249

Vadas, S. L., Liu, H. -L., and Lieberman, R. (2014). Numerical modeling of the global changes to the thermosphere and ionosphere from the dissipation of gravity waves from deep convection. Journal of Geophysical Research: Space Physics, 119(9), 7762–7793. https://doi.org/10.1002/2014JA020280

Vadas, S. L., Xu, S., Yue, J., Bossert, K., Becker, E., and Baumgarten, G. (2019). Characteristics of the quiet-time hot spot gravity waves observed by GOCE over the Southern Andes on 5 July 2010. Journal of Geophysical Research: Space Physics, 124(8), 7034–7061. https://doi.org/10.1029/2019JA026693

Vadas, S. L., Zhao, J., Chu, X., and Becker, E. (2018). The excitation of secondary gravity waves from local body forces: Theory and observation. Journal of Geophysical Research: Atmospheres, 123(17), 9296–9325. https://doi.org/10.1029/2017JD027970

Valladares, C., and Hei, M. A. (2012). Measurement of the characteristics of TIDs using small and regional networks of GPS receivers during the campaign of 17–30 July of 2008. International Journal of Geophysics, 1–14. https://doi.org/10.1155/2012/548784

Valladares, C., Villalobos, J., Hei, M., Sheehan, R., Basu, S., MacKenzie, E., et al. (2009). Simultaneous observation of traveling ionospheric disturbances in the Northern and Southern Hemispheres. Annales Geophysicae, 27(4), 1501–1508. https://doi.org/10.5194/angeo-27-1501-2009

Venkatraman, S., and Heelis, R. (1999). Longitudinal and seasonal variations in nighttime plasma temperatures in the equatorial topside ionosphere during solar maximum. *Journal of Geophysical Research: Space Physics*, *104*(A2), 2603–2611. https://doi.org/10.1029/1998JA900109

Wang, X., Miao, J., Lu, X., Aa, E., Liu, J., Wang, Y., and Liu, S. (2021). Latitudinal impacts of Joule heating on the high-latitude thermospheric density enhancement during geomagnetic storms. *Journal of Geophysical Research: Space Physics*, 126, e2020JA028747. https://doi.org/10.1029/2020JA028747

Wanliss, J. A. and Showalter, K. M. 2006. High-resolution global storm index: Dst versus SYM-H. Journal of Geophysical Research: Space Physics, 111(A2). doi: https://doi.org/10.1029/2005JA011034.

Webb, P. A., and Essex, E. A. (2000). An ionosphere-plasmasphere global electron density model. *Physics and Chemistry of the Earth, Part C: Solar, Terrestrial and Planetary Science*, *25*(4), 301–306. https://doi.org/10.1016/S1464-1917(00)00021-0

Wu, D. L., Preusse, P., Eckermann, S. D., Jiang, J. H., Torre Juarez, M., Coy, L., and Wang, D. Y. (2006). Remote sounding of atmospheric gravity waves with satellite limb and nadir techniques. Advances in Space Research, 37(12), 2269–2277. https://doi.org/10.1016/j.asr.2005.07.031

Xu, G. and Xu, Y. 2016. GPS: Theory, Algorithms and Applications. Springer.

Yizengaw, E., Dyson, P. L., Essex, E. A., and Moldwin, M. B. (2005). Ionosphere dynamics over the Southern Hemisphere during the 31 March 2001 severe magnetic storm using multi-instrument measurement data. *Annales Geophysicae*, *23*(3), 707–721. https://doi.org/10.5194/angeo-23-707-2005

Yizengaw, E., Essex, E. A., and Birsa, R. (2004). The Southern Hemisphere and equatorial region ionization response for a 22 September 1999 severe magnetic storm. *Annales Geophysicae*, *22*(8), 2765–2773. https://doi.org/10.5194/angeo-22-2765-2004

Yu, J., Wang, J., Li, L.Y., Cui, J., Cao, J.B. and He, Z.G., 2020. Electron diffusion by coexisting plasmaspheric hiss and chorus waves: Multisatellite observations and simulations. Geophysical Research Letters, 47(15), p.e2020GL088753.

Yue, J., Hoffmann, L., and Joan Alexander, M. (2013). Simultaneous observations of convective gravity waves from a ground-based airglow imager and the AIRS satellite experiment. Journal of Geophysical Research: Atmospheres, 118(8), 3178–3191. https://doi.org/10.1002/jgrd.50341

Zakharenkova, I., E. Astafyeva, and I. Cherniak (2016), GPS and GLONASS observations of large-scale traveling ionospheric disturbances during the 2015 St. Patrick's Day storm, *J. Geophys. Res. Space Physics*, 121, 12,138–12,156, doi:10.1002/2016JA023332.

Zhao, S. Q., Xiao, C. J., Wang, X. G., Pu,Z. Y., Shi, M. J., and Liu, T. Z. (2019).Observation of a large-amplitude slow magnetosonic wave in the magnetosheath. Journal of Geophysical Research: Space Physics, 124,,https://doi.org/10.1029/2019JA026924

Zolesi, B., Cander, L. R., Zolesi, B., and Cander, L. R. (2014). *Total Electron Content Modelling and Mapping.* 147–160. https://doi.org/10.1007/978-3-642-38430-1_7